UNIVERSITY OF LIVERPOOL

Metasurface-Based Antennas for Wireless Communications and Energy Harvesting

by

Zhang, Wenzhang

B.Eng. MSc.

A thesis submitted in accordance with the requirements for the award of the degree of *Doctor of Philosophy* of the University of Liverpool

May 2021

Declaration

I hereby declare that except where specific reference is made to the work of others, the contents of this dissertation are original and have not been submitted in whole or in part for consideration for any other degree or qualification in this, or any other University. This dissertation is the result of my own work and includes nothing which is the outcome of work done in collaboration, except where specifically indicated in the text.

Zhang, Wenzhang

[Status]

Acknowledgements

First and foremost, I would like to express my deepest gratitude to my main supervisor Dr. Jiafeng Zhou for granting me the precious opportunity to test myself at the highest level. He has encouraged and helped me to grow up from a fresh graduate student to a professional researcher. I learned so much from him both academically and personally. Thank you for the invaluable comments and advice on my research as well as my life and career. It is a great honour for me to be one of his Ph.D. students, and I hope I have repaid the faith he showed in me. I will always treasure your support, encouragement, and guidance. I also would like to thank Prof. Yi Huang for supporting and guiding me in my research. I have learned from him a lot not only about research, but also about professional ethics. He is an experienced antenna expert and his passion and persistence in research have deeply inspired and encouraged me.

I would also like to thank my parents. You have always supported me with no expectation of a reward. Your continuous help and understanding have made my life full of love and I am grateful for everything you have done.

Special thanks are also paid to my brilliant and lovely colleagues and friends; in particular to Dr. Chaoyun Song, Dr. Zhihao Tian, Dr. Zhouxiang Fei, Dr. Muayad Kod, Dr. Muaad Hussein, Dr. Ahmed Alieldin, Dr. Manoj Stanley, Prof. Dajun Lei, Dr. Zhenghua Tang, Mr. Yansong Wang, Mr. Jingyuan Jiang, Dr. Yuan Zhuang, Dr. Anqi Chen, Dr. Sumin David Joseph, Dr. Bahaa Al-Juboori, Dr. Tianyuan Jia, Dr. Chen Xu, Mr. Qiang Hua, Mr. Jinyao Zhang, Mr. Lyuwei Chen, Miss. Jiayou Wang and Mr. Kai Jiang for many fruitful discussions and enjoyable moments. Particular thanks should also be paid to Mark Norman, Mark Burnley, John Gillmore, and Steve Markey from the Electrical Workshop for always being very kind to me and fabricating my circuits very quickly and beautifully. Many thanks should be paid to Rogers company for providing the substrate materials for the antenna and rectifier fabrications.

Table of Contents

List of Figures

List of Publications

[1] **Wenzhang Zhang**, Chaoyun Song, Rui Pei, Yi Huang and Jiafeng Zhou, "Broadband Metasurface Antenna Using Hexagonal Loop-Shaped Unit Cells," *IEEE Access*, vol. 8, pp. 223797-223805, Dec. 2020.

[2] Long Li, Xuanming Zhang, Chaoyun Song, **Wenzhang Zhang**, Tianyuan Jia and Yi Huang, "Compact Dual-Band, Wide-Angle, Polarization- Angle -Independent Rectifying Metasurface for Ambient Energy Harvesting and Wireless Power Transfer," IEEE Transactions on Microwave Theory and Techniques, vol. 69, No.3, pp.1518-1528, Mar. 2021.

[3] Rui Pei, Mark Paul Leach, Eng Gee Lim, Zhao Wang, Chaoyun Song, Jingchen Wang, **Wenzhang Zhang**, Zhenzhen Jiang and Yi Huang, "Wearable EBG-Backed Belt Antenna for Smart On-Body Applications," IEEE Transactions on Industrial Informatics, vol. 16, No.11, pp.7177-7189, Nov. 2020.

[4] **Wenzhang Zhang**, Yuan Zhuang, Chaoyun Song, Yi Huang and Jiafeng Zhou, "A Dual-Band Quasi-Yagi Wearable Antenna with High Directivity," 2018 IEEE MTT-

S International Wireless Symposium (IWS), Chengdu, China, 2018 (IET Active and Passive RF Devices 2018 Best student Paper).

[5] **Wenzhang Zhang**, Yi Huang and Jiafeng Zhou, "Wide-Beam Rectenna Design Using Multi-Port Metasurface-Based Antenna," ACES-China 2021 (Invited Paper).

[6] **Wenzhang Zhang**, Mobayode O. Akinsolu, Mingwei He, Bo Liu, Yi Huang and Jiafeng Zhou, "Design of a Dual-Band Metasurface-Based Antenna with Shorting Pins," IMWS AMP 2021 (has been shortlisted in Best Student Paper Contest).

[7] **Wenzhang Zhang**, Lyuwei Chen, Yi Huang and Jiafeng Zhou, " Pattern Reconfigurable Metasurface-based Antenna," EuCAP2021 (Invited Paper).

[8] **Wenzhang Zhang**, Yi Huang and Jiafeng Zhou, "A Design of Metasurface-Based Antenna using Hexagonal Loop Elements," EuCAP2020 (Best Student Paper Finalist).

[9] **Wenzhang Zhang**, Chaoyun Song, Yi Huang and Jiafeng Zhou, "A Novel Broadband Metasurface-based Antenna," EuCAP2019.

Abstract

With the rapid development of wireless communication systems, there is an increasing demand for high-performance antennas. Broadband or wide beamwidth antennas are commonly required for several purposes, such as data transmission or energy harvesting. However, conventional microstrip antennas have limited bandwidth, and thus, are unable to meet the application demands. The MTS-based antenna has recently been proposed to improve the poor performance of traditional antennas. The antenna performance is improved through the co-excitation of multiple desired MTS modes, such as broadband or wide beamwidth. The aim of this thesis is to explore further possibilities of MTS-based antenna designs in respect of broadband or wide beamwidth performance. This thesis is comprised of three parts.

In the first part, a basic 3×3 MTS-based antenna is taken as an example to analyze the existing modes. When identifying the mode in the MTS-based antenna, the mode identification method used in the waveguide is used as a reference. This basic example can facilitate understanding of how the MTS-based antenna works and provide inspiration in terms of how to excite the desired modes to improve the antenna performance.

The focus of the second part is on improving the bandwidth of the MTS-based antenna, and two designs are presented. The first design is a novel broadband MTS-based antenna achieving a broader bandwidth with hexagonal unit cells, which differs from the conventional square unit cells. Five modes could be excited to obtain a 56% fractional bandwidth. The second design is a dual-band MTS-based antenna, which can achieve the dual-band performance through a composite right-/left-handed structure. To maintain the broadband performance in the higher band, the positions of the shorting pins were analyzed. The second antenna could obtain 25% and 50% fractional bandwidth in the lower and higher frequency bands, respectively.

The third part is mainly a discussion on improving the beamwidth of the MTS-based antenna. A wide beamwidth MTS-based antenna with high gain was designed to receive sufficient power at the receiver part in the energy harvesting system. Three modes with complementary radiation patterns were excited through one middle and two side aperture-coupled feeding ports. By exciting the three modes simultaneously, then linking three modes with a direct current combining rectifier circuit to a single load, a wide beamwidth of 114° could be achieved.

Chapter 1 Introduction

As modern wireless communication has rapidly developed, a higher data rate has emerged for fourth generation/fifth generation (4G/5G) technology compared with the technology of the previous generation. To ensure the reliability and achievability of current communication or energy harvesting, the antennas installed on electronic devices or vehicles need to have the properties of broad bandwidth or wide beamwidth, particularly in the case of long-distance wide-coverage data transmission or energy harvesting systems [1]-[2]. Unfortunately, traditional antennas, such as the microstrip patch antenna, are typically hindered by a narrow bandwidth/beamwidth. To overcome such problem, several solutions have been proposed, including adding parasitic resonators, using a thicker substrate, cutting the U/E-structure on the patch layer, using a capacitive probe feed, and using a L-probe feed [3]-[6]. However, the aforementioned methods either increase the antenna size or the design complexity.

Owing to its unique properties, the MTS antenna has recently emerged as a promising method for improving bandwidth/beamwidth performance. These unique properties allow for the possibility to excite multiple MTS modes and tune the resonant frequencies of excited modes [7]. Thus, exploring how to use the MTS antenna to improve the antenna performance in terms of broad bandwidth/beamwidth is meaningful in wireless communication and energy harvesting systems.

1.1 Metasurface-Based Antennas

Metamaterial (MTM) is an artificially structured material that exhibits unique electromagnetic properties that are not easily found in nature. The permittivity, permeability, and refraction index can be artificially constructed by changing the unit cells in MTM to affect the electromagnetic waves [1]-[3].

Metasurface (MTS) is regarded as two-dimensional or planar MTM. Compared with the wavelength of operation, the size of the unit cells is small [4]. When the unit cells on the MTS respond to electromagnetic resonance and radiation, the MTS is considered to act as an antenna.

The current range of MTS antennas is significantly extensive. The function of the MTS antenna is initially closer to that of the antenna array, and the size of the unit cell in the MTS antenna is around half-wavelength. To achieve diverse purposes, including reflective/transmissive focusing and reflection/refraction, devices such as phase shifters and lumped elements are added after the unit cell [5]. Subsequently, MTS is placed above or below the antenna to enhance the antenna performance in terms of bandwidth and gain. The antenna can still work without the MTS, but will perform poorly [6]. Recently, MTS and antenna have been designed as one, in that the unit cells of MTS serve as the radiator and the MTS itself operates as the radiating aperture receiving the electromagnetic waves from the feed. Combined with MTS electromagnetic functions, such MTS antennas can be designed to act as end-fire antennas or frequency reconfigurable antennas [7].

In this thesis, the MTS and the antenna in the present MTS-based antenna can be taken as a whole. The present MTS-based antenna is discussed from two categories: the field region, and the resonant state of the unit cell. For the field region, the MTS antenna can be classified into near-field MTS and far-field MTS. Since the present MTS-based antenna is always excited by a tightly coupled primary source, the antenna can be classified as near-field MTS [8]. For the resonant state of the unit cell, the present MTS-based antenna is composed of $n \times n$ (n is a finite number) unit cells. For an electrically small unit cell, the dimension is usually less than one-tenth of the operational wavelength. By contrast, the unit cell in an MTS-based antenna is typically larger but still much less than one wavelength. As an example, the typical size of a unit cell for an MTS-based antenna is about 0.15 to 0.2 times the whole wavelength [8]. Additionally, the unit cells in MTS-based antennas are radiators rather than having the characteristics of reflection or refraction.

The unit cells on the MTS layer can be excited in multiple modes, and the resonant frequencies of the multiple modes can be tuned. For instance, the frequency difference between different resonant modes can be small enough to achieve a broad bandwidth. Further, by appropriately choosing the structure and arrangement of unit cells, diverse resonant modes with different radiation patterns or polarizations can be obtained. With multiple modes, MTS-based antennas are suitable for extending the bandwidth, exciting multiple frequency bands, allowing antennas with different radiation patterns to be designed (or pattern reconfigurable antennas), allowing for antennas with different polarizations to be designed (or polarization reconfigurable antennas), and others [9]-[12].

1.2 Performance Improvement of MTS-based Antenna

A variety of MTS-based antenna designs have been developed in order to improve the performance [13]-[26]. In recent years, besides the fundamental mode, attempts have been made to excite other modes in the MTS-based antenna to achieve broadband performance [13]-[17]. Said modes include higher TM mode (TM_{20} mode) [13], TE mode [14], slot mode [15], and others. To excite more modes, two layers are normally considered, the MTS layer and the feed layer. For the MTS layer, multiple resonance modes can be excited by choosing the uniform/non-uniform unit cells [13], [16], modifying the structure of the unit cells [11], and arranging the unit cells in various ways [17]. Regarding the feed layer, besides general aperture-coupled feed methods, L-probe feed [14], differential probe feed [20], and substrate integrated waveguide (SIW)/coplanar waveguide (CPW) feed [11], [17] have also been adopted to excite more modes.

To design an appropriate MTS layer, the properties of the unit cells or the MTS structure layer need to be analyzed in advance, rather than trying different structures and arrangements of unit cells. Among the broadband MTS-based antenna designs, the dispersion diagram of the unit cell is taken as a general method to estimate the resonant frequencies of desired modes in an MTS-based antenna [13], [18]. However, because of the boundary setting, such analysis method is limited to the period unit cells and is not suitable for non-period unit cells. As such, there are limitations in terms of the estimation from the dispersion diagram. Additionally, in several designs, characteristic mode analysis (CMA) is utilized to take the whole MTS layer as a whole and modify the structures of partial unit cells to find the desired modes [11], [19]. In said designs, the characteristic current distributions in CMA provide guidance on how to separate or excite the desired modes.

Compared with broadband antennas, dual-band antennas are more suitable for certain application scenarios. For instance, the integration of different radio modules into one piece of equipment has become a trend, and requires a dual-band antenna to cover two different modes. To extend the lifetime of the devices, the wearable or implantable antenna needs to switch between sleep and wake-up modes [21]. The satellite antenna also needs two different bands for low-speed up-link and high-speed downlink communications, respectively [22]. Based on such applications, several dual-band MTS-based antennas have been investigated since the MTS-based antenna itself has the advantage of broad bandwidth [11], [17], [29]. Such MTS-

based antennas can realize dual-band performance by separating a broad bandwidth into two frequency bands [11], exciting the unit cells with different properties by different feed methods [17], and utilizing a composite right-/left-handed (CRLH) structure [23]. In broadband MTS-based antenna designs, the general fractional bandwidth (FBW) can be over 30%, but in dual-band MTS-based antenna designs, the FBW can normally be over 20% and 10%, respectively. Broadband/dual-band antennas always have a directional radiation pattern (main lobe), and thus, are more suitable for wireless communication systems.

In addition to broad bandwidth, other performance improvements involving gain improvement [24], pattern diversity [25], polarization diversity [26], and function diversity [17] [24] have also been explored. The gain of an MTS-based antenna can be enhanced by modifying the structure of partial unit cells according to current distributions. Compared with an MTS layer with uniform unit cells, the square ring slots on four inner unit cells provide a higher gain [24]. Several techniques have been established to realize MTS-based antennas with various polarizations, such as circular polarization [27]-[32]. Such techniques can also be divided into the MTS layer and the feed layer. For the MTS layer, the methods include using truncated corners on the unit cells [27], using an oblique on the unit cells [28], and cutting an L-shaped slot on the unit cells [29]. Meanwhile, regarding the feed layer, the methods include realizing different phases by feeding networks [30], by a Γ-shaped feeding structure [31], and by a coaxial probe feed [32]. Further, function diversity has also been explored based on MTS-based antennas that have a filtering function [33]-[34], a wireless charging function [35], a beam steering function [36]-[37], and other functions. There are mainly two methods for realizing the filtering function in the MTS-based antenna, which involve taking unit cells as the last-stage resonator of the filter [33] and using unit cells with radiation null properties [34]. For the wireless charging function, the unit cells on the MTS layer are generally connected to the load via the feed network and integrated into the overall harvesting system. Recently, in one study [35], a thorough assessment of the different unit cell structures on the MTS layer was reported, which could be applied to harvest radio-frequency energy. Moreover, several methods for realizing the beam-steering function have been proposed, including using the feed structure to control the magnitude and phase of the coupling from the feed layer to the MTS layer [36], and applying a defected ground structure to the feed layer to extend the scanning range [37].

Additionally, with the advantages of broadband and being able to minimize electronic interference by switching the null location, pattern diversity MTS-based antennas have also gained much attention. Notably, such antennas can also save system energy by dynamically

directing the signal to the targets [25]. To design a pattern diversity MTS-based antenna, the initial step involves learning how to excite the mode with various radiation patterns in an MTS-based antenna. The various radiation patterns of MTS-based antennas include omnidirectional radiation patterns and end-fire radiation patterns, which can be respectively achieved by specific feeding methods. Omnidirectional radiation patterns can be produced by a one-to-four power divider [38], while end-fire radiation patterns can be excited by an open-end substrate integrated waveguide feed [12]. In terms of designing pattern diversity MTS-based antennas, one type involves exciting multiple modes in the MTS-based antenna by different feeding structures, and then switching to different modes [20]. The other type involves designing the pattern reconfigurable MTS-based antenna through mechanical [39] or electronic means [25]. As a result, pattern diversity MTS-based antennas can be used not only in wireless communication systems but also in energy harvesting systems, as evidenced in the aforementioned scenarios.

Regarding broadband and pattern diversity MTS-based antennas, the approaches for improving antenna performance obviously include but are not limited to modifying the structure or the arrangement of unit cells, utilizing multiple/complicated feeding structures, and adopting certain MTM properties, such as the CRLH structure. Among said methods, the ability to modify the structure and the arrangement or adopt the certain MTM properties can be attributed to the specific properties of the MTS-based antenna. MTS-based antennas have multiple radiating gaps on the MTS layer, which allows for different MTS modes to be excited. Co-excitation of multiple desired MTS modes, such as broadband or wide beamwidth, can improve the antenna performance. At the same time, the MTS-based antenna improves performance without increasing the structural complexity or analysis difficulty. Hence, exciting more modes and exploring more possibilities of the MTS-based antenna can facilitate further improvement of the antenna performance.

1.3 Thesis Motivation

Despite the various approaches for increasing antenna bandwidth, research on the relationship between the structure of the unit cell and antenna bandwidth remains inadequate, and the geometry of the unit cell can be considered the most intuitive approach for altering the bandwidth. In addition, there is scarcity of designs for dual-band MTS-based antennas. Several of the existing designs lack the flexibility to control the bandwidth of two bands, and the

frequency ratio in other designs cannot be adjusted. Such shortcomings undoubtedly limit the dual-mode application of dual-band MTS-based antennas in wireless communication systems. Although the assumption is that a dual-band MTS-based antenna using a CRLH structure can overcome such shortcomings, the bandwidth in the higher-band is quite narrow [12]. Further, there is a limited number of studies on the beamwidth improvement of the MTS-based antenna, despite wide-beam high-gain antennas being ideal for energy harvesting applications. By utilizing the multiple modes feature of the MTS-based antenna, modes with various radiation patterns can be effectively excited to extend the beamwidth. However, such concept has yet to be reported in research on the MTS-based antenna.

The aim of this thesis is to overcome the aforementioned concerns and problems. Thus, the motivations of this thesis can be summarized as follows:

- Investigate the basic MTS-based antenna to learn its operating mechanism and how the modes are excited.
- Explore the relationship between the geometry of the unit cell and the bandwidth of the MTS-based antenna. Based on the findings, design a broadband MTS-based antenna.
- Determine why the bandwidth of dual-band MTS-based antennas designed with the CRLH structure is limited. Based on the findings, design a broader dual-band MTS-based antenna.
- Design a wide beamwidth MTS-based antenna for energy harvesting by utilizing the multiple mode property of the MTS-based antenna.

1.4 Thesis Organization

This thesis is divided into six chapters, and the structural framework is shown in Fig. 1.1. The contents of this thesis are organized as follows.

The background of the performance improvement techniques in the MTS-based antenna designs is investigated in Chapter 1, in addition to an introduction of the motivation and objectives of this thesis.

The fundamental theory of the antenna and MTS-based antenna, the common analysis methods of MTS-based antenna, and the literature review of previous MTS-based antenna designs are introduced in Chapter 2.

A basic MTS-based antenna is taken as an example in Chapter 3 to explore how to identify its modes, how to excite the desired modes, and the relationship between the antenna structure and the modes.

Two bandwidth improvement designs based on the MTS-based antenna for wireless communication systems are introduced in Chapter 4. The first design is a broadband MTS-based antenna design using hexagonal unit cells. Based on two advantages of the hexagonal structure, five modes can be excited in this proposed antenna. The second design is a dual-band MTS-based antenna design with appropriate shorting pins. Dual-band performance is achieved by the CRLH structure. The position of the shorting pins is critical for maintaining broadband performance at higher bands while simultaneously exciting modes at lower bands.

An aperture-shared beamwidth improvement MTS-based antenna for energy harvesting systems is introduced in Chapter 5. To receive sufficient power from the receiver in energy harvesting, a wide beamwidth antenna is achieved by exciting three modes with complementary radiation patterns and then connecting to three rectifiers, respectively.

The key contributions of this thesis are summarized in Chapter 6. There are also some future work suggestions for the MTS-based antenna.

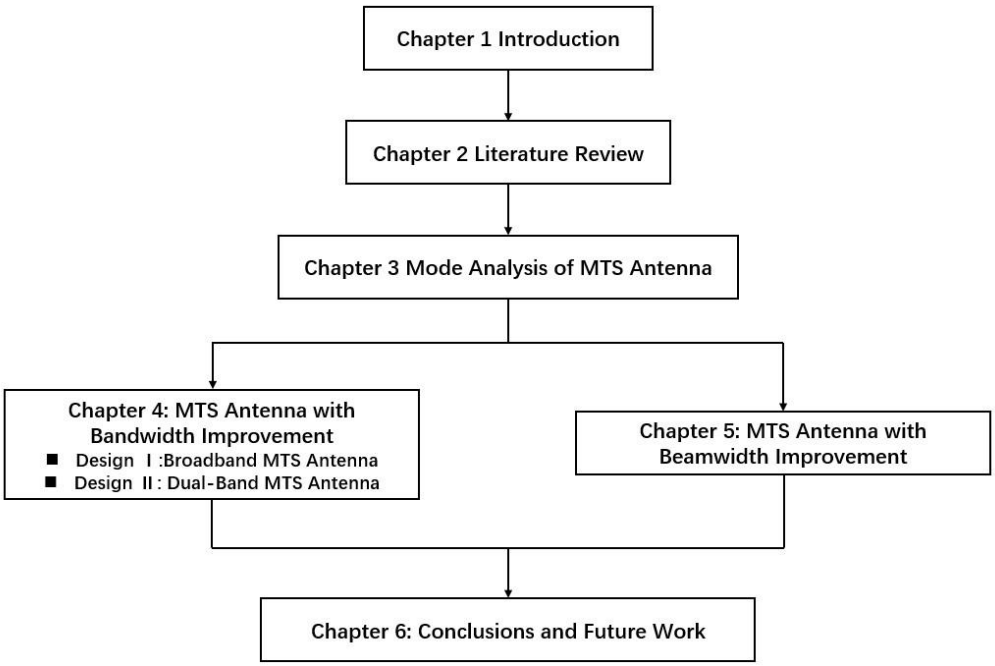

Figure 1.1. Structural framework of this thesis.

For convenience of writing, ‘MTS antenna’ is hereinafter used to refer to ‘MTS-based antenna’.

1.5 References

[1] C. Caloz and T. Itoh, Electromagnetic Metamaterials Transmission Line Theory and Microwave Applications. New York: Wiley, 2006.

[2] T. J. Cui, R. Liu, and D. R. Smith, Metamaterials: Theory, Design, and Applications. New York: Springer Science, 2010.

[3] D. H. Werner and D. H. Kwon, Transformation Electromagnetics and Metamaterials. Springer, 2015.

[4] S. S. Bukhari, J. Vardaxoglou and W. Whittow, "A Metasurfaces Review: Definitions and Applications," *Applied Sciences*, vol. 9, no. 13, pp. 2727-2741, 2019.

[5] J. Wang, Y. Li, Z. Jiang, T. Shi, M. Tang, Z. Zhou, Z. N. Chen, and C. Qiu, "Metantenna: When Metasurface Meets Antenna Again," *IEEE Transaction on Antennas and Propagation*, vol. 68, no. 3, pp. 1332-1347, Mar. 2020.

[6] K. Chen, Z. Yang, Y. Fenga, B. Zhu, J. Zhao, and T. Jiang, "Improving microwave antenna gain and bandwidth with phase compensation metasurface," *AIP Advances*, vol. 5, no. 6, pp. 067152(1-8), Jun. 2015.

[7] M. E. Badawe, T. A., and O. M. Ramahi, "A true metasurface antenna," 26 Jun.-1 Jul. 2016; Fajardo, PR, USA; IEEE International Symposium on Antennas and Propagation (APSURSI), pp. 1903-1904.

[8] F. Lin, "Study of Microwave Metasurface Antenna Using Characteristic Mode Analysis", Ph.D. thesis, Department of Electronics, National University of Singapore, 2018 [Online]. Available: https://scholarbank.nus.edu.sg/handle/10635/150286.

[9] F. Lin and Z. N. Chen, "Recent Progress in Metasurface Antennas Using Characteristic Mode Analysis," 31 Mar.-5 Apr. 2019; Krakow, Poland; 13th European Conference on Antennas and Propagation (EuCAP 2019), pp. 1-4.

[10] F. H. Lin and Z. N. Chen, “Probe-fed broadband low-profile metasurface antennas using characteristic mode analysis,” 16-19 Oct. 2017; Xi'an, China; Proc. IEEE Asia–Pacific Conf. Antennas Propagation (APCAP), Xi’an, pp. 664-666.

[11] T. Li and Z. N. Chen, “A dual-band metasurface antenna using characteristic mode analysis,” *IEEE Transactions on Antennas and Propagation*, vol. 66, no. 10, pp. 5620-5624, 2018.

[12] T. Li and Z. N. Chen, “Wideband substrate integrated waveguide (SIW)-fed end-fire metasurface antenna array,” *IEEE Transactions on Antennas and Propagation*, vol. 66, no. 12, pp. 7032-7040, 2018.

[13] W. Liu, Z. N. Chen, and X. Chen, “Metamaterial-Based Low-Profile Broadband Mushroom Antenna,” *IEEE Transactions on Antennas and Propagation*, vol. 62, no. 3, pp. 1165-1172, 2014.

[14] W. Liu, Z. N. Chen, and X. Chen, “Broadband Low-Profile L-Probe Fed Metasurface Antenna With TM Leaky Wave and TE Surface Wave Resonances,” *IEEE Transactions on Antennas and Propagation*, vol. 68, no. 3, pp. 1348-1355, 2020.

[15] F. Lin and Z. N. Chen, “Low-Profile Wideband Metasurface Antennas Using Characteristic Mode Analysis,” *IEEE Transactions on Antennas and Propagation*, vol. 65, no. 4, pp. 1706-1713, 2017.

[16] W. Liu, Z. N. Chen, and X. Chen, “Miniature Wideband Non-Uniform Metasurface Antenna Using Equivalent Circuit Model,” *IEEE Transactions on Antennas and Propagation*, vol. 68, no. 7, pp. 5652-5657, 2020.

[17] T. Li and Z. N. Chen, “Metasurface-Based Shared-Aperture 5G-Band Antenna Using Characteristic Mode Analysis,” *IEEE Transactions on Antennas and Propagation*, vol. 66, no. 12, pp. 6742-6750, 2018.

[18] W. Wan, M. Xue, L. Cao, T. Ye, and Q. Wang,” Low-Profile Broadband Patch-Driven Metasurface Antenna,” *IEEE Antennas and Wireless Propagation Letters*, vol. 19, no. 7, pp. 1251-1255, 2020.

[19] D. Chen, W. Yang, W. Che, and Q. Xue, “Broadband Stable-Gain Multiresonance Antenna Using Nonperiodic Square-Ring Metasurface,” *IEEE Antennas and Wireless Propagation Letters*, vol. 18, no. 8, pp. 1537-1541, 2019.

[20] X. Yang, J. Hu, Y. Ji, L. Ge, and X. Zeng, “Design of a Metasurface Antenna With Pattern Diversity,” *IEEE Antennas and Wireless Propagation Letters*, vol. 19, no. 12, pp. 2467-2471, 2020.

[21] C. Liu, Y. Guo, and S. Xiao, “Compact Dual-Band Antenna for Implantable Devices,” *IEEE Antennas and Wireless Propagation Letters*, vol. 11, pp. 1508-1511, 2012.

[22] D. E. Serup, G. F. Pedersen, and S. Zhang, “Dual-Band Shared Aperture Reflectarray and Patch Antenna Array for S- and Ka-Band,” *IEEE Transactions on Antennas and Propagation* (Early Access).

[23] Z. Wu, L. Li, X. Chen, and K. Li, “Dual-Band Antenna Integrating With Rectangular Mushroom-Like Superstrate for WLAN Applications,” *IEEE Antennas and Wireless Propagation Letters*, vol. 15, pp. 1269-1272, 2016.

[24] J. Park, M. Jeong, N. Hussain, S. Rhee, S. Park, and N. Kim, “A low-profile high-gain filtering antenna for fifth generation systems based on nonuniform metasurface,” *Microwave and Optical Technology Letters*, vol. 61, no. 11, pp. 2513-2519, 2019.

[25] J. Liu, Z. Weng, Z. Zhang, Y. Qiu, Y. Zhang, and Y. Jiao, “A Wideband Pattern Diversity Antenna With a Low Profile Based on Metasurface,” *IEEE Antennas and Wireless Propagation Letters*, vol. 20, no. 3, pp. 303-307, 2021.

[26] W. Li, Y. Wang, Y. Hei, B. Li, and X. Shi, “A Compact Low-Profile Reconfigurable Metasurface Antenna With Polarization and Pattern Diversities,” *IEEE Antennas and Wireless Propagation Letters*, vol. 20, no. 7, pp. 1170-1174, 2021.

[27] S. X. Ta and I. Park, “Low-Profile Broadband Circularly Polarized Patch Antenna Using Metasurface,” *IEEE Transactions on Antennas and Propagation*, vol. 63, no. 12, pp. 5929–5934, Dec. 2015.

[28] Z. Wu, L. Li, Y. Li, and X. Chen, “Metasurface Superstrate Antenna With Wideband Circular Polarization for Satellite Communication Application,” *IEEE Antennas and Wireless Propagation Letters*, vol. 15, pp. 374-377, 2016.

[29] Q. Chen and H. Zhang, "Dual-Patch Polarization Conversion Metasurface-Based Wideband Circular Polarization Slot Antenna," *IEEE Access*, vol. 6, pp. 74772-74777, Nov. 2018.

[30] S. Liu, D. Yang, and J. Pan, "A Low-Profile Circularly Polarized Metasurface Antenna With Wide Axial-Ratio Beamwidth," *IEEE Antennas and Wireless Propagation Letters*, vol. 18, no. 7, pp. 1438-1442, 2019.

[31] H. W. Lai, K. M. Mak, and K. F. Chan, "Novel Aperture-Coupled Microstrip-Line Feed for Circularly Polarized Patch Antenna," *Progress in Electromagnetics Research*, vol. 144, pp. 1-9, 2014.

[32] Y. Dong, H. Toyao, and T. Itoh, "Compact Circularly-Polarized Patch Antenna Loaded with Metamaterial Structures", *IEEE Transactions on Antennas and Propagation*, vol. 59, no. 11, pp. 4329-4334, 2011.

[33] W. Yang, S. Chen, Q. Xue, W. Che, G. Shen, and W. Feng, "Novel Filtering Method Based on Metasurface Antenna and Its Application for Wideband High-Gain Filtering Antenna With Low Profile," *IEEE Transactions on Antennas and Propagation*, vol. 67, no. 3, pp. 1535-1544, Mar. 2019.

[34] Y. M. Pan, P. F. Hu, X. Y. Zhang, and S. Y. Zheng, "A Low-Profile High-Gain and Wideband Filtering Antenna With Metasurface," *IEEE Transactions on Antennas and Propagation*, vol. 64, no. 5, pp. 2010–2016, May. 2016.

[35] A. A. G. Amer and S. Zahirah, "A Comprehensive Review of Metasurface Structures Suitable for RF Energy Harvesting," *IEEE Access*, vol. 8, pp. 76433-76452, Apr. 2020.

[36] W. Yang, L. Gu, W. Che, Q. Meng, Q. Xue, and C. Wan, "A Novel Steerable Dual-Beam Metasurface Antenna Based on Controllable Feeding Mechanism," *IEEE Transactions on Antennas and Propagation*, vol. 67, no. 2, pp. 784–793, Feb. 2019.

[37] L. Gu, Y. Zhao, Q. Cai, Z. Zhang, B. Xu, and Z. Nie, "Scanning Enhanced Low-Profile Broadband Phased Array With Radiator-Sharing Approach and Defected Ground Structures," *IEEE Transactions on Antennas and Propagation*, vol. 65, no. 11, pp. 5846 – 5854, Nov. 2017.

[38] X. Yang, Y. Liu, and S. Gong, “Design of a Wideband Omnidirectional Antenna With Characteristic Mode Analysis,” *IEEE Antennas and Wireless Propagation Letters*, vol. 17, no. 6, pp. 993-997, 2018.

[39] H. Zhu, S. W. Cheung, and T. I. Yuk, “Mechanically pattern reconfigurable antenna using metasurface,” *IET Microwaves, Antennas & Propagation*, vol. 9, no. 12, pp. 1331-1336, 2015.

Chapter 2 A Review of Metasurface-Based Antennas

2.1 Antenna Fundamentals

2.1.1 Antenna Performance Parameters

When designing the antenna, several important antenna performance parameters are S-parameter, bandwidth, impedance, gain, radiation pattern, beamwidth, and polarization [1]-[7].

- **S-parameter (reflection coefficient)**

S_{11} refers to how much power is reflected from the antenna and is known as reflection coefficient or return loss. If S_{11}= 0 dB, all power is reflected from the antenna, and nothing is radiated. If S_{11}= -10 dB, 10% of the incident power is reflected towards the source from the antenna [8, 9].

- **Bandwidth**

Bandwidth describes the range of frequencies over which the antenna can properly radiate or receive energy [8, 9].

- **Impedance**

Antenna impedance relates to the voltage and the current at the input to the antenna. The real part of the antenna impedance represents power that is either radiated away or absorbed within the antenna. The imaginary part of the antenna impedance represents power that is stored in the near field of the antenna. Normally, an antenna with a real input impedance (zero imaginary part) is said to be resonant [8, 9].

- **Gain**

Antenna gain describes the amount of power transmitted in the direction of peak radiation to that of an isotropic source [8, 9].

- **Radiation pattern**

Radiation pattern defines the power variation radiated by an antenna as a function of the direction away from the antenna, as shown in Fig. 2. 1. This power variation as a function of the arrival angle is observed in the antenna far field [8, 9].

- **Beamwidth**

Beamwidth is the aperture angle from where most of the power is radiated, which is the peak power. One of the main considerations of beamwidth is half power beamwidth (HPBW), as shown in Fig. 2. 1. HPBW is the angular separation, in which the magnitude of the radiation pattern decreases by 50% (or -3 dB) from the peak of the main beam [8, 9].

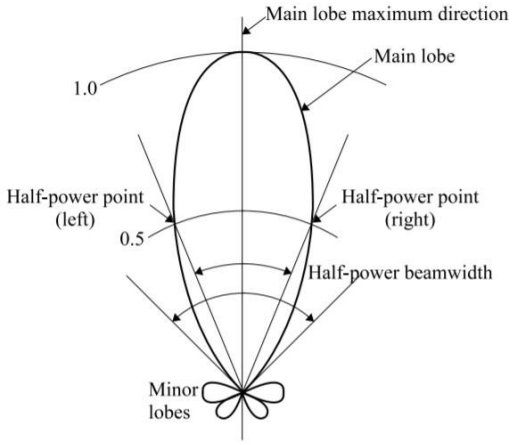

Figure 2.1. Antenna radiation pattern (including HPBW) [10].

- **Polarization**

Polarization refers to the direction of the electric fields produced by an antenna as energy radiates away therefrom. The directional fields determine the direction in which the energy radiates away from.

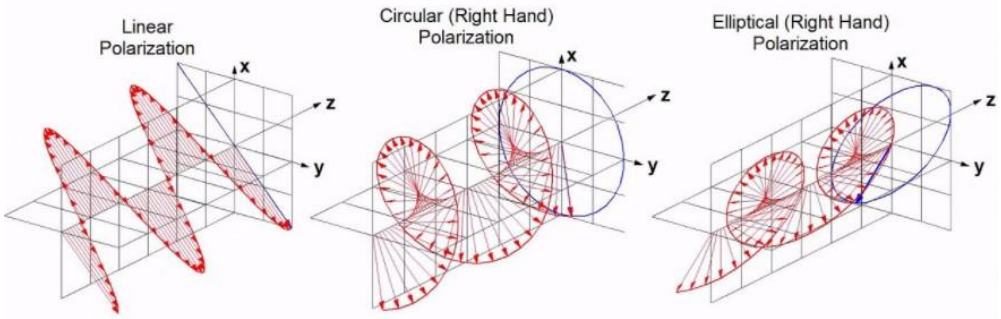

Figure 2.2. Antenna polarization (including linear/circular/elliptical polarization) [11].

Linear polarization:

The electric field of wave is confined to a single plane along the direction of propagation, as shown in Fig. 2. 2 [12].

Circular polarization:

The electric field of wave consists of two linear components that are perpendicular to each other and equal in amplitude, but have a phase difference of $\pi/2$. The resulting electric field that rotates in a circle around the direction of propagation is referred to as left-/right-hand circular polarization. Fig. 2. 2 shows the right-hand circular polarization [12].

Elliptical polarization:

The electric field of wave describes an ellipse, which results from the combination of two linear components with different amplitudes and/or a phase difference that is not $\pi/2$, as shown in Fig. 2. 2(c) [12].

2.1.2 Antenna Type (Related)

2.1.2.1 Microstrip Patch Antenna

The geometry of the microstrip patch antenna is shown in Fig. 2. 3, and consists of a patch layer, a substrate layer, and a ground plane layer. The patch layer, microstrip transmission line and ground plane layer are made of high conductivity metal (normally copper). The substrate layer is between the patch layer and the ground plane layer, with dielectric constant ε_r and thickness d. Typically, the thickness d of substrate material is much lower than the full wavelength [8, 9].

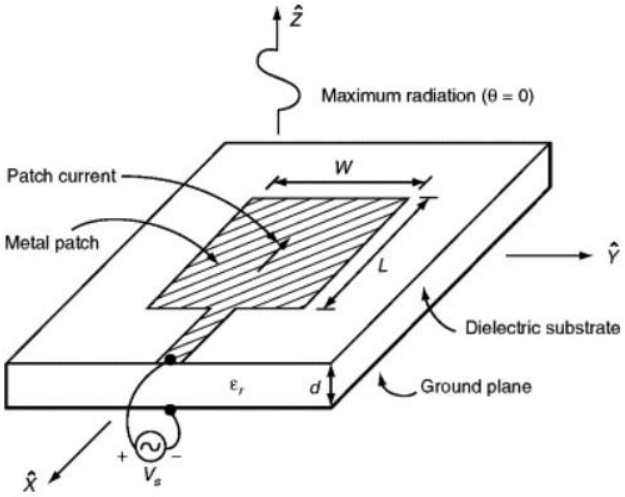

(a)

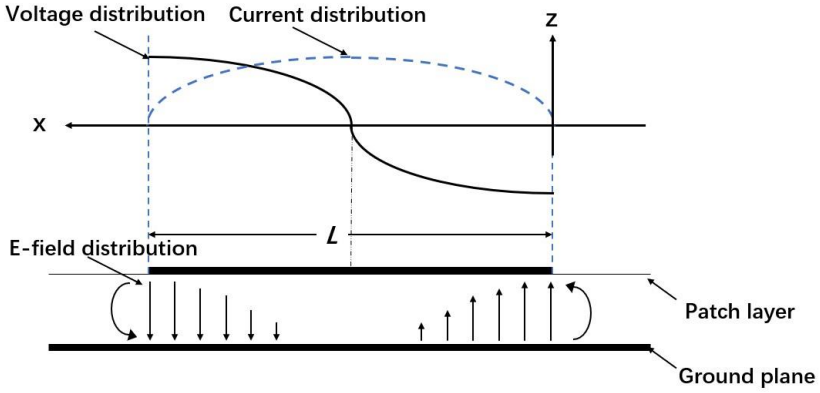

(b)

Figure 2.3. Microstrip patch antenna with (a) 3D view and (b) side view [13].

The patch is of length *L*, width *W*, and sits on top of a substrate material. The frequency of the patch antenna in Fig. 2. 3(a) is determined by the patch length *L*. The center frequency is approximately given by:

$$f_c = \frac{c}{2L\sqrt{\varepsilon_r}} \tag{2. 1}$$

In equation 2. 1, *c* is the light speed, and the microstrip patch antenna should have a length equal to one half of a wavelength within the dielectric (substrate medium) [8, 9].

The width *W* of the microstrip patch antenna is related to the input impedance.

Fig. 2. 3(b) shows the E-field distributions of the fundamental mode on the xoz cutting plane of Fig. 2. 3(a). The E-field distribution is zero at the patch center and has a maximum magnitude

on both edges. The E-field distributions do not stop abruptly near the patch edges, and the E-field extends beyond the outer periphery. Such field extensions are fringing fields that induce the antenna radiation. The fundamental mode of the patch antenna is TM_{10} mode, which is demonstrated in Fig. 2. 3(b). In the figure, the H-field is transverse to the ground plane, but the E-field is not. Index "01" is the number of times the signs of the E-field are flipped along the x-axis and the y-axis, respectively [8, 9].

2.1.2.2 Waveguide (Waveguide Mode)

In this section, the waveguide mode is introduced. The waveguide mode is introduced because the mode identification method in the waveguide (namely identifying the mode from E-/H-field distributions) was taken as a reference while identifying the mode in the MTS antenna.

A variety of modes exist in the waveguide during signal propagation, including TE, TM and TEM modes. The TE mode refers to when the waveguide mode is dependent upon the transverse electric wave, in which the electric vector is always perpendicular to the propagation direction. The TM mode refers to when the waveguide mode is dependent upon the transverse magnetic mode, in which the magnetic vector is always perpendicular to the propagation direction. The transverse electromagnetic wave cannot be propagated within a waveguide but is included for completeness. Both the electric vector and the magnetic vector are perpendicular to the propagation direction [14]. The TE, TM and TEM modes in the waveguide are represented in Fig. 2. 4.

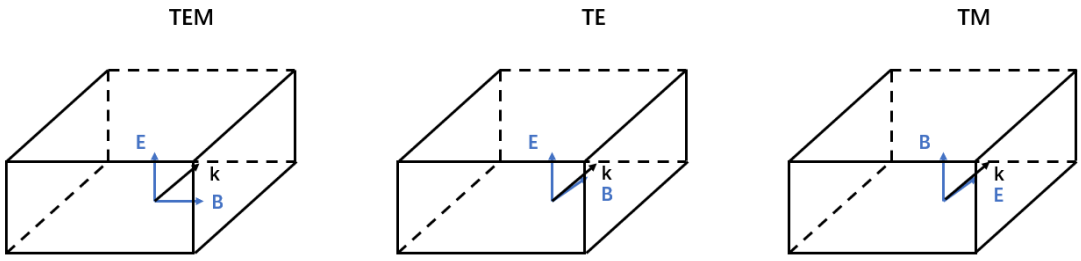

Figure 2.4. (a) TEM mode, (b) TE mode and (c) TM mode in waveguide [14].

Regarding the different waveguide mode, two integers will normally exist after the TE and TM modes, namely, the $TE_{m,n}$ and $TM_{m,n}$ modes. In a square or rectangular waveguide, for the TE_{mn} or TM_{mn} mode, *m* is the number of half-wave patterns across the width of the waveguide and *n* is the number of half-wave patterns across the height of the waveguide, as shown in Fig. 2. 5. For example, in Fig. 2. 5(b), the E-field is represented by solid lines and the H-field is

represented by dashed lines. From the xoy plane, the H-field goes zero at the center along both the *a* dimension and the *b* dimension, which is one half wavelength. Thus, according to the H-field distributions in Fig. 2. 5(b), the mode is TM_{11}.

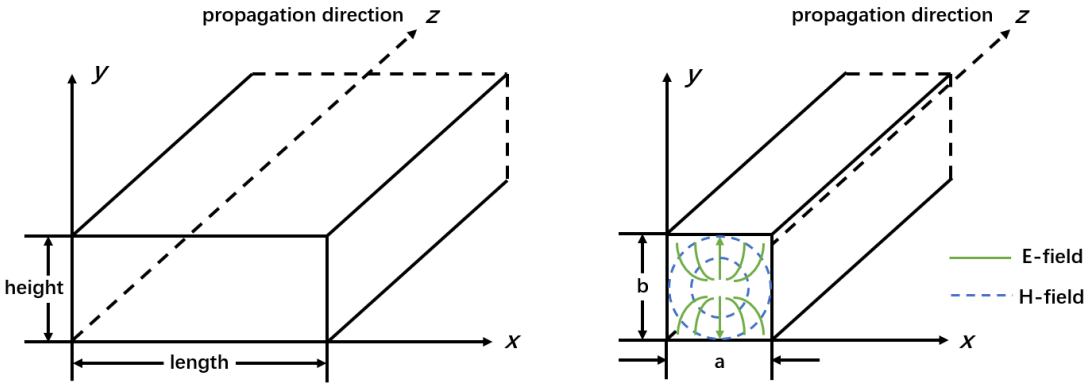

Figure 2.5. (a) Rectangular waveguide and (b) square waveguide (TM_{11} mode) [14].

Waveguides have an extensive range of applications. For instance, a waveguide antenna is a form of antenna dish used in radar applications, for which waveguides are used to transmit the radio beam between the large steerable dish and the equipment for transmitting and receiving [9].

2.1.3 Antenna in Energy Harvesting

MTS antennas have the advantage of performance improvement in terms of bandwidth and beamwidth, which is beneficial not only for wireless communication but also for energy harvesting systems. As such, basic knowledge of energy harvesting systems is presented as follows.

2.1.3.1 Fundamental of Rectenna

A typical energy harvesting system is shown in Fig. 2. 6, which can be roughly divided into two parts: the RF power source part and the receiver part. The receiver part, normally referred to as the rectenna, contains the antenna, the matching circuit, the rectifier, the energy management, and the energy storage component [15]. The antenna captures the RF energy radiated from the RF source or environment. The matching circuit matches the impedance of antenna to the rectifier, which transforms the RF energy to DC energy. The energy management

module subsequently coverts the energy into usable DC output to the load, such as rechargeable batteries or supercapacitors [15].

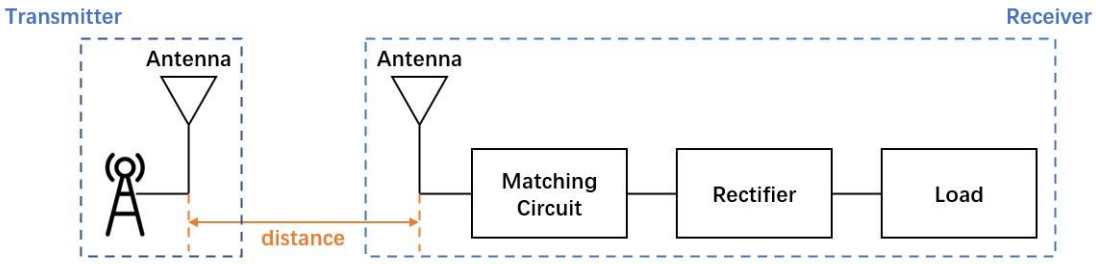

Figure 2.6. Energy harvesting system model [15].

The RF input power of the antenna is P_{RF}, and the DC output power of the rectifier is P_{DC}. The RF-to-DC conversion efficiency of the rectifier can be expressed as follows [15]:

$$\eta_{Rectifier} = \frac{P_{DC}}{P_{RF}} \tag{2. 2}$$

The overall efficiency of the energy harvesting system can be expressed as the ratio of the DC output power at the end of the system to the input RF power at the beginning of the antenna, which can be expressed as [15]:

$$\eta_{RF-DC} = \frac{P_{DC}}{P_{av}} = (1 - |\Gamma|^2) \cdot \eta_{Rectifier} \tag{2. 3}$$

2.1.3.2 Design Methods in Energy Harvesting

In energy harvesting systems, the aim is to capture a sufficient number of electromagnetic waves and convert their RF energies into DC energies by means of a rectifier circuit. Typically, two considerations need to be taken in an energy harvesting system. One consideration is that the antenna needs to capture as many electromagnetic waves as possible in a specific frequency range. The other consideration is that the RF-to-DC conversion efficiency from the antenna to the rectifier circuit needs to be as high as possible. Through such considerations, the energy loss in the whole receiver part should be as small as possible [15]. The related design in this thesis focuses on the first consideration.

To facilitate the capture of more power in an antenna, several antenna performance parameters could be improved, such as bandwidth, beamwidth, gain, and polarization. In most RF energy harvesting systems, the direction of the incident power is supposed to be unknown. Based on

such environment, a receiver antenna with a wide beamwidth is preferred for increasing the collected power from low RF densities. In this thesis, a multibeam or wide beamwidth antenna design with high gain was taken as the solution in the energy harvesting system.

2.2 Basics of MTS Antenna

2.2.1 Definition of MTS Antenna

MTS antennas contain an MTS layer and a feed layer. The MTS layer contains finite-sized unit cells as the main radiator, while the feed structure of the MTS antenna is placed at the near field of the main radiator, which is tightly attached to the MTS layer. Notably, the behavior of the MTS cannot be accurately predicted by period unit cell boundaries since the edges from the main radiator to the substrate boundaries have a large effect on the antenna performance [16].

Finite-sized MTS antennas, such as planar antennas, can excite multiple modes. As such, the MTS has several advantages, including: (a) the possibility of exciting multiple resonant modes to achieve broad bandwidth; (b) the possibility of exciting different radiation patterns and polarizations; (c) the possibility of optimizing the geometry of unit cells to tune the phase difference between modes for circular polarization; and (d) the possibility of suppressing higher order modes to reduce the pattern restoration in antenna array systems [7].

Despite the finite-sized unit cells on the MTS antenna appearing to be similar to the antenna array, several differences exist between the two. To illustrate, the typical antenna array designed for classical systems has a narrow bandwidth, while the conventional MTS antenna usually has a broad bandwidth [17]. Additionally, the space between unit cells in the antenna array can result in antenna coupling, and should be carefully considered [17]. However, the gaps between unit cells in the MTS antenna, allow for more design freedom in antenna design, and the unit cells on the MTS layer will be considered as a whole system rather than treating each unit cell individually to analyze the excited modes.

2.2.2 Design Methods of MTS Antenna

2.2.2.1 Dispersion Property Analysis Method

2.2.2.1.1 Parameter definition in dispersion property method

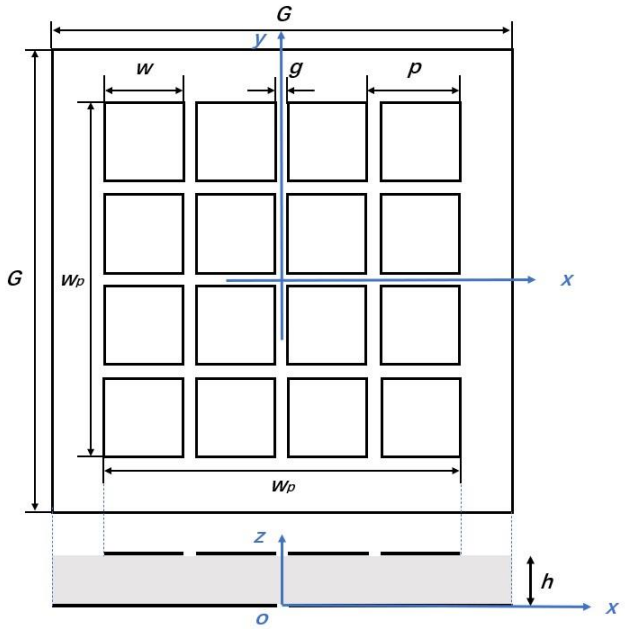

Figure 2.7. Geometry of the aperture-coupled fed mushroom antenna [3, 5].

The geometry of the aperture-coupled fed mushroom antenna is illustrated in Fig. 2. 7. Fig. 2. 7 contains three layers: an MTS layer, a substrate layer and a ground plane layer.

The MTS layer has width w of unit cell and gap g between neighboring unit cells. The period p refers to the width of the unit cell added to the gap between unit cells, namely, $p=w+g$. The number of the unit cells along the x- and y-axis directions is N_x and N_y, respectively. Since the numbers of the unit cells along x- and y-axis directions in Fig. 2. 7 are the same, the unit cell array along x- or y-axis directions is defined as W_p. $W_p=N_{xp}$-g. The unit cell array is assumed to have an additional extended length at each end, which is defined as L.

The size G is defined as the substrate size, and the height and the dielectric constant of the substrate are h and ε_r, respectively.

The corresponding antenna performance is analyzed from the dispersion property of the unit cell on the MTS layer. The dispersion property describes the dispersion effect on the properties of waves in a medium and refers to the relationship between wavenumber and frequency.

Dispersion relations are more commonly expressed in terms of the angular frequency and wavenumber [3]. The unit cell in Fig. 2. 7 does not have shorting pins connected to the ground plane, and thus, only the right-handed (RH) dispersion branch is analyzed while the left-handed (LH) dispersion branch is absent.

2.2.2.1.2 Design steps

Assuming the TM_{10} and anti-phase TM_{20} modes can be excited in the MTS antenna proposed in Fig. 2. 7, after combining the dispersion property of the unit cell with that of TM_{10} mode and anti-phase TM_{20} mode, respectively, two intersection points could be found to estimate the resonant frequencies of the TM_{10} and anti-phase TM_{20} modes from the dispersion diagram, respectively. As such, Equation 2. 6 can be combined with Equations 2. 4 and 2. 5, respectively.

The equations for estimating the resonant frequencies of two modes are listed as follows:

$$\frac{\beta_{mr} \cdot p}{\pi} = \frac{1-\frac{2 \cdot \beta_{eff} \cdot \Delta L}{\pi}}{N_x} \tag{2. 4}$$

$$\frac{\beta_{mr} \cdot p}{\pi} = \frac{1-\frac{2 \cdot \beta_{eff} \cdot \Delta L}{\pi}}{\frac{N_x}{2}} \tag{2. 5}$$

$$\beta_{eff} = \frac{2 \cdot \pi \cdot f \cdot \sqrt{\varepsilon_{reff}}}{c} \tag{2. 6}$$

where β_{mr} is the propagation constant of the unit cell; β_{eff} is the propagation constant in the effective extend length ΔL at each end along the resonant direction because of the fringing field effect; p is the period of unit cell; N_x is the number of the unit cells along the x-direction; f is the resonant frequency; and c is the speed of light in vacuum.

For Equation 2. 6, the effective dielectric constant ε_{reff} can be obtained from the following equations:

$$\frac{\Delta L}{h} = 0.412 \cdot \frac{(\varepsilon_{reff}+0.3) \cdot (\frac{W_p}{h}+0.262)}{(\varepsilon_{reff}-0.258) \cdot (\frac{W_p}{h}+0.813)} \tag{2. 7}$$

$$\varepsilon_{reff} = \frac{\varepsilon_r+1}{2} + \frac{\varepsilon_r-1}{2} \cdot (1+\frac{12h}{W_p})^{-\frac{1}{2}} \tag{2. 8}$$

where W_p is the length of unit cell array; h is the height of the substrate; and ε_r is the dielectric constant of the substrate.

The unit cell in Fig. 2. 7 was taken as an example to show the frequency estimation process of the aforementioned analysis method. Fig. 2. 8 shows the dispersion diagram of the unit cell in Fig. 2. 7, which could be obtained from the full-wave CST simulation. The dispersion property of the unit cell is represented by the solid line, while the dispersion properties of the TM_{10} and anti-phase TM_{20} modes are represented by two different dotted lines. An observation can be made from Fig. 2. 8 that two intersection points exist between the solid line and two dotted lines, respectively. Thus, the frequencies were estimated to be around 5.1 and 5.7 GHz.

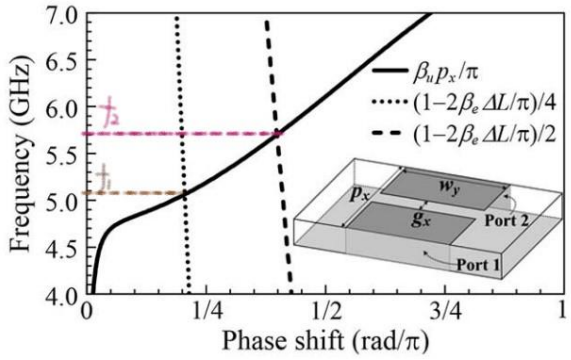

Figure 2.8. Dispersion diagram of the unit cell [18].

2.2.2.1.3 Advantages and disadvantages of dispersion property method

Through the analysis method of the dispersion diagram, more information is provided on how the unit cell works, as well as the relationship between the unit cell and the estimated frequencies. However, there are still a number of drawbacks. The first drawback is that the boundary setting of the unit cell in the dispersion diagram is infinite, while the boundary setting in a real MTS antenna is finite. The second drawback is that the dispersion property is suitable for analyzing the uniform unit cell, but not suitable for analyzing non-uniform unit cells on the MTS layer. Moreover, the frequency estimation was made according to the dispersion diagram, which was simulated by CST. If the frequency estimation needs to be made from analyzing the antenna structure, rather than from a simulation, such analysis method will not be beneficial.

2.2.2.2 Characteristic Mode Analysis Method

2.2.2.2.1 Basics in Characteristic Mode Analysis

Characteristic modes involve typical eigenfunctions, and are orthogonal over both the source region and the sphere at infinity. On a conducting body with arbitrary geometry, characteristic

mode analysis (CMA) generates a set of orthogonal currents, and the inherent resonance mode is used to represent the existing current patterns of a conducting body. The aforementioned modes depend on the geometry of the conducting body but are independent of the feed. According to the specific aim of the designer, several modes can be selected (excited) while others can be ignored (suppressed). The mode excitation is related to the structure and the location of the feed [19, 20].

The generalized eigenvalue equation is represented by:

$$X(J_n) = \lambda_n R(J_n) \tag{2. 9}$$

where λ_n is the eigenvalue; J_n is the eigencurrent; X and R are the imaginary and real parts of an impedance matrix Z, which is achieved from the electric field integral equation [21]; n denotes the index of the order of each mode. When λ_n=0, the mode is resonant. By illustration, different modes excited at different frequencies can exist in a conductor with fixed geometry and size. The frequency at which λ_n=0 is regarded as the resonant frequency of the mode, and the mode with the lowest resonant frequency is regarded as the fundamental mode of the conductor.

The total current on the conductor can be described as the sum of the orthogonal components [22]:

$$J = \sum_{n=1}^{\infty} \frac{V_n^i J_n}{1+j\lambda_n} \tag{2. 10}$$

where λ_n, V_n^i and J_n are the eigenvalue, modal excitation coefficients and modal current for the n^{th} mode, respectively. Modal excitation coefficient represents the coupling between the current of the excitation source and that of the n^{th} mode. The higher the coupling value, the greater the current contribution under the external source.

Research on the variation of the eigenvalue with frequency is meaningful in antenna design, since information on the resonant frequency of modes is provided. However, another representation referred to as modal significance (MS) is preferred, which is inversely proportional to the eigenvalue.

$$MS_n = \left|\frac{1}{1+j\lambda_n}\right| \tag{2. 11}$$

MS represents the normalized amplitude of the current modes [22], and the term depends on the geometry and size of the conducting, but is independent from the excitation. The maximum value of *MS* is 1, and the nearest the *MS* value to 1, the most effectively the mode contributes to the conductor radiation.

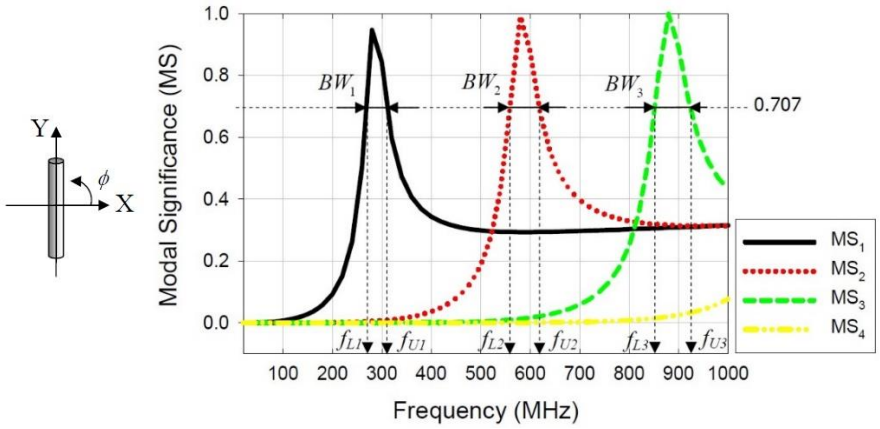

Figure 2.9. Modal significance of the first three modes versus frequency of a dipole structure [19].

Fig. 2. 9 shows the modal significance of the first three modes of a dipole structure versus frequency. The radiating bandwidth of a mode BW_n is defined as the range of frequencies within which the mode radiated power is larger than half power radiated at resonance. Half power at resonance corresponds to a reduction of the normalized current by a factor $\sqrt{2}$, where MS=1/$\sqrt{2}$=0.707. Therefore, the radiation bandwidth of a mode BW_n is described as a proportion of frequency difference over the resonant frequency of the mode. Namely, $BW_n = \frac{f_U - f_L}{f_{res}}$, where f_{res} is the resonance frequency of the mode; and f_U and f_L are the upper and lower constraints, respectively.

If an antenna is to be designed using characteristic mode method, the following steps can be taken as the reference [19]:

Step 1: Firstly, import the antenna structure (conducting) without the excitation. (The characteristic currents and fields of the conducting import are calculated. The resonance frequency of the modes present in the conducting import and corresponding radiating behaviors are determined from the eigenvalue.)

Step 2: Secondly, change the geometry and size of the antenna (conducting) until the desired resonant frequency or desired radiating behavior is achieved.

Step 3: Finally, choose the optimum feed position and feed structure according to the modal current distributions of the desired modes in the optimized antenna.

2.2.2.2.2 Design Steps

Based on the advantages of characteristic modes, such as source-free, the MTS antenna was recently analyzed using CMA. One MTS antenna was designed using CMA [4], with the aim of designing a broadband MTS antenna with a directional radiation pattern for wireless communication. According to such example, studying and selecting modes with directional radiation patterns at different frequencies, and exciting them together appear to be the aim when designing such antennas.

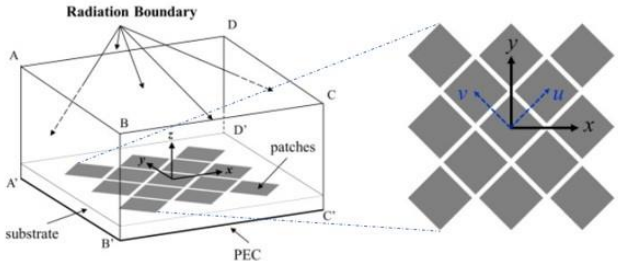

Figure 2.10. The boundary setting and the geometry of MTS [4].

The MTS geometry was simulated using the moments-based CMA tool in the simulation software CST MWS. As shown in Fig. 2. 10, five radiation boundaries (ABB'A', BCC'B', CDD'C', DAA'D', ADCB) were set as open boundary while the remaining (A'B'C'D') were set as PEC boundaries. Hence, the unit cells on the MTS layer were meshed and the electrical currents on the unit cells were solved.

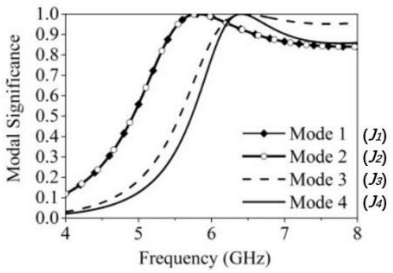

Figure 2.11. Modal significances (MSs) of the first four modes in MTS structure mentioned in Fig. 2.9 [4].

The modal significances (MSs) of the first four modes of the MTS structure shown in Fig. 2. 10 are presented in Fig. 2. 11. In the CMA simulation results, J_1 represents the modal current

of the fundamental MTS mode. Fig. 2. 12 shows the corresponding modal currents and modal radiation patterns of the first four modes excited in Fig. 2. 11. The black arrows indicate the direction of the modal current.

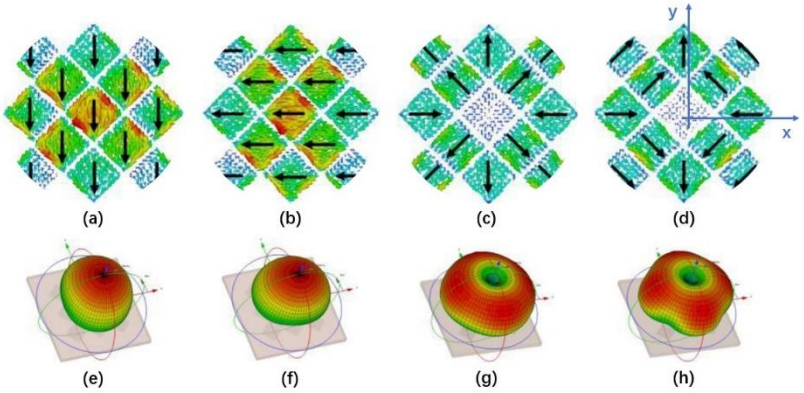

Figure 2.12. Modal currents and modal radiation patterns of the first four modes in MTS structure mentioned in Fig. 2.10 [4]. Modal currents (a) J_1, (b) J_2, (c) J_3, (d) J_4. Modal radiation patterns (e) J_1, (f) J_2, (g) J_3, (h) J_4.

As demonstrated in Fig. 2. 12(a) and (b), the first two modes, J_1 and J_2, were a pair of orthogonal modes, which both resonated at around 5.9 GHz. The modal current J_1 was always in the same direction, which induced the directional modal radiation pattern shown in Fig. 2. 12(e). Similarly, the modal current J_2 was also in the same direction, but the direction of J_2 can be seen as rotating 90° based on the direction of J_1. The other two modes, J_3 and J_4 were both self-symmetrical along the x-axis and the y-axis, respectively. Such distribution led to a null appearing at the boresight of the radiation pattern (shown in Fig. 2. 12(g) and (h)) because of the reversed modal currents, as shown in Fig. 2. 12(c) and (d). An observation can be made from Fig. 2. 12(g) and (h) that the radiation patterns of J_3 and J_4 were not directional, and thus, J_3 and J_4 could not be regarded as desired modes. Conversely, J_1 and J_2 could be regarded as desired modes, and exciting either one of the two modes would generate a linearly polarized antenna.

Additionally, according to Fig. 2. 12(a), (c) and (d), the maximum modal current of J_1 existed at the center unit cell, while the minimum modal currents of J_3 and J_4 appeared at the center unit cell. Cutting a slot at the center unit cell would be beneficial for selectively exciting the desired mode J_1. Fig. 2.13 depicts the process of modal significance variation from an MTS structure to an MTS structure with a center slot. Compared with the modal significance of the MTS structure, that of the MTS structure with a center slot was slightly different, owing to the

resonant frequencies of J_1 and J_2 being different because of the asymmetrical MTS structure with a center slot along the x- and y-axis. The resonant frequencies of J_3 and J_4 were not affected since the center slot was positioned at the minimum modal current.

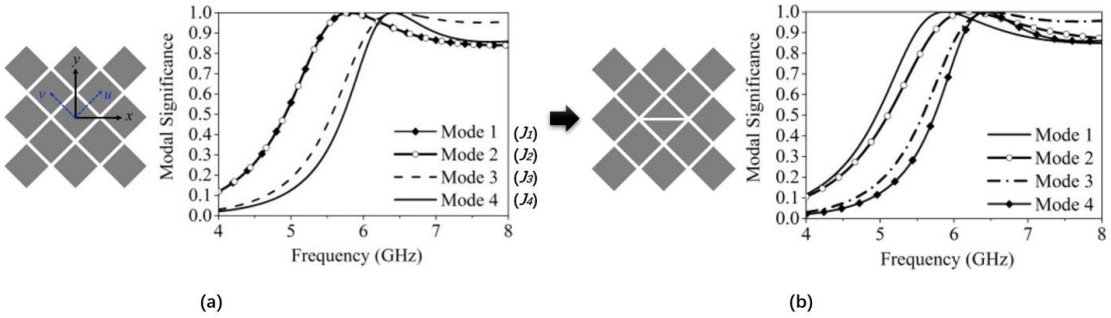

Figure 2.13. Modal significances of (a) MTS structure and (b) MTS structure with a center slot [4].

To improve the broadband performance, the other mode with directional radiation patterns at different frequencies needed to be excited. Thus, further exciting the slot at the center unit cell could help excite the other 'slot mode'. To further excite the center slot, a slot on the ground plane was introduced, as shown in Fig. 2. 14(b). Since both unit cells on the MTS layer and the ground plane with a slot were meshed, six radiation boundaries were set as open boundaries, as shown in Fig. 2. 14(a).

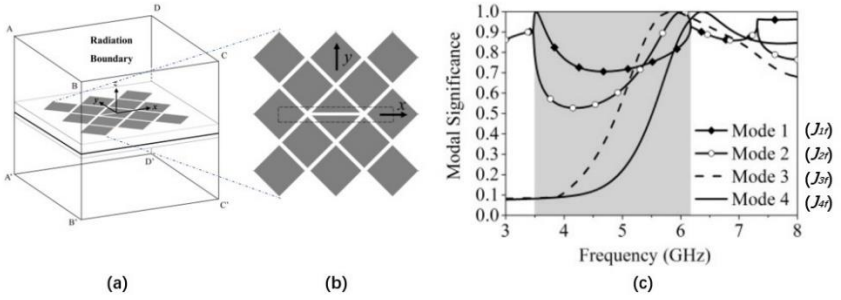

Figure 2.14. MTS structure with a center slot [4]. (a) Boundary setting. (b) Geometry. (c) Modal significance.

The modal significances of the first four modes in MTS structure with a center slot are shown in Fig. 2. 14(c). J_{1f} is newly introduced because of the coupling between the slot at the center unit cell and the slot on the ground plane. The resonant frequency of each mode was decided from the peak value of modal significance, and thus, the resonant frequencies of J_{1f}, J_{2f}, J_{3f} and J_{4f} were 3.5, 6.0, 5.85 and 6.4 GHz, respectively.

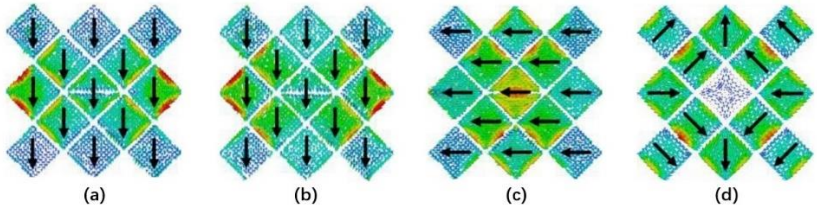

Figure 2.15. Modal current of MTS structure with a center slot [4]. (a) J_{1f}, (b) J_{2f}, (c) J_{3f}, (d) J_{4f}.

The corresponding modal currents of MTS structure with a center slot is displayed in Fig. 2.15. Modal current J_{1f} had the same direction along the y-axis, which is the modal current of the slot mode. Modal current J_{2f} is similar to the modal current J_1 mentioned in Fig. 2. 12(a), which can be attributed to the fundamental MTS mode. Modal current J_{3f} is also similar to the modal current J_2 in Fig. 2. 12(b). Modal current J_{4f} is similar to the modal current J_4 in Fig. 2. 12(d).

Finally, to successfully excite two modes with directional radiation patterns, the appropriate position and type of feed had to be selected. Since the two desired modes of J_{1f} and J_{2f}, which are shown in Fig. 2. 15(a) and (b), both had maximum modal currents at the two ends of unit cells, the desired feeds had to be positioned at the maximum modal current positions. As such, the aperture-coupled feed with maximum current distributions at two ends of the horizontal aperture were selected to effectively excite J_{1f} and J_{2f}, simultaneously.

The process of designing an MTS antenna assisted by CMA was described in this section. Notably, the current density distribution bar was not present in the described example because the related paper did not provide such information.

2.2.2.2.3 Advantage and Disadvantage of Characteristic Mode Analysis

There are mainly two advantages of using CMA to design an MTS antenna. The first advantage is that the complex boundary setting is considered rather than the period boundary environment, and thus, the estimation of the resonant frequencies would be more accurate. The second advantage is that the 'source-free' property of CMA can be used to analyze the mode more clearly. As an example, in the described MTS antenna design, the slot mode is identified when adding the aperture (the aperture-coupled feed structure). Otherwise, there will be uncertainty in terms of whether the J_{1f} mode is from the MTS layer or the ground plane layer. The third advantage is that CMA can be used to analyze either the uniform or non-uniform unit cells, which broadens the analysis range of MTS antennas. However, the resonant frequencies of the

desired mode are still obtained from a simulation tool, and thus, investigating the relationship between MTS geometry and related resonant frequencies will be more beneficial.

2.2.2.3 Other Analysis Method

In addition to the dispersion property method and the CMA method, other analysis methods can also be used to explore the properties of MTS, such as the equivalent circuit. The equivalent circuit analysis method can be used to represent the complicated MTS antenna models and quantify the impact of the unit cell structure on the performance. The equivalent circuit analysis method is usually used to estimate the fundamental resonant frequency from the unit cell structure [23].

An MTS antenna design with a composite right-/left-handed (CRLH) structure is a common example, and is typically analyzed in terms of the equivalent circuit and dispersion property. The CRLH structure includes both right-handed and left-handed structures. The right-handed structure is achieved from simultaneous positive permittivity and permeability while the left-handed structure is obtained from simultaneous negative permittivity and permeability.

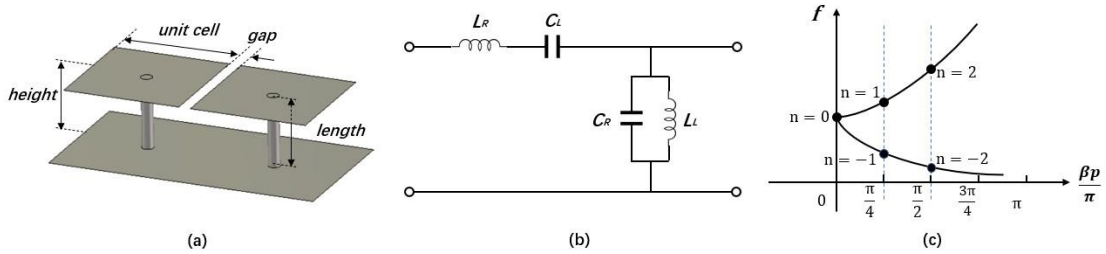

Figure 2.16. Composite right-/left-handed (CRLH) structure. (a) 3D view. (b) equivalent circuit. (c) dispersion diagram.

Fig. 2. 16(a) shows two adjacent CRLH unit cells. Each CRLH unit cell consists of a square radiating element, a ground plane, and a shorting pin connecting the radiating element with the ground plane. The property of the CRLH structure can be analyzed using the corresponding equivalent circuit, as shown in Fig. 2. 16(b). For the structure, the radiating element is equivalent to a series inductance L_R; the gap between the radiating element layer and the ground plane layer is equivalent to a shunt capacitance C_R; the gap between adjacent unit cells is modeled with a series capacitance C_L; and the shorting pin is modeled with a shunt inductance L_L.

The resonant frequencies of series LC circuit and shunt LC circuit are defined from the equivalent circuit of the CRLH unit cell model [18]:

$$\omega_{se} = \frac{1}{\sqrt{L_R C_L}} \tag{2. 12}$$

$$\omega_{sh} = \frac{1}{\sqrt{L_L C_R}} \tag{2. 13}$$

If $\omega_{se} \neq \omega_{sh}$, then the case is unbalanced, which means that there is a stopband in the dispersion diagram. If $\omega_{se} = \omega_{sh}$, then the case is balanced, which is used for designing a broad bandwidth.

The propagation constant of the CRLH unit cell can be determined by the following equation [18]:

$$\beta_{CRLH} = s(\omega)\sqrt{\omega^2 L_R C_R + \frac{1}{\omega^2 L_L C_L} - \left(\frac{L_R}{L_L} + \frac{C_R}{C_L}\right)} \tag{2. 14}$$

where,

$$s(\omega) = \begin{cases} -1, if\ \omega < \omega_{se} = \min\left(\frac{1}{\sqrt{L_R C_L}}, \frac{1}{\sqrt{L_L C_R}}\right) \\ +1, if\ \omega > \omega_{sh} = \max\left(\frac{1}{\sqrt{L_R C_L}}, \frac{1}{\sqrt{L_L C_R}}\right) \end{cases} \tag{2. 15}$$

Notably, Fig. 2. 16(c) shows a balanced case with a smooth transition from LH to RH propagation in the dispersion diagram. Owing to the negative and zeroth-order resonance in the CRLH antennas, there is more freedom to design antennas with multiple but narrow bandwidths [3].

2.3 Performance Enhancement in Metasurface-Based Antennas

MTS antennas with finite unit cells have several unique properties, including the ability to excite multiple modes on the MTS layer with different radiation patterns or polarizations and tune the resonant frequencies of multiple modes [7]. Due to such properties, MTS antennas can be designed to have a broad bandwidth or diverse radiation patterns. Several related studies on MTS antennas have recently been conducted. An overview and a detailed discussion of the research is provided in this section.

2.3.1 Metasurface-Based Antennas with Bandwidth Enhancement

As wireless communication systems have rapidly developed, there have been significant increases in the requirements for broad bandwidth antenna design. Compared with conventional microstrip patch antennas, MTS antennas can be more easily designed with broadband performance due to the radiating gaps of such antennas. The current methods for expanding the bandwidth of the MTS antenna are mainly applied to two parts: the MTS layer and the feed layer.

In terms of the MTS layer, researchers have focused on exciting more MTS modes at different frequencies to broaden the bandwidth. The first excited mode is the fundamental MTS mode. In one previous study on the higher MTS mode [3], the TM_{20} mode was excited by the existing aperture-coupled feed structure. The resonant frequencies of the fundamental TM_{10} mode and TM_{20} mode were estimated from the equations related to the propagation constant and the dispersion diagram of the unit cell. The frequency difference between the fundamental TM_{10} mode and the excited TM_{20} mode could be tuned by the gap width on the MTS layer, indicating that the bandwidth could be shrunk or extended by tuning the gap width. Fractional bandwidth with 25% is acquired at around 5 GHz. The mode analysis in the previous study [3] was designed according to the dispersion relation, and such method has several drawbacks, which are mentioned in Section 2.2.2.1.3.

To overcome some of the problems of the dispersion analysis method, an MTS antenna design based on the CMA method was proposed in one study [4]. The bandwidth was composed of the fundamental TM_{10} mode and slot mode. The slot mode was excited by the coupling between the slot on the center unit and the aperture on the ground plane. Similarly, the frequency of the slot mode could be tuned by the slot length. Hence, the bandwidth could be improved accordingly. The proposed MTS antenna could achieve 31% fractional bandwidth at around 5.5 GHz.

In addition to the exciting mode from the MTS layer, bandwidth improvement can also be realized from the feed layer. In a previous study [24], a pair of edge-fed slots assisted by a fictitious short was designed to excite the MTS layer, as shown in Fig. 2. 17(a). With the MTS layer, the pair of edge-fed slots could excite the fundamental mode and the higher mode. The length of the fictitious short could tune the frequency difference between the two modes.

Further, the feed structure could provide a better polarization purity over the bandwidth, and the antenna could obtain 21% fractional bandwidth at around 6.25 GHz.

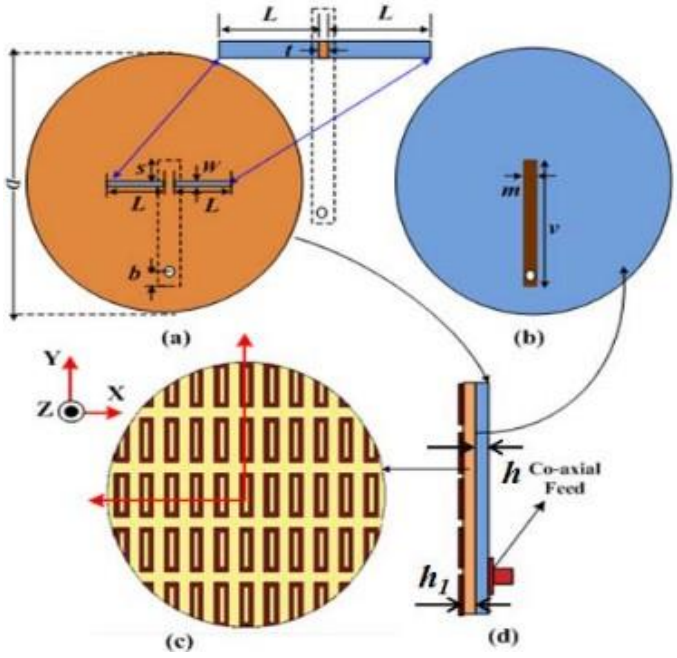

Figure 2.17. The structure of broadband directive slot antenna loaded with cavities and single/double layer(s) of MTS [24]. (a) Slot antenna bottom view. (b) Slot layer top view. (c) MTS layer. (d) MTS antenna side view.

Despite the aforementioned MTS design allowing for the bandwidth to be extended from the feed layer rather than the MTS layer alone, only TM modes are excited. To explore the mode diversity to increase the design freedom, both the TM and TE modes were excited in one MTS antenna design [6]. The TM and TE modes were excited simultaneously because of the proposed L-probe feed, as shown in Fig. 2. 18(b). The vertical part in the L-probe feed structure could excite the TM mode along the x-axis, while the horizontal part in the feed could excite the TE mode along the y-axis of the MTS layer. Similar to the method of estimating the resonant frequency of the TM mode, that of the TE mode could also be estimated from the dispersion relation, but along the y-axis of the MTS layer. The proposed MTS antenna could realize 34.5% fractional bandwidth at around 5.5 GHz.

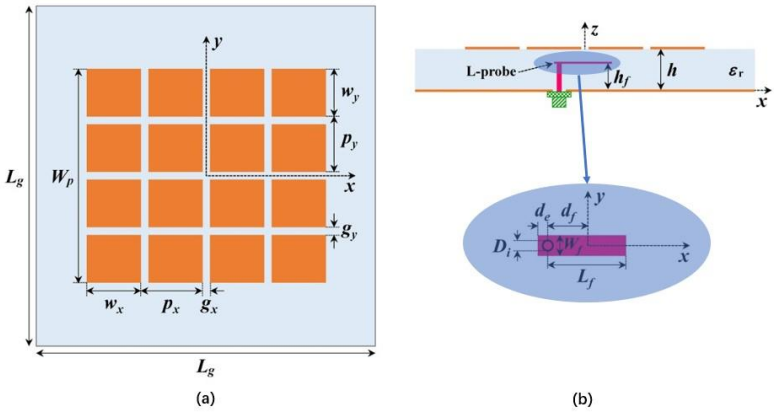

Figure 2.18. Configuration of the L-probe fed MTS antenna. (a) Top view of MTS. (b) Side view and the top view of L-probe [6].

Different broadband MTS antenna designs are proposed. The bandwidth in some antennas is improved from the different structures while that in some antennas is increased from different types of modes. However, the bandwidths of all the above-mentioned MTS antenna designs are not wide enough. To achieve a broader bandwidth, [25] proposed an MTS antenna fed by coplanar waveguide aperture coupled structure. The stair-shape feeding aperture shown in Fig. 2. 19 greatly increase the antenna bandwidth because the special stair-shape aperture makes the input impedance of the antenna be adjusted for wideband characteristic. The fractional bandwidth of this MTS antenna is 67.3% at around 7 GHz, which is much broader than the other mentioned designs.

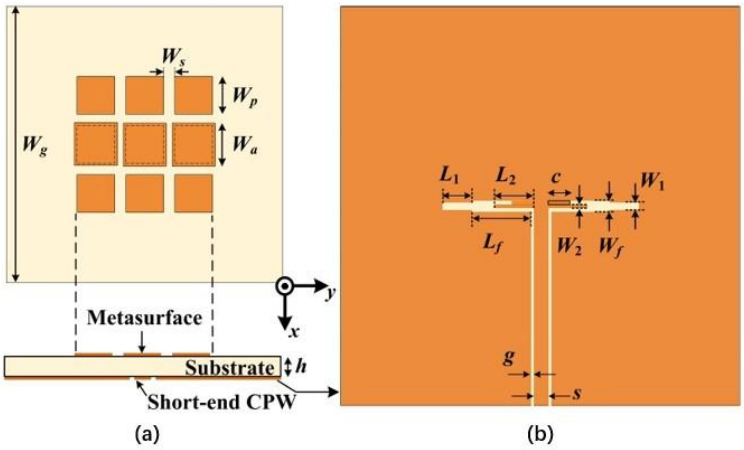

Figure 2.19. The geometry of a broadband coplanar waveguide (CPW)-fed aperture coupled MTS antenna [25].

The broadband antenna design is applied so that more frequencies can be covered in wireless communication. However, in certain applications, dual-band performance is preferred over

broadband. Two scenarios of a base station and a satellite can be taken as examples. In the base station application, an antenna may be required to simultaneously cover two frequency bands that are close to each other in terms of the base station frequency range, in which the frequencies between the two bands are rejected [26]. In the satellite application, a dual-band antenna is also desired since both a low-frequency mode and a high-frequency mode are required for low-speed uplink and high-speed downlink communications, respectively [27].

Notably, depending on different applications, the ratio of two bands in a dual-band antenna needs to be considered. In one previous study [28], a dual-band MTS antenna with a large frequency ratio for 5G application was proposed. One band operated at sub-6 GHz while the other band operated at millimeter (mm)-wave. The unit cell of the MTS contained the subcell of a square ring and an inner square patch, which featured different characteristics at the S-band and K-band, respectively. The subcell of a square ring was generated at the S-band by the aperture-coupled feed, whereas an inner square patch was generated at the K-band by the plane wave feed, shown in Fig. 2. 20. The aperture-shared MTS antenna could realize 23.45% and 4.8% fractional bandwidth at S-band (3.2-4.05 GHz) and K-band (25.22-26.46 GHz), respectively.

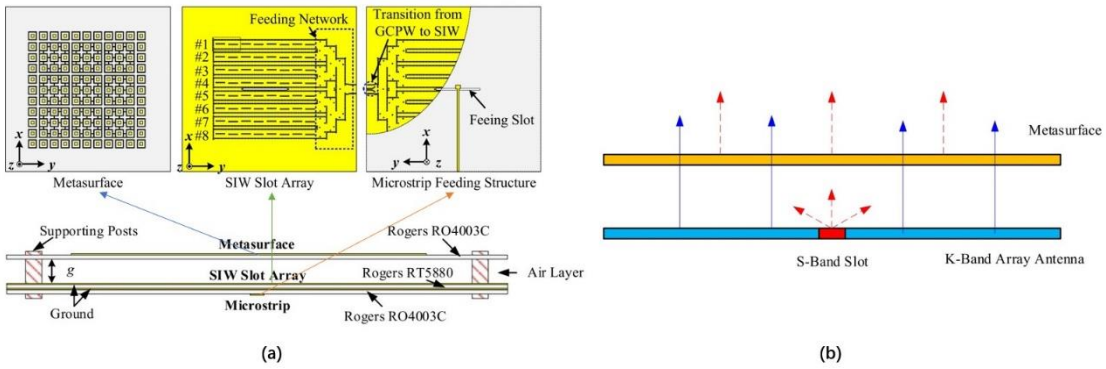

Figure 2.20. Shared-aperture antenna [28]. (a) Geometry of separated layers and side view of antenna. (b) Working mechanism of antenna.

By contrast, in another study [29], a dual-band MTS antenna with a small frequency ratio for wireless local area network (WLAN) and 5 GHz applications was presented. Two bands were generated from the CRLH structure, as shown in Fig. 2. 21. The resonant frequencies of the two bands could be estimated from the equivalent circuit and dispersion diagram of the unit cell, and the frequency ratio could be evaluated accordingly. The MTS antenna with the CRLH structure could achieve two fractional bandwidths with 25.8% and 15.1% at around 2.6 and 5.6 GHz, respectively.

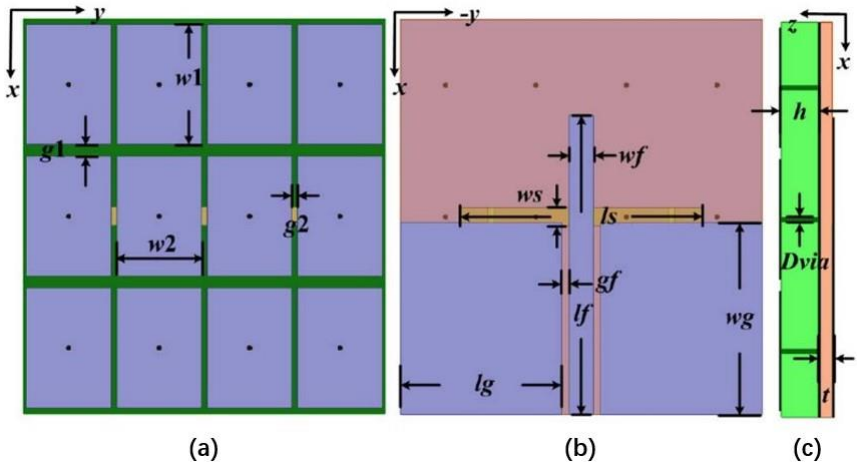

Figure 2.21. Geometry of dual-band MTS antenna with CRLH structure [29]. (a) Top view. (b) Back view. (c) Side view.

2.3.2 Metasurface-Based Antennas with Beamwidth Enhancement/Pattern Diversity

Since MTS antennas can achieve different radiation patterns by exciting different modes, research on MTS antennas with different radiation patterns can be regarded as meaningful. Among the recent MTS antenna designs, the radiation pattern has generally been designed to be directional, because such antennas are usually used in wireless communication systems. However, if a pattern-diverse MTS antenna is required, more possibilities for MTS antenna with various radiation patterns, such as omnidirectional, endfire, and others, should be explored.

In general, an MTS antenna with pattern diversity can be achieved through mechanical or electrical means. In one previous study [30], a pattern reconfigurable MTS antenna was designed based on a planar semi-circular MTS layer, shown in Fig. 2. 22. The pattern reconfigurable could be realized by rotating the MTS around the center of the patch antenna. However, such method is achieved through mechanical means, and methods achieved through electrical means are usually preferred.

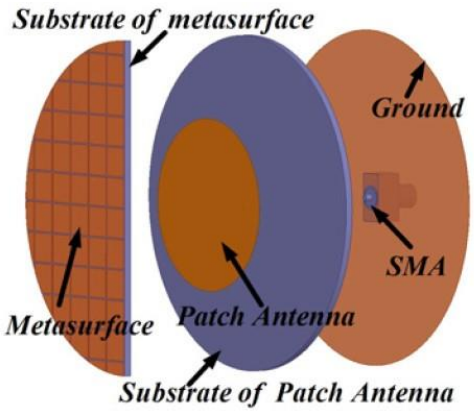

Figure 2.22. Assembly schematic of pattern reconfigurable MTS antenna [30].

In several designs, electrical methods were used to realize MTS antennas with different radiation patterns [31], [32], [33]. In one previous study [31], an MTS antenna with an omnidirectional radiation pattern was developed, which was excited according to a desired characteristic mode and fed by a one-to-four power divider, as shown in Fig. 2. 23. The MTS antenna had 16.6% fractional bandwidth at around 5.2 GHz. The bandwidth of the developed antenna [31] was relatively narrow, and thus, further research is needed on broader MTS antennas with omnidirectional radiation patterns.

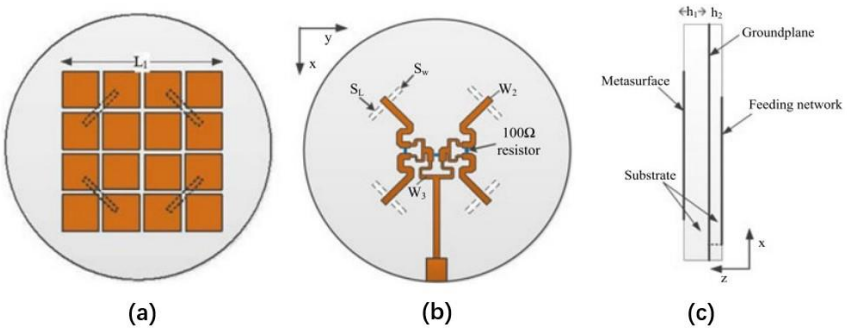

Figure 2.23. Structure of omnidirectional MTS antenna [31]. (a) Top view. (b) Bottom view. (c) Side view.

To improve the bandwidth of omnidirectional MTS antennas, a novel nonuniform tapered MTS antenna was designed in one previous study [32], with 33.1% fractional bandwidth. The antenna bandwidth could be improved by changing the ratio between two excited frequencies. The ratio could be tuned by changing the radiating gap positions on the MTS layer, as shown in Fig. 2. 24.

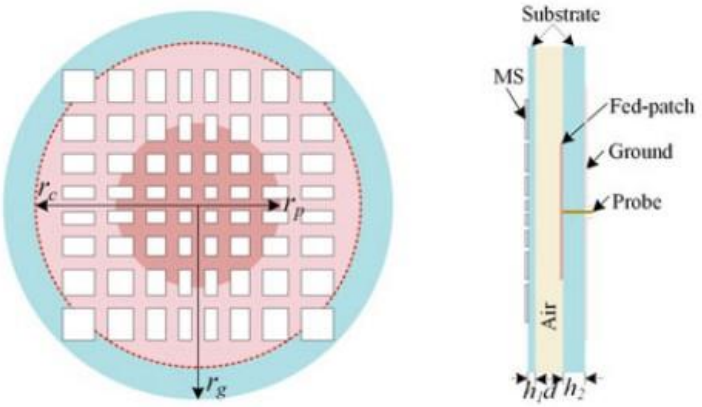

Figure 2.24. Geometry of omnidirectional surface-wave MTS antenna [32]. (a) Top view. (b) Side view.

In addition to omnidirectional radiation patterns, another MTS antenna with an endfire radiation pattern was designed in one previous study [33]. The endfire pattern was excited by an open-end substrate integrated waveguide (SIW) feed, as shown in Fig. 2. 25. The MTS antenna had 37% fractional bandwidth at 32.65 GHz. The antenna design was applied for mm-wave communication technology, which could potentially be a candidate for the next generation of communication systems.

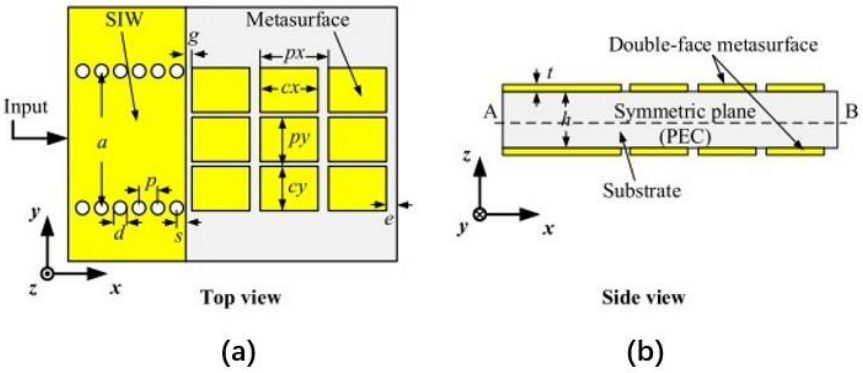

Figure 2.25. Configuration of substrate-Integrated waveguide- (SIW) fed endfire MTS antenna [33].

As well as antenna designs with different radiation patterns, MTS antenna designs with pattern diversity are also appealing. Pattern diversity antennas can be used in a variety of applications [35]-[37]. For example, by redirecting the null location of the radiation pattern, a pattern diversity antenna can prevent interference from noise sources originating from a known direction [37]. Such antennas can also cover a large area by redirecting the main beam [35], in addition to having the potential to enable numerous independent far-field radiation patterns,

which is beneficial for improving the performance and environmental adaptability of mobile systems [36].

In one previous study [34], an MTS antenna by dual-port excitations with different patterns was proposed. The differential probe feed excited the broadside mode, while the stepped probe excited the conical mode, as shown in Fig. 2. 26. Additionally, an appropriate position choice of the two types of feeds ensured good isolation between the two ports. To provide a more systematic design method for MTS antennas with pattern diversity, CMA was introduced due to the advantages of being accurate and source-free. The proposed MTS antenna could realize 11.2%/30.8% fractional bandwidth at 5.3 GHz.

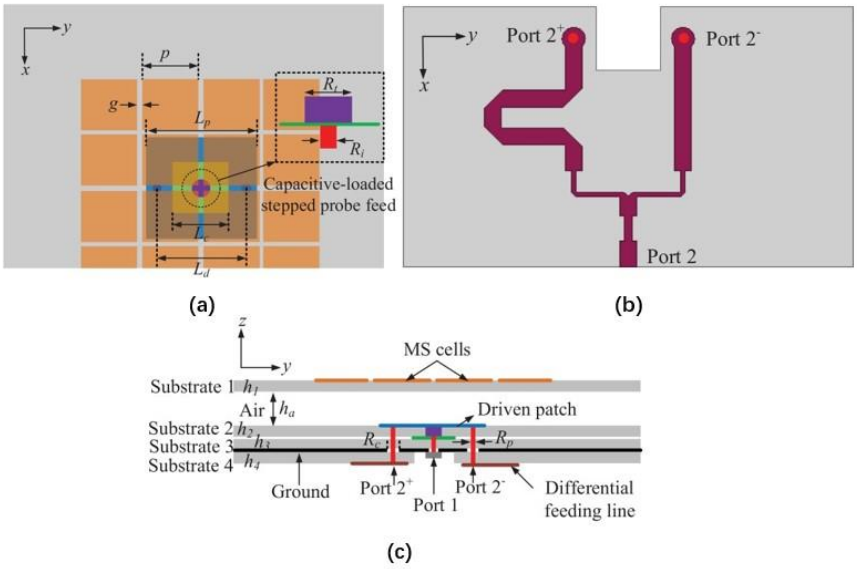

Figure 2.26. Geometry of pattern-diversity MTS antenna [34]. (a) Front view. (b) Feed view. (c) Side view.

To realize pattern diversity, another MTS antenna with two excited modes was presented in previous research [38]. The two modes were successfully excited on the MTS layer to achieve pattern diversity, shown in Fig. 2. 27. Additionally, CMA was used to suppress the higher order mode (HOM) to improve the distorted radiation pattern. The proposed MTS antenna with pattern diversity had 20.2% fractional bandwidth at around 6 GHz, and was designed for unmanned aerial vehicle communications. The main limitation of the design is that the feeding structure for exciting the two modes is slightly complicated. As such, simpler feed methods need to be further explored.

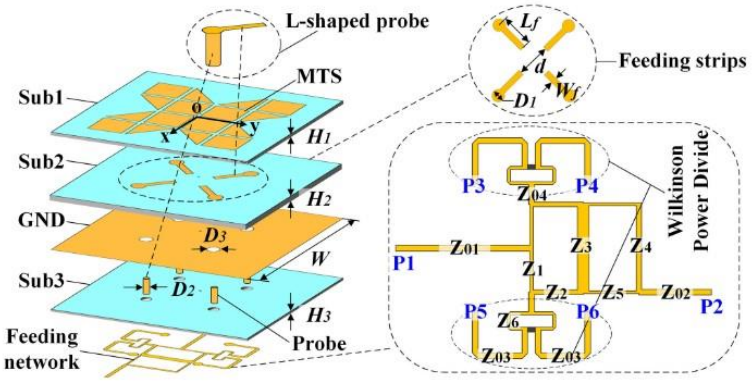

Figure 2.27. Geometry of pattern-diversity MTS antenna [38]. (a) Front view. (b) Feed view. (c) Side view.

2.4 Summary

The fundamentals of the antenna theory as well as the description of the MTS antenna are covered in this chapter. The benefits of the MTS antenna are also mentioned, which indicate that such antennas can improve the antenna performance in terms of bandwidth or beamwidth. The common analysis methods of the MTS antenna include the dispersion property method and the CMA method, which are introduced and discussed in detail. Moreover, a review of previous MTS antenna research with broad bandwidth and diverse radiation patterns is provided, which facilitates further understanding of how the current methods and technology can be used to explore the potential of MTS antennas and improve the antenna performance accordingly.

2.5 References

[1] M. Boban, A. Kousaridas, K. Manolakis, J. Eichinger, and W. Xu, "Connected Roads of the Future: Use Cases, Requirements, and Design Considerations for Vehicle-to-Everything Communications," *IEEE Vehicle Technology Magazine*, vol. 13, no. 3, pp. 110–123, 2018.

[2] Y. Feng, F. Zhang, G. Xie, Y. Guan, and J. Tian, "A Broadband and Wide-Beamwidth Dual-Polarized Orthogonal Dipole Antenna for 4G/5G Communication," *IEEE Antennas and Wireless Propagation Letters*, vol. 20, no. 7, pp. 1165-1169, 2021.

[3] W. Liu, Z. N. Chen, and X. Qing, "Metamaterial-Based Low-Profile Broadband Mushroom Antenna," *IEEE Transactions on Antennas and Propagation*, vol. 62, no. 3, pp. 1165-1172, 2014.

[4] F. Lin and Z. N. Chen, "Low-Profile Wideband Metasurface Antennas Using Characteristic Mode Analysis," *IEEE Transactions on Antennas and Propagation*, vol. 65, no. 4, pp. 1706-1713, 2017.

[5] W. Liu, Z. N. Chen, and X. Qing, "Metamaterial-Based Low-Profile Broadband Aperture-Coupled Grid-Slotted Patch Antenna," *IEEE Transactions on Antennas and Propagation*, vol. 63, no. 7, pp. 3325-3329, 2015.

[6] W. Liu, Z. N. Chen, and X. Qing, "Broadband Low-Profile L-Probe Fed Metasurface Antenna With TM Leaky Wave and TE Surface Wave Resonances," *IEEE Transactions on Antennas and Propagation*, vol. 68, no. 3, pp. 1348-1355, 2020.

[7] F. Lin and Z. N. Chen, "Recent Progress in Metasurface Antennas Using Characteristic Mode Analysis," 31 Mar.-5 Apr. 2019; Krakow, Poland; 13th European Conference on Antennas and Propagation (EuCAP 2019), pp. 1-4.

[8] C. A. Balanis, "Antenna Theory: Analysis and design", 3rd edition, John Wiley and Sons, New Jersey, 2005, pp. 1117.

[9] Antenna theory, from https://www.antenna-theory.com/

[10] V. Zuniga, N. Haridas, A. T. Erdogan, and T. Arslan, “Effect of a Central Antenna Element on the Directivity, Half-Power Beamwidth and Side-Lobe Level of Circular Antenna Arrays,” 29 Jul.-1 Aug. 2009; San Francisco, CA, USA; 2009 NASA/ESA Conference on Adaptive Hardware and Systems, pp. 252-256.

[11] Antenna – Satellite Wiki, from https://www.aero.iitb.ac.in/satelliteWiki/index.php/Antenna

[12] Introduction to Polarization, from https://www.edmundoptics.com/knowledge-center/application-notes/optics/introduction-to-polarization/

[13] W. K. Chen. The electrical engineering handbook. Academic Press, pp. 569-583, 2005.

[14] S. Leble. Waveguide Propagation of Nonlinear Waves. Springer, pp. 37-74, 2019.

[15] C. Song, “Broadband Rectifying-Antennas for Ambient RF Energy Harvesting and Wireless Power Transfer”, Ph.D. thesis, Department of Electrical Engineering and Electronics, University of Liverpool, Jul. 2017 [Online]. Available: https://livrepository.liverpool.ac.uk/3008512/

[16] F. Lin, “Study of Microwave Metasurface Antenna Using Characteristic Mode Analysis”, Ph.D. thesis, Department of Electronics, National University of Singapore, 2018 [Online]. Available: https://scholarbank.nus.edu.sg/handle/10635/150286

[17] B. Clerckx and C. Oestges, MIMO Wireless Networks (Second Edition), Elsevier Ltd., pp. 29-58, 2013.

[18] J. M. Tanabe, “Dual-band Composite Right/Left Hand Substrate Integrated Waveguide Leaky Wave Antenna Phased Array Design,” M.Sc. thesis, Department of Electrical Engineering, University of California, 2013 [Online]. Available: https://escholarship.org/content/qt2mz9765x/qt2mz9765x.pdf

[19] M. C. Febres., “Systematic Design of Antennas Using the Theory of Characteristic Modes”, Ph.D. thesis, Department of Electronics, Valencia University of Technology, Feb. 2007 [Online]. Available: https://riunet.upv.es/bitstream/handle/10251/1883/tesisUPV2594.pdf

[20] M. Stanley., “Mobile Phone Antennas for MIMO and 5G Millimetre Wave Communications”, Ph.D. thesis, Department of Electrical Engineering and Electronics,

University of Liverpool, Nov. 2018 [Online]. Available: https://livrepository.liverpool.ac.uk/3031149/

[21] R. F. Harrington and J. R. Mautz, "Theory of characteristic modes for conducting bodies", *IEEE Transactions on Antennas and Propagation*, vol. 19, no. 5, pp. 622–628, Sep. 1971.

[22] D. Wen, Y. Hao, H. Wang, and H. Zhou, "Multimode Decoupling Technique with Independent Tuning Characteristic for Mobile Terminals," *IEEE Transactions on Antennas and Propagation*, vol. 65, no. 12, pp. 6739–6749, 2017.

[23] T. L. Simpson, "A Wideband Equivalent Circuit Electric Dipoles," *IEEE Transactions on Antennas and Propagation*, vol. 68, no. 11, pp. 7636-7639, 2020.

[24] B. Majumder, "Compact Broadband Directive Slot Antenna Loaded With Cavities and Single and Double Layers of Metasurfaces," *IEEE Transactions on Antennas and Propagation*, vol .64, no. 11, pp. 4595-4606, 2016.

[25] J. Wang, "Broadband CPW-Fed Aperture Coupled Metasurface Antenna," *IEEE Antennas and Wireless Propagation Letters*, vol. 18, no. 3, pp. 517-520, 2019.

[26] W. C. Mok, S. H. Wong, K. M. Luk, and K. F. Lee, "Single-Layer Single-Patch Dual-Band and Triple-Band Patch Antennas," *IEEE Transactions on Antennas and Propagation*, vol .61, no. 8, pp. 4341-4344, 2013.

[27] D. E. Serup, G. F. Pedersen, and S. Zhang, "Dual-Band Shared Aperture Reflectarray and Patch Antenna Array for S- and Ka-Band," *IEEE Transactions on Antennas and Propagation*, 2021 (Early Access).

[28] T. Li and Z. N. Chen, "Metasurface-Based Shared-Aperture 5G S-/K-Band Antenna Using Characteristic Mode Analysis," *IEEE Transactions on Antennas and Propagation*, vol. 66, no. 12, pp. 6742-6750, 2018.

[29] Z. Wu, "Dual-Band Antenna Integrating With Rectangular Mushroom-Like Superstrate for WLAN Applications," *IEEE Antennas and Wireless Propagation Letters*, vol. 15, pp. 1269-1272, 2016.

[30] H. Zhu, "Mechanically pattern reconfigurable antenna using metasurface," *IET Microwaves, Antennas & Propagation*, vol. 9, no. 12, pp. 1331-1336, 2015.

[31] X. Yang, “Design of a Wideband Omnidirectional Antenna With Characteristic Mode Analysis,” *IEEE Antennas and Wireless Propagation Letters*, vol. 17, no. 6, pp. 993-997, 2018.

[32] G. Feng, “Broadband Surface-Wave Antenna With a Novel Nonuniform Tapered Metasurface,” *IEEE Antennas and Wireless Propagation Letters*, vol. 16, pp. 2902-2905, 2017.

[33] T. Li, “Wideband Substrate-Integrated Waveguide-Fed Endfire Metasurface Antenna Array,” *IEEE Transactions on Antennas and Propagation*, vol. 66, no. 12, pp. 7032-7040, 2018.

[34] X. Yang, “Design of a Metasurface Antenna With Pattern Diversity,” *IEEE Antennas and Wireless Propagation Letters*, vol. 19, no. 12, pp. 2467-2471, 2020.

[35] L. Sun, G. Zhang, B. Sun, W. Tang, and J. Yuan, “A Single Patch Antenna With Broadside and Conical Radiation Patterns for 3G/4G Pattern Diversity,” *IEEE Antennas and Wireless Propagation Letters*, vol. 15, pp. 433-436, 2016.

[36] S. S. Yang and K. Luk, “Design of a Wide-Band L-Probe Patch Antenna for Pattern Reconfiguration or Diversity Applications,” *IEEE Transactions on Antennas and Propagation*, vol. 54, no. 2, pp. 433-438, 2006.

[37] S. Chen, J. Row, and K. Wong, “Reconfigurable Square-Ring Patch Antenna With Pattern Diversity,” *IEEE Transactions on Antennas and Propagation*, vol. 55, no. 2, pp. 472-475, 2007.

[38] J. Liu, “A Wideband Pattern Diversity Antenna With a Low Profile Based on Metasurface,” *IEEE Antennas and Wireless Propagation Letters*, vol. 20, no. 3, pp. 303-307, 2021.

Chapter 3 Mode Analysis in Metasurface-based Antenna

This chapter presents an approach to analyze modes that exist in an metasurface (MTS). The mode study is based on a basic 3×3 MTS antenna with square solid elements. This study provides a clear physical understanding of excited MTS modes in basic MTS antennas. It offers a guideline for designing and controlling the mode resonances in MTS antenna design. The parametric studies (including beamwidth and gain) on excited MTS modes are also discussed.

3.1 Mode Analysis in MTS Antenna

3.1.1 Mode Analysis from MTS Antenna Structure

Two methods are used to analyze and verify the modes existing in the MTS antenna, respectively. The MTS antenna is analyzed from the antenna structure by antenna theory. Then, the characteristic mode analysis (CMA) method can verify whether the existing modes are due to the MTS layer or the feed layer. The reason is that once the sizes, structures, and arrangement of the unit cells are determined, an MTS is fully characterized.

Fig. 3. 1 shows a basic MTS antenna with 3×3 square solid elements. This basic MTS antenna has two layers: the MTS layer and the feeding layer. The geometry and specific details of these two layers are shown in Figure 3. 1. These two layers are coupled through an aperture and connected using a Rogers RO4003c substrate together. The heights of the two layers are 3.18 mm and 0.813 mm, respectively. This antenna is modelled and simulated using CST Microwave Studio (MWS) for current, electric (E)-field, and magnetic (H)-field distributions performance [1].

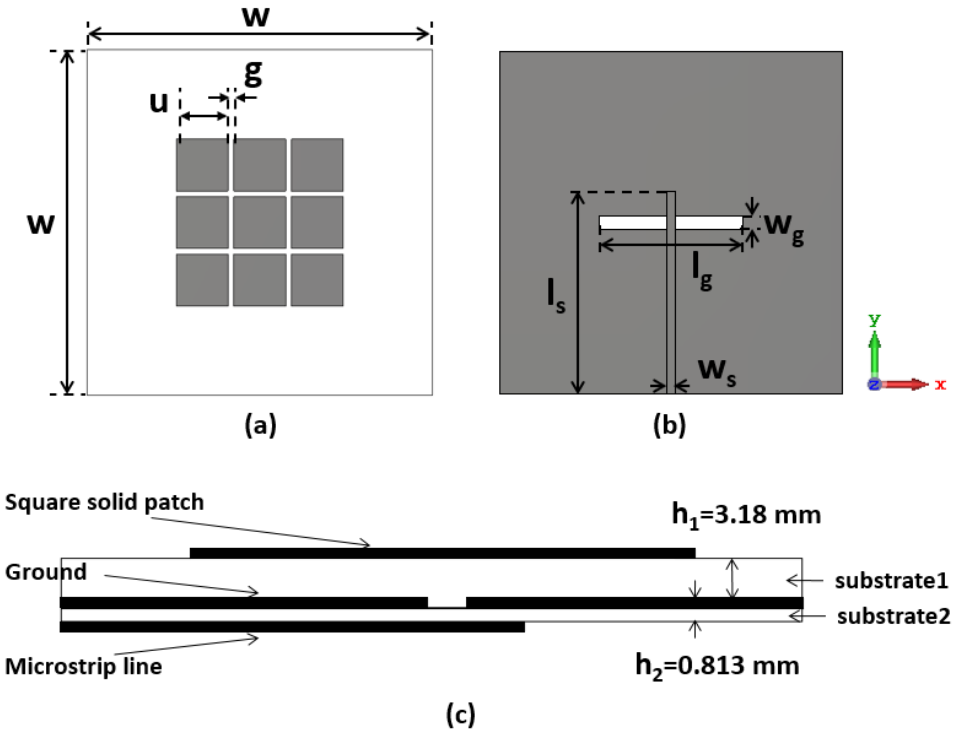

Figure 3.1. Geometry of the basic 3×3 MTS antenna with 3×3 square solid elements. (a) Top view. (b) Bottom view. (c) Side view. (W= 60 mm, u= 9 mm, g= 1 mm, l_g= 20 mm, w_g= 2.5 mm, l_s= 34.5 mm, w_s= 1.88 mm).

In the antenna theory, a moving set of charges, namely current, will have radiation. In addition, the E- and H-field distributions on the MTS look similar to the mode on the waveguide, so the mode identification method in the waveguide (namely identifying the mode from E-/H-field distributions) will be taken as the reference while identifying the mode in the MTS antenna. The current, E-field, and H-field distributions of this basic 3×3 MTS antenna will be all displayed in this section.

With the feeding structure shown in Fig. 3. 1, the basic MTS antenna is fed by a microstrip line along the y-axis. It is coupled to the MTS layer via an aperture on the ground plane. As a result, the E-field vector generated by this feeding structure is not parallel to the MTS surface. So, TE modes cannot be excited in this way. On the contrary, TM modes can be easily excited, such as the fundamental and higher TM modes.

Notably, the fundamental TM mode is excited because the electromagnetic (EM) wave will be coupled from the microstrip line (along the y-axis) to the center of the MTS via the aperture center on the ground plane. This mode is similar to the fundamental mode in microstrip patch antennas. The E-field is zero at the patch center and has a maximum magnitude on both edges.

The fundamental mode of the microstrip patch is commonly referred to as the TM_{10} mode using waveguide theory [2]-[3].

Apart from the fundamental patch TM_{01} mode, it is also possible that higher TM_{xy} modes can be excited. The values of *x* and *y* are decided by different factors, which will be discussed as follows.

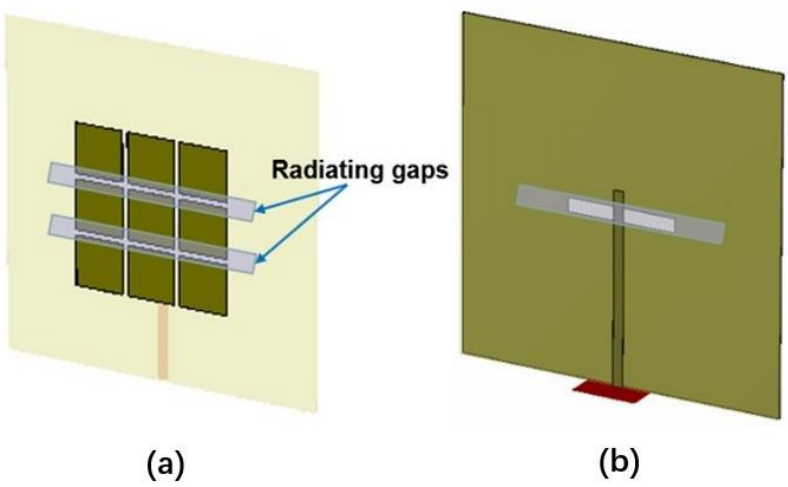

Figure 3.2. (a) MTS layer with two horizontal radiating gaps. (b) The feed structure with a horizontal aperture on the ground plane.

In the basic 3×3 MTS antenna with square solid elements, two horizontal and two vertical gaps exist between each unit cells, as shown in Fig. 3. 2. (The N×N MTS antenna has (N-1) horizontal/vertical radiating/non-radiating gaps [4].) Among these gaps in this case, two horizontal gaps are radiating while two vertical gaps are non-radiating according to the direction of the feeding structure. In this proposed aperture-coupled feeding structure, the EM wave propagates from the microstrip line to the aperture on the ground, coupled from the aperture to the horizontal gaps on the MTS layer. Under this condition, the horizontal gaps parallel to the aperture can radiate while the vertical gaps that are orthogonal cannot radiate. Additionally, the number of horizontal radiating gaps is related to the excited MTS mode types. In particular, for the excited TM_{xy} modes, '*y*' should be equal to 2 since there are only two horizontal radiating gaps in this basic MTS antenna. Thus, other modes with '*y*' unequal to 2 could be ignored in the analysis.

Differently, the '*x*' value in TM_{xy} should be odd since the EM field concentrates at the center of the feed. In the xoz plane, the magnitude of the E-field is maximum at the center and reaches a minimum at two edges. Consequently, only odd modes can be excited, and even modes are

largely suppressed ('*x*' should be odd). Therefore, TM_{1y} and TM_{3y} can be excited in this basic MTS antenna, and there are a total of three excited modes: TM_{01}, $TM_{12,}$ and TM_{32}.

3.1.2 Current/E-/H-field Distribution to Analyze MTS Modes

To verify the above analysis, the current distribution ('*I*' in Table. I), the E-field distribution ('*E*' in Table. I), and the H-field distribution ('*H*' in Table. I) of three excited modes are shown in Table. I. Normally, the current distribution of each mode is used to illustrate the radiation property of the antenna. The E- and H-field distributions are used to identify the MTS modes. The reason is that the E- and H-field distributions on the MTS look like the mode on the waveguide, so the mode identification way in the waveguide will be used as a guide here. The E-field and H-field distributions of each mode are orthogonal to each other, and these field distributions obey the right-hand rule.

The current, E-field, and H-field distributions of three excited modes are shown in Table I. For TM_{01} mode, the current distribution is in-phase across the unit cells on the MTS layer. The H-field distribution is in-phase across the entire MTS, but orthogonal to the current distribution. For TM_{12} mode, the current distribution on the 1^{st} and the 3^{rd} columns is in-phase up across the unit cells on the MTS layer, while that on the 2^{nd} column is in-phase down. The H-field distribution has two closed magnetic field loops along with the horizontal gaps on the MTS layer. For TM_{32} mode, the current distribution on the center and corner unit cells ((1^{st} (row), 1^{st} (column)), (1^{st}, 3^{rd}), (2^{nd}, 2^{nd}), (3^{rd}, 1^{st}), (3^{rd}, 3^{rd})) on the MTS layer is in-phase up, whereas that on the side unit cells ((1^{st} (row), 2^{nd} (column)), (2^{nd}, 1^{st}), (2^{nd}, 3^{rd}), (3^{rd}, 2^{nd})) is in-phase down.

Table I. The Current, E-field, and H-field Distributions of TM_{01}, TM_{12}, and TM_{32} Modes.

	TM_{01}	TM_{12}	TM_{32}
I	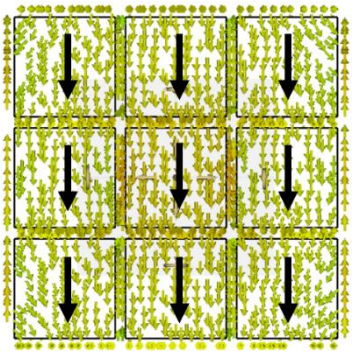	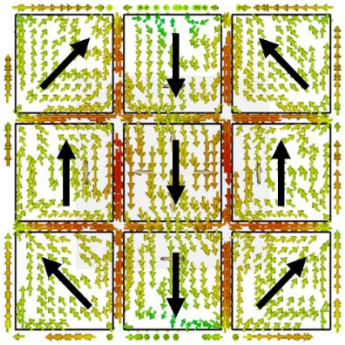	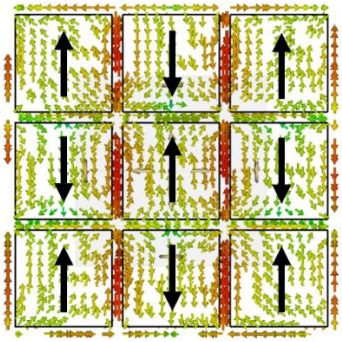
E	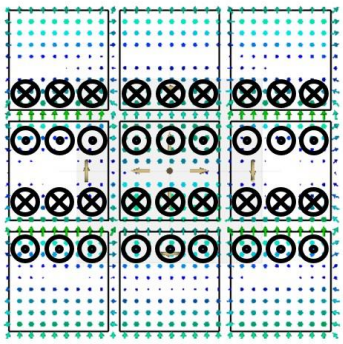	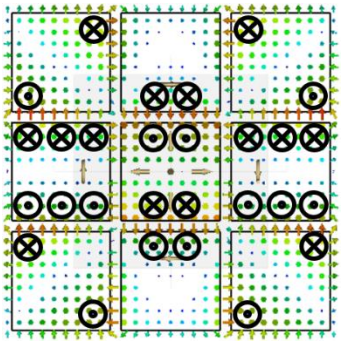	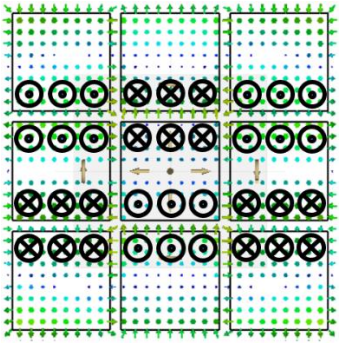
H	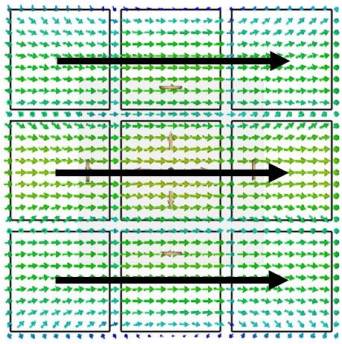	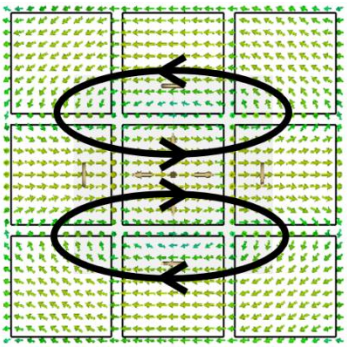	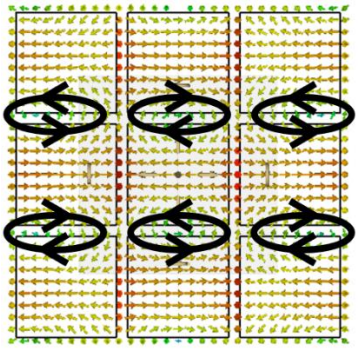

It is noted that most MTS antenna designs in this thesis are analyzed by their current distributions at each frequency. Only the modes of the first MTS antenna design in Chapter 4 are analyzed by its H-field distributions. The reason is that this is the first design in this thesis, and we want to use H-field distributions to describe these transverse magnetic (TM) modes more clearly (take the mode identification method in the waveguide as the reference).

3.2 Parametric Studies in MTS Antennas

According to the above-mentioned mode analysis, in this basic 3×3 MTS antenna, the parameters on the MTS layer are the main factors affecting the resonant frequencies while those on the feeding layer are the minor factors. There are two determining factors on the MTS layer, including the unit size and the gap width. In contrast, the feeding layer has two related factors: the aperture length and the aperture width.

The MTS antenna with CMA has been simulated to verify which parameters are the major factors and which are the minor factors. The MTS antenna is simulated by the method of the moments-based CMA tool in CST MWS software. Only the MTS layer is considered and meshed, as shown in Fig. 3. 3(a). The currents are solved on the MTS layer. The substrate material is Rogers RO4003c, which is set as lossless. As can be seen in Fig. 3. 3(b) and (c), the four-sided and top boundaries are set as open while the bottom boundary is set as PEC.

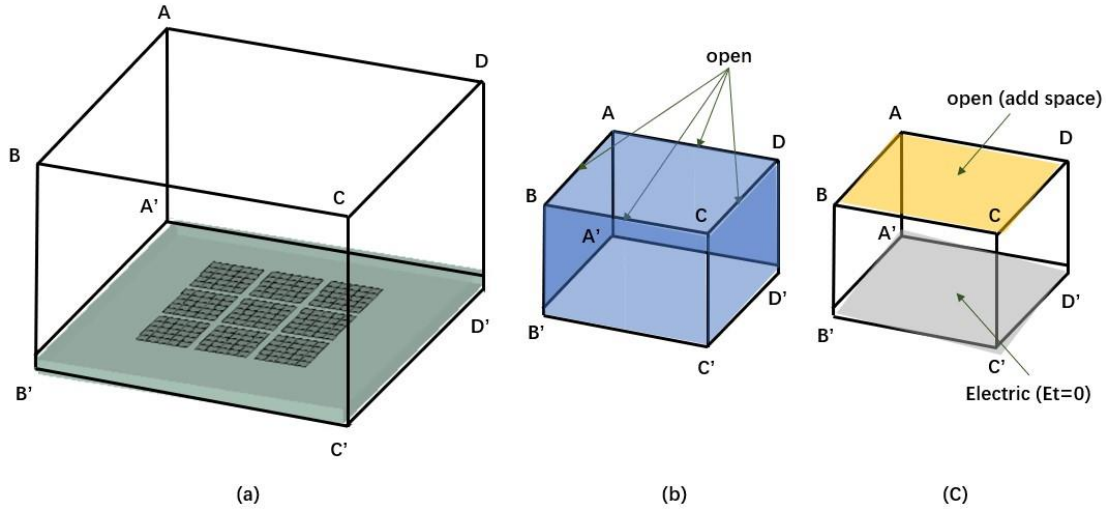

Figure 3.3. (a) Geometrical modeling. Boundary setup of (b) four sides and (c) top and bottom sides.

The modal significances of the first 20 modes from 4 to 10 GHz are calculated at 5.8 GHz. Among these modes, three TM modes mentioned in the Section 3. 1 can be found, which are TM_{01}, TM_{12}, and TM_{32} modes. The modal current distributions of these three TM modes are shown in Fig. 3. 4. The feeding layer is appropriately designed to excite three TM modes. Therefore, the parameters on the MTS layer determine three TM modes while those on the feeding layer affect three modes.

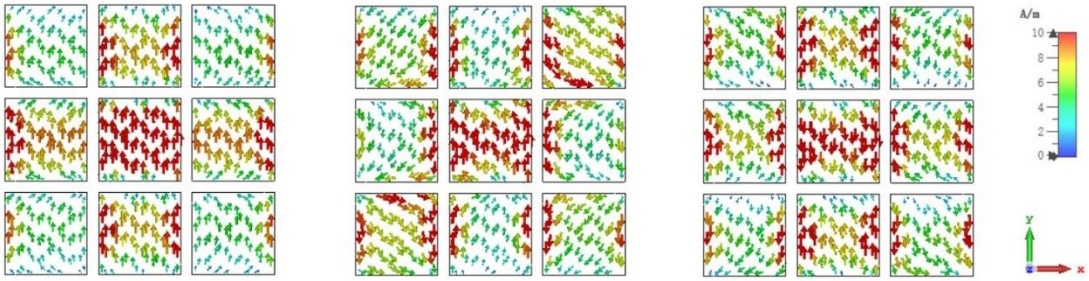

Figure 3.4. Modal current distributions of three TM modes in 3×3 MTS antenna.

3.2.1 Effect of Main Factors on MTS Performance

A. Unit Size

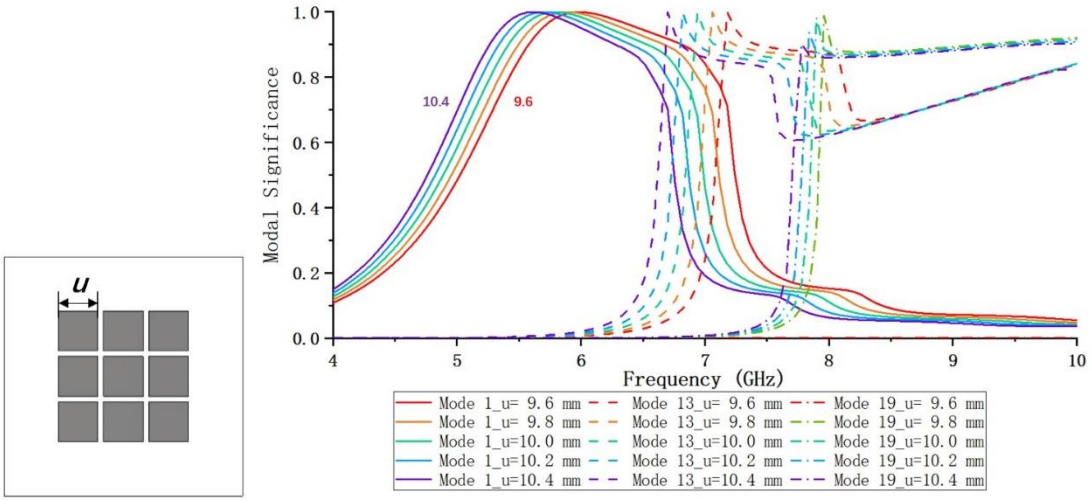

(a)

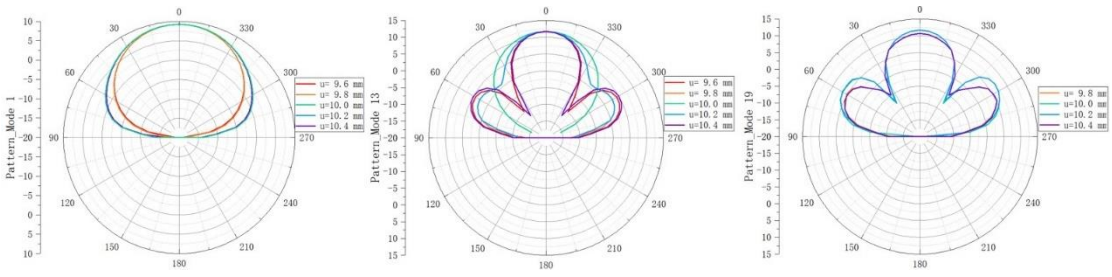

(b)

Figure 3.5. (a) Variation of modal significance against different unit sizes (*u*). (b) Variation of radiation pattern against different unit sizes.

Unit size has a major effect on determining the resonant frequency and the radiation pattern of three TM modes. Fig. 3. 5 shows the effect of unit size on the modal significance and radiation

patterns of three TM modes. As can be seen in Fig. 3. 5(a), as unit size *u* increases, the resonant frequencies of three TM modes shift downward due to the increasing electrical size of the MTS. As shown in Fig. 3. 5(b), when the unit size grows, the beamwidth of TM_{01} extends whereas the gain of TM_{01} mode decreases (the gain value is shown in Table II). When the unit size increases, the beamwidths of TM_{12} and TM_{32} modes increase initially and then decrease while the gains of TM_{12} and TM_{32} modes show a trend from decline to rise.

B. Gap Width

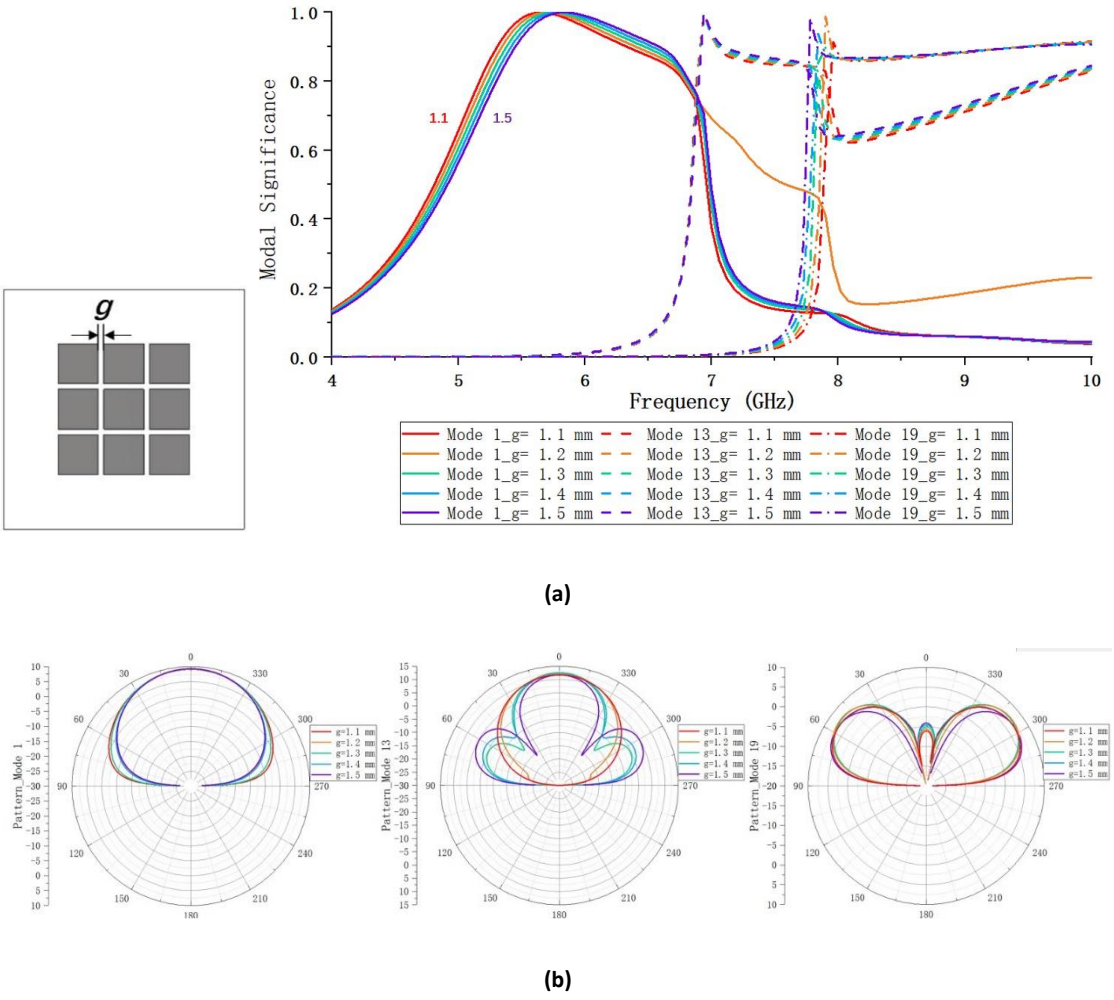

Figure 3.6. (a) Variation of modal significance against different gap widths (*g*). (b) Variation of radiation pattern against different gap widths.

Another important parameter that determines the resonant frequency and the radiation pattern of three TM modes is gap width. It can be observed from Fig. 3. 6(a) that when the gap width reduces, the resonant frequency of TM_{01} mode lowers, the resonant frequency of TM_{12} mode keeps almost the same, and the resonant frequency of TM_{32} mode increases. The gap width can

be equivalent to the capacitance. When the gap width reduces, the equivalent capacitance value increases. The fundamental TM_{x1} mode is related to half-wavelength which is greatly affected by the gap width while the higher TM_{x2} mode is related to full wavelength which has no effect on the gap width. When the gap width decreases, the beamwidths of the three TM modes increase, and the gains of the three TM modes decrease, which is shown in Table II.

C. Number of Unit Cells

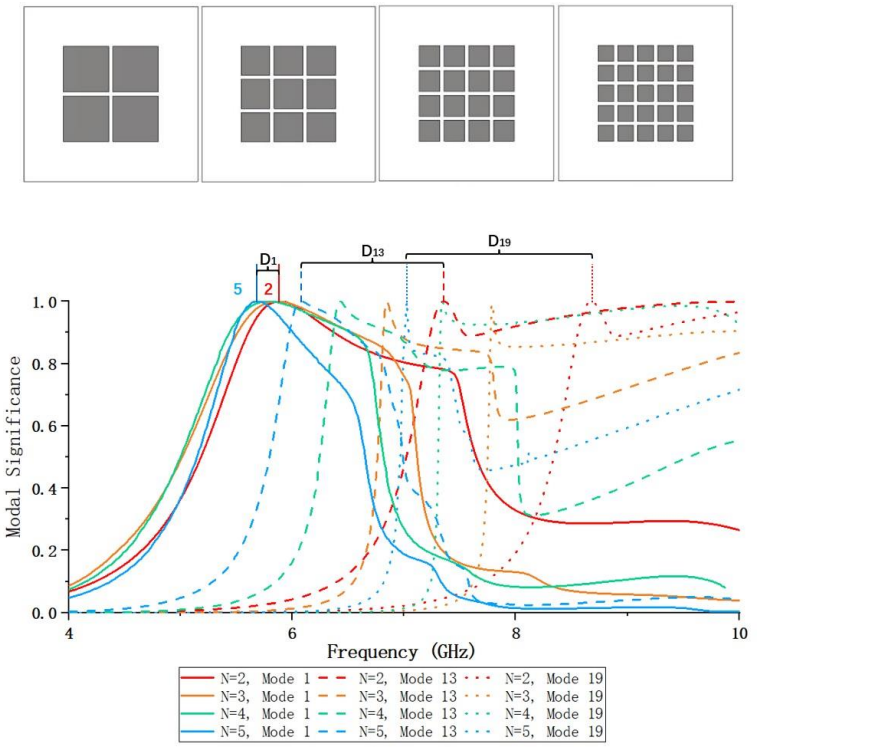

(a)

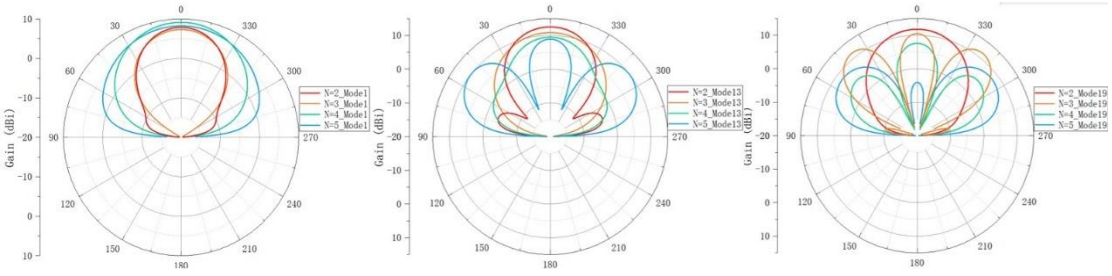

(b)

Figure 3.7. (a) Variation of modal significance against the different unit number (*n*). (b) Variation of radiation pattern against the different unit numbers.

The number of unit cells is also taken into account when designing an MTS antenna. Due to the increasing electrical size of the MTS, the resonance frequency of three TM modes shifts

downward as the number of unit cells grows, as illustrated in Fig. 3. 7(a). As observed in Fig. 3. 7(b) and Table II, when the number of unit cells grows, the beamwidth of TM_{01} mode increases, and the gain of TM_{01} mode also increases. When the number of the unit cells increases, the beamwidths of TM_{12} and TM_{32} modes decrease and the gains of TM_{12} and TM_{32} modes decrease as well.

3.2.2 Effect of Minor Factors on MTS Performance

Different from the major factors, two minor factors are on the ground plane. The MTS antenna with aperture-coupled feeding structure and feeding port is studied using CST MWS to test the influence of the feeding layer on three TM modes. Six directions are all set as open boundaries.

A. Aperture Length

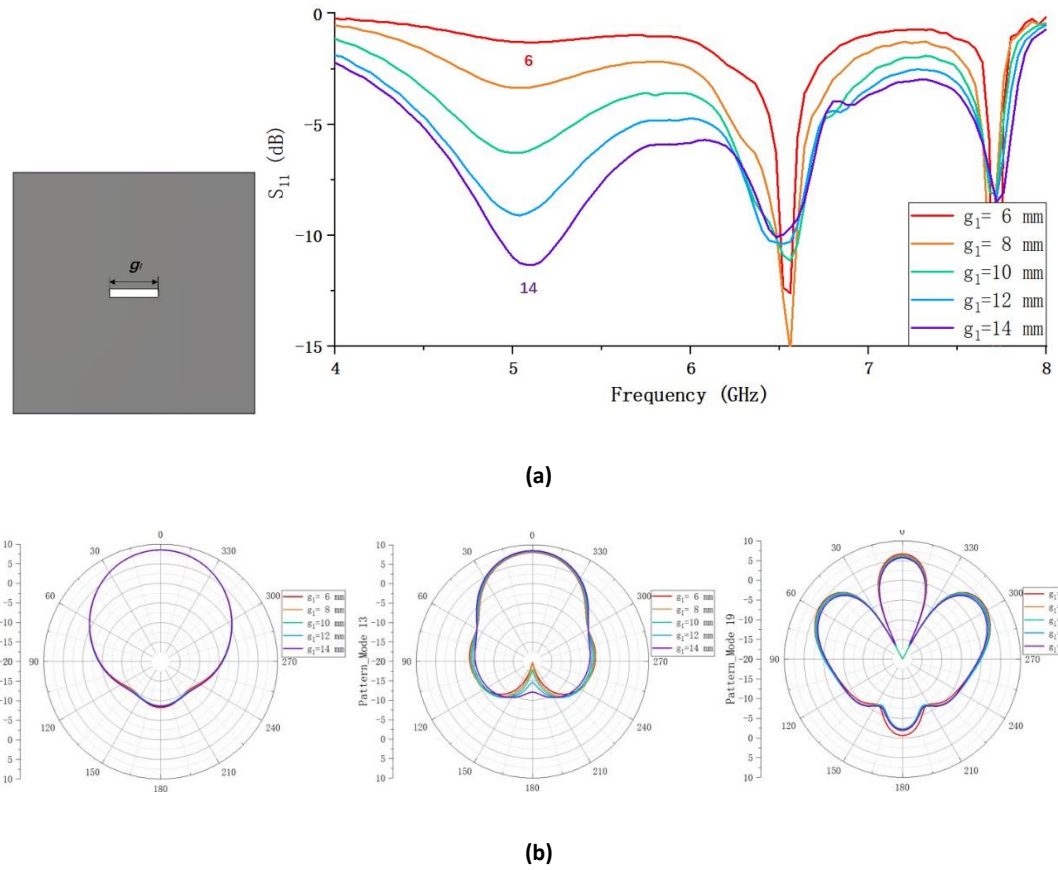

Figure 3.8. (a) Variation of modal significance against different aperture lengths (g_l). (b) Variation of radiation pattern against different aperture lengths.

B. Aperture Width

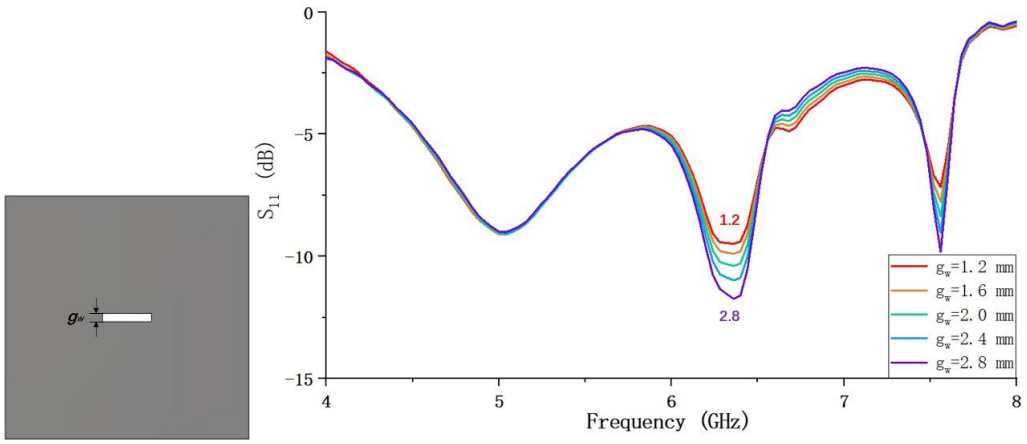

(a)

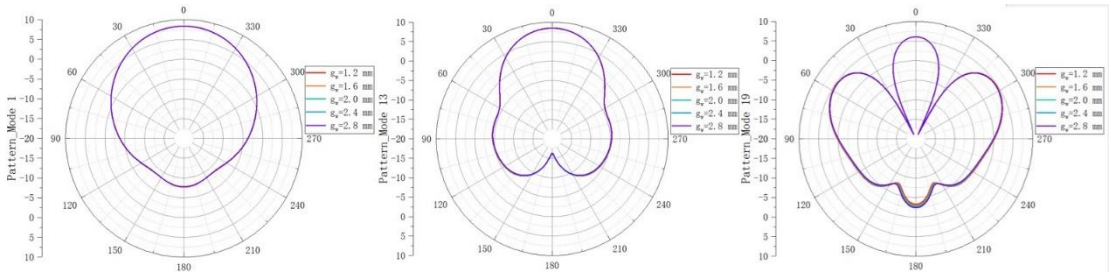

(b)

Figure 3.9. (a) Variation of modal significance against different aperture widths (g_w). (b) Variation of radiation pattern against different aperture widths.

The minor factors are the aperture length and aperture width, which are mainly used to excite three modes and adjust the impedance matching. The aperture length does not affect the resonant frequency of TM modes but the resonant frequency of aperture mode. However, the aperture mode is not considered here. As observed in Fig. 3. 8 and Table II, when the aperture length increases, the resonant frequencies, the beamwidths, and gains of three TM modes nearly have no change. A similar phenomenon can be seen in Fig. 3. 9 and Table II, when the aperture width changes, three performances of three modes almost remain stable.

Table II. The Current, E-field, and H-field Distributions of TM_{01}, TM_{12}, and TM_{32} Modes.

Gain (dBi)				
Parameter (mm)		Mode 1 (TM_{01})	Mode 13 (TM_{12})	Mode 19 (TM_{32})
Unit Size (u)	9.6	9.75	10.42	9.65
	9.8	9.75	10.2	9.6
	10.0	9.75	9.9	8.26
	10.2	9.74	11.9	8.30
	10.4	9.74	12.2	9.2
Gap Width (g)	1.1	9.8	11.7	8.27
	1.2	9.77	11.9	8.01
	1.3	9.69	11.9	7.85
	1.4	9.63	12.1	7.6
	1.5	9.56	12.2	7.37
Unit Number (n)	2	7.97	11.3	11.44
	3	7.03	10.7	9.5
	4	9.15	9.49	10
	5	11.9	8.92	7.17
Aperture Length (g_l)	6	≅9.02	≅8.6	≅7.5
	8			
	10			
	12			
	14			
Aperture Width (g_w)	1.2	≅8.84	≅8.95	≅7.1
	1.6			
	2.0			
	2.4			
	2.8			

3.3 Summary

This chapter covers the mode analysis from MTS antenna structure and identify the modes from E-/H-field distributions. It also includes the parametric studies between different parameters and the MTS performance (such as S_{11}, beamwidth and gain). It also verifies that the parameters on the MTS layer are main factors (determining three excited TM modes) while the parameters on the feeding layer are minor factors (no affecting on three TM modes).

3.4 References

[1] CST software, from http://www.cst-korea.co.kr/Application/MIMO-Antenna-Simulation-CSTMWS.pdf.

[2] C. A. Balanis, "Antenna Theory: Analysis and design", 3rd ed., John Wiley and Sons, New Jersey, 2005, pp. 1117.

[3] Antenna theory, from https://www.antenna-theory.com/

[4] W. Liu, Z. N. Chen, and X. Qin, "Metamaterial-Based Low-Profile Broadband Aperture-Coupled Grid-Slotted Patch Antenna," *IEEE Transactions on Antennas and Propagation*, vol. 63, no. 7, pp. 3325-3329, Jul. 2015.

Chapter 4 Design of MTS Antenna Designs with Bandwidth Improvement

The metasurface (MTS) antenna can excite several MTS modes because of the unique structure with several radiating gaps. The unit size and gap width are the main determinants of MTS modes, hence designing unit cells on the MTS with specific shape/structure can have an impact on MTS antenna performance. In this Chapter, two designs demonstrate that the MTS antenna has the possibility to achieve broad/dual- bandwidth. Unit cells with hexagonal shape and unit cells with a composite right-/left-handed (CRLH) structure are applied in these designs.

4.1 Introduction

The antenna is a critical component in the wireless communication system. It has a significant impact on the overall performance of a wireless communication system. There will be a loss if the antenna is not correctly designed and precisely fitted for its working frequency, resulting in the system failing. As a result, one of the essential techniques in wireless communications is antenna design with performance improvements such as broad bandwidth, multiband, high gain, high efficiency, or polarization diversity.

Nowadays, modern communication systems are utilizing an increasing number of frequency bands. The antennas with broadband performance appeal to engineers and researchers because they can cover more frequencies. In some applications, dual-band antenna design is more appropriate than broadband one. The dual-band dual-mode antenna is employed to switch between sleep and wake-up modes for wearable/implantable devices [8]. A lower frequency range is typically used for downlink power transmission to the wireless-powered device. In comparison, a higher frequency band is generally used for uplink information transmission to the satellite [9].

Traditional antennas such as microstrip patch antennas have several advantages, such as low profile and ease of fabrication, but their use is limited due to their inherent narrow bandwidth. Various approaches such as aperture coupling [1], usage of coupled parasites [2], stacking [3], [4], E-shaped patch [5], and feed modifications [6], [7] have been explored to extend the

bandwidth of a microstrip patch antenna. Different from these methods, the MTS antenna, due to its unique multiple radiating gaps, can excite more modes, resulting in broadening the bandwidth.

In this Chapter, two MTS antennas are designed for wireless communication system. One is the broadband MTS antenna with a novel hexagonal loop-shaped unit cell structure. The other is a dual-band nonuniform MTS-based antenna with hexagonal radiating elements and parasitic elements. Dual-band performance is obtained by CRLH structure.

4.2 Bandwidth of Hexagonal Structure

The antenna in this Chapter is designed and analyzed in computer simulation technology (CST) microwave studio (MWS) software. Different parameters like reflection coefficient (S_{11}), gain, radiation patterns, and impedance matching are simulated using the time domain solver in CST. Simulations are carried out from 4 to 9 GHz, and the boundary settings of six directions are all open.

In addition, the results like modal significances and characteristic current distributions are obtained using the method of the moments-based CMA tool in CST MWS. The boundary of the ground plane is set as electric while the rest five boundaries are all set as open, which is detailed described in Chapter 3.

4.2.1 Radiating Bandwidth Comparison between Unit Cells with Different Shapes

In MTS antennas, the choice of the element structure and the layout of the radiating elements determine the resonant frequencies and radiation bandwidth. The antenna performance can be improved by optimizing the shape of the radiating elements, as well as the gaps between neighbouring elements. In this chapter, the hexagon structure is chosen to design the proposed antenna to achieve a wider bandwidth compared with other antennas built based on traditional unit cells such as square or circular ones.

The reason that the hexagonal structure is a suitable option is mainly because unit cells incorporating tapered or rounded edges lead to the surface current flowing through smooth paths. The smooth transition on the edge of the radiating elements will cause a smaller variation

in the input impedance, defined as the impedance seen from the input port of the whole MTS antenna with the presence of the feeding structure. Such a difference will lead to broad bandwidth performance and impedance matching improvement [19]. Compared with conventionally designed square radiating elements [14]-[18], a smoother transition brought by hexagonal unit cells will potentially enable the antenna to achieve wider bandwidth performance.

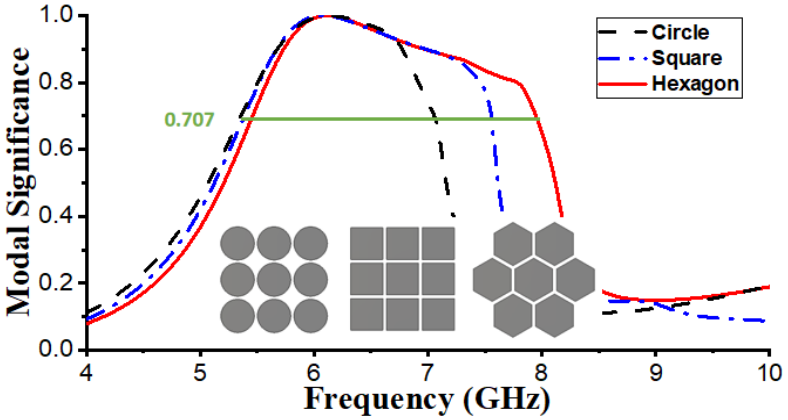

Figure 4.1. The modal significance comparison between square, hexagonal and circular elements.

4.2.2 Gap Effect on Unit Cells with Different Shapes

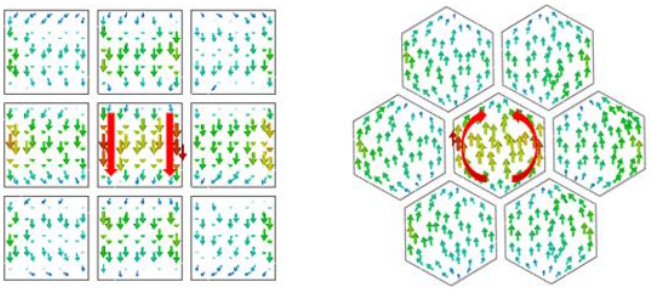

(a) **(b)**

Figure 4.2. The characteristic current distributions on (a) square unit cells and (b) hexagonal unit cells.

The characteristic mode analysis technique is employed to compare the bandwidth of hexagonal and square unit cells. With the aid of the characteristic mode analysis, the radiating bandwidth of a structure can be predicted without considering the feed. In modal significance, the radiating bandwidth of a mode is defined as the range of frequencies within which the

power radiated by the mode is no less than one-half the power (equivalent to $MS = \frac{1}{1+j\lambda_n} = \frac{1}{\sqrt{2}} = 0.707$, where λ_n is the eigenvalue of the generalized impedance matrix) [20]. To make a fair comparison, the tessellation of square unit cells and hexagonal unit cells with almost identical metallic areas are analyzed, as shown in Fig. 4. 1. By evaluating the modal significance at the fundamental frequency, the hexagonal structure can achieve a wider radiating bandwidth (41%) than the square one (35%).

Furthermore, as can be seen in Fig. 4. 2, the characteristic current (depicted using red arrows) at the edge of the hexagonal unit cell flows with a much smoother transition, compared with that of the square unit cell in which the current is flowing in straight lines. This is consistent with the explanations in the last paragraph. Such an appealing property brought by hexagonal unit cell will lead to a wider bandwidth.

However, not all radiating structures with a smooth transition on the edge are suitable choices, particularly when considering the influence on the bandwidth brought by gaps between neighbouring unit cells. One representative example is the circular patch which has the smoothest structural transition. When the circular unit cells are used, gaps between composing elements cannot be kept constant. As demonstrated in [19], the bandwidth can be affected by changing impedance values. When considering potential influence between neighbouring unit cells, the transition of gaps between neighbouring circular unit cells is not constant, compared with that of hexagonal ones or square ones.

To evaluate the gap effect on unit cells with different structures, the equivalent circuit has been used to do the comparison. The equivalent circuit provides a simple and quick way to understand the behaviour of unit cells. For the period unit cell, the equivalent inductive (L) and capacitive (C) construct the circuit. Both L and C values of the equivalent circuit are commonly calculated using (1) and (2), where d, p, s, and g are the unit size, period size, loop width, and gap width. θ is the incidence angle, which is 0 here.

$$\frac{X_L}{Z_0} = \omega \mathrm{L} = \frac{d}{p} \cos\theta \, F(p, 2s, \lambda, \theta) \tag{4. 1}$$

$$\frac{B_C}{Y_0} = \omega \mathrm{C} = 4\frac{d}{p} \sec\theta \, F(p, g, \lambda, \theta) \varepsilon_{eff} \tag{4. 2}$$

where

$$F(p,w,\lambda,\theta) = \frac{\mathrm{p}}{\lambda}\left[\ln\left(\csc\frac{\pi w}{2p}\right) + G(p,w,\lambda,\theta)\right] \quad (4.3)$$

$$G(p,w,\lambda,\theta) = \frac{1}{2} \times \frac{(1-\beta^2)^2\left[\left(1-\frac{\beta^2}{4}\right)(A_+ + A_-) + 4\beta^2 A_+ A_-\right]}{\left(1-\frac{\beta^2}{4}\right) + \beta^2\left(1+\frac{\beta^2}{2}-\frac{\beta^4}{8}\right)(A_+ + A_-) + 2\beta^6 A_+ A_-} \quad (4.4)$$

with

$$A_\pm = \frac{1}{\sqrt{\left[1 \pm \frac{2p\sin\theta}{\lambda} - \left(\frac{p\cos\theta}{\lambda}\right)^2\right]}} - 1 \quad (4.5)$$

$$\beta = \sin\left(\frac{\pi w}{2p}\right) \quad (4.6)$$

$$\varepsilon_{eff} = 0.5(\varepsilon_r + 1) \quad (4.7)$$

According to the equations from (1) to (7) [21]-[22], the inductance value of unit cell with square solid structure (L_{sq}) is 1.89 (nH) while the capacitance value of that (C_{sq}) is 2.43 (pF). The inductance value of unit cell with circle solid structure (L_{cir}) is 2.38 (nH) while the capacitance value of that (C_{cir}) is 1.78 (pF). The inductance value of unit cell with hexagon solid structure (L_{hex}) is 1.7 (nH) while the capacitance value of that (C_{hex}) is 2.73 (pF). The gap effect on different structures, which is equivalent from capacitance value, can be concluded as: $C_{hex} > C_{sq} > C_{cir}$. The equivalent capacitance value of hexagon unit cell is largest among these three structures.

In short, the hexagonal structure has a wider bandwidth than the other two. Therefore, it is chosen as the radiating element.

4.3 Design I: Broadband MTS Antenna Design with Hexagonal Loop Elements

4.3.1 Antenna Design

1) Mode analysis in a basic MTS antenna with hexagonal radiating unit cells

To achieve broadband performance as analyzed above with the simplest and most compact settings, a basic MTS antenna using hexagonal unit cells is designed. In this model, the basic MTS antenna consists of the MTS layer and the feeding layer. The geometry and detailed dimensions of the MTS layer and the feeding layer are shown in Fig. 4. 3(a). These two layers

are coupled through an aperture. A Rogers RO4003c substrate is used to connect these two parts, of which the relative dielectric constant is 3.38. The heights of the first and the second layers are 3.18 mm and 0.813 mm, respectively.

Potentially, both the TE and TM modes could be excited using MTS antennas. Nevertheless, as shown in Fig. 4. 3(a), the basic antenna is fed by a microstrip line, along the y-axis and perpendicular to the z-axis. It is coupled to the MTS layer via the aperture on the ground plane. Consequently, there is no electric field vector parallel with the MTS surface generated by this feeding structure. In this sense, since the feed is underneath the center of the hexagonal units, TE modes cannot be excited. On the contrary, TM modes can be easily excited, including the fundamental and higher TM modes. The fundamental TM mode is excited since the electromagnetic wave will be coupled from the microstrip line to the center of the MTS via the center of the aperture. In more detail, it is the fundamental patch TM_{01} mode since the feed is parallel with the y-axis. Fig. 4. 3(b) verifies this since the direction of the magnetic field on the MTS is along the x-axis.

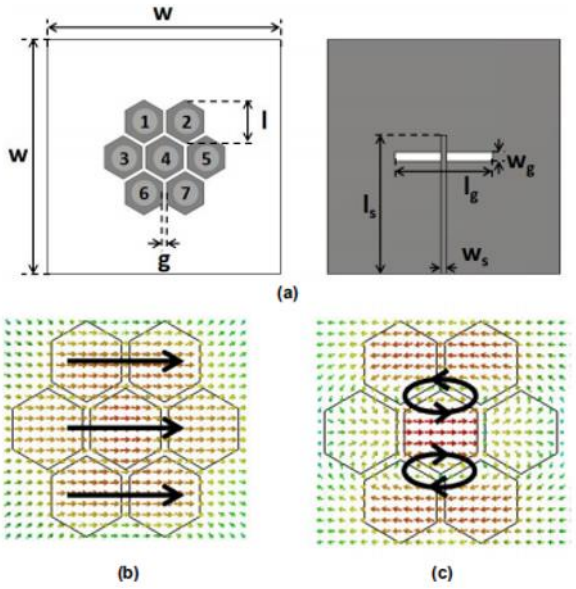

Figure 4.3. (a) Geometry of the basic MTS antenna using hexagonal radiating elements: MTS layer and feed layer (Dimensions: W= 60 mm, l= 10.5 mm, g= 1 mm, l_g= 25 mm, w_g= 2.4 mm, l_s= 35.5 mm, w_s= 1.55 mm). The magnetic field distributions at (b) the 1st frequency and (c) the 2nd frequency on the xoy plane.

Apart from the fundamental patch TM_{01} mode, it is also possible that higher TM_{xy} modes can be excited. The values of x and y are decided by different factors, which will be discussed as follows.

The value of *x* should be odd. As can be seen in Fig. 4. 3(a), for hexagonal tessellation, the unit cells have to be placed in a staggered manner. Otherwise, non-tessellation or overlapping will occur if they are aligned in a conventional way as the case for square unit cells. Based on this staggered geometry, units 1 and 2 are symmetric along the y-axis. In the area above the feed line, e.g. on unit 4 or on the gap between unit 1 and 2, the magnetic field must be parallel to the MTS surface along the x-axis. Therefore, the directions of the magnetic field on units 1 and 2 must be in the same direction. The same applies to units 6 and 7 due to symmetry. Since the magnetic field must form complete loops, the number of loops along the x-axis direction must be an odd number. The directions of the magnetic field on unit 1 and unit 2 cannot be the same if the number of loops was an even number.

Differently, the value of *y* is determined by the number of horizontal radiating gaps that are parallel to the aperture on the ground plane. Vertical gaps are not radiating because they are orthogonal to the aperture. For this reason, *y* is equal to 2 for lower modes since there are only two horizontal radiating gaps in this basic MTS antenna.

To verify the prediction, the magnetic field distributions at the 2nd resonant frequency are illustrated in Fig. 4. 3(c). In each horizontal radiating gap, there will be one single closed magnetic field loop. Therefore, the MTS antenna operates at the TM_{12} mode. Higher modes are possible, but it will be beyond the frequency of interest.

2) Mode analysis of the MTS antenna with hexagonal loop elements

To achieve a broader operating bandwidth, two changes are made to the fundamental antenna. Firstly, 12 extra hexagonal loop unit cells are placed outside of the basic MTS antenna, as shown in Fig. 4. 4. Secondly, hexagonal loop unit cells are used instead of hexagonal patch ones. This is because using loops can lower the resonant frequency of the MTS antenna [16]. The feeding structure is kept the same as the basic MTS antenna. In the proposed MTS antenna, there are in total 19-unit cells placed to form three concentric rings, namely the inner, the middle, and the outer ring with one, six, and 12-unit cells, respectively. Let UC-i denote the unit cell indexed as *i* as shown in Fig. 4. 4. The notation of the unit cell set can be defined as {UC-i, i∈I}, where the set of I contains all the possible indices. Based on this, for the inner ring, it is UC-10. For the middle ring, it is {UC-i, i∈{5, 6, 9, 11, 14, 15}}. For the outer ring, it is {UC-i, i∈{1, 2, 3, 4, 7, 8, 12, 13, 16, 17, 18, 19}}. These three rings are seen in Fig. 4. 4.

The unit cells in the inner and middle rings are of the same size. The size of unit cells in the outer ring is slightly smaller than those in the inner and middle rings, to be discussed later.

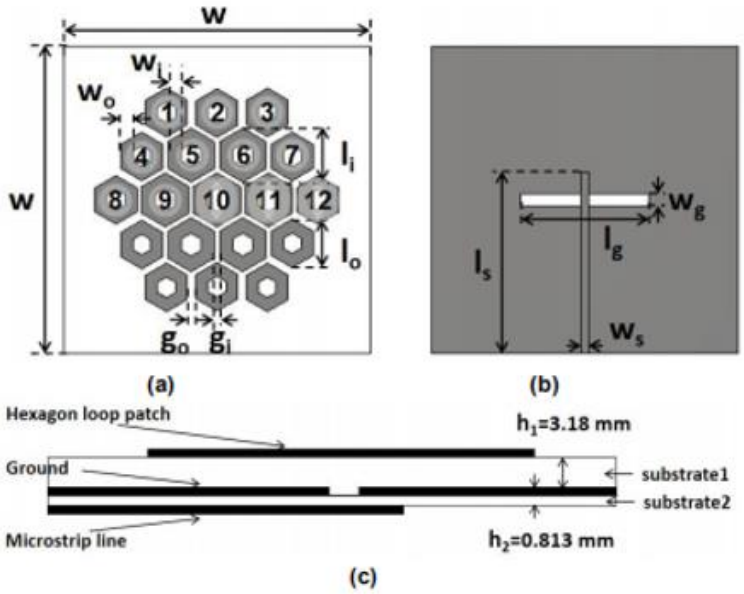

Figure 4.4. Geometry of the proposed MTS antenna using hexagonal loop unit cells. (a) Top view. (b) Bottom view. (c) Side view. (W= 60 mm, l_i= 10.5 mm, l_o= 9.5 mm, w_i= 2.6 mm, w_o= 2.3 mm, g_i= 1 mm, g_o= 1.7 mm, l_g= 25 mm, w_g= 2.4 mm, l_s= 35.5 mm, w_s= 1.55 mm).

The same mode analysis method will be used to see only TM_{xy} modes can be excited. Specifically, the fundamental TM_{01} mode can still be excited since the microstrip line of the aperture coupled feeding part is along the y-axis. If *x* is not 0, it can only be an odd positive integer, as discussed in previous section.

As can be seen in Fig. 4. 4, there are in total four horizontal radiating gaps in the proposed MTS antenna. Therefore, *y*=2 or 4. Except for TM_{01}, two kinds of TM modes (TM_{x2} or TM_{x4}) can be possibly excited. The resonant frequencies of modes with x>1 are too high for the operational band of interest. The resonant frequencies of modes with y$\geqslant$4 are also very high. These high modes are not considered in this design. Therefore, only the TM_{12} mode can be excited.

However, the TM_{12} mode can be excited in different ways, i.e., at different radiating positions corresponding to different resonant frequencies. To better demonstrate this, those involved unit cells are divided into five rows. As shown in Fig. 4. 4, the 1st row to the 5th row contain unit cells {UC-i, 1$\leqslant$i$\leqslant$3}, {UC-i, 4$\leqslant$i$\leqslant$7}, {UC-i, 8$\leqslant$i$\leqslant$12}, {UC-i, 13$\leqslant$i$\leqslant$16}, and {UC-i,

$17 \leqslant i \leqslant 19\}$, respectively. Since the unit cells are symmetric, the electromagnetic field distribution on elements from the 1st to the 3rd rows will be symmetric to that from the 3rd to the 5th row. In the top half {UC-i, $1 \leqslant i \leqslant 12\}$ in Fig. 4. 4, closed magnetic field loops can be excited in two positions. One loop can be excited around the gaps between the 1st and the 2nd row. Another loop can be excited around the gaps between the 2nd and the 3rd row. In each case, the loop can involve different units.

3) Study on the excited modes

To verify the prediction above, the operation of the antenna is evaluated by simulation. Five resonant frequencies can be observed in the simulation. The magnetic field distributions on the xoy planes are shown in Fig. 4. 5. The magnetic field along the MTS layer is marked in black.

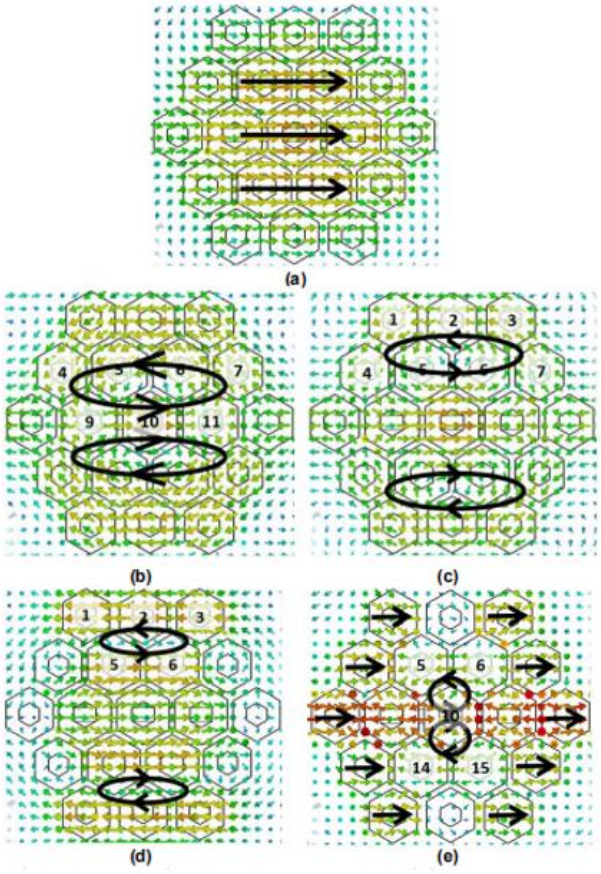

Figure 4.5. The magnetic field distributions on the xoy plane at (a) the 1st frequency, (b) the 2nd frequency, (c) the 3rd frequency, (d) the 4th frequency and (e) the 5th frequency.

For the fundamental mode, the magnetic field distribution is similar to the patch antenna operating in the TM_{01} mode [10]. At the 2nd resonant frequency, in terms of the magnetic field, two closed magnetic loops can be observed on the gaps between unit cells {UC-i, $i \in \{4, 5, 6,$

7, 9, 10, 11}} and {UC-i, i∈{9, 10, 11, 13, 14, 15, 16}}. The MTS antenna operates in an anti-phase TM_{12} mode.

The MTS can operate in the TM_{12} mode in different ways. Another two resonant frequencies can be generated. As can be seen in Fig. 4. 5(c) and (d) at the 3rd and 4th frequencies, respectively, the MTS operates in the anti-phase TM_{12} mode as well. However, these two modes differ from each other since the corresponding magnetic loops are in different areas. At the 3rd resonant frequency, two closed magnetic loops are mainly generated by unit cells {UC-i, 1⩽i⩽7}, and its symmetric area on the bottom half of the MTS surface. While at the 4th resonant frequency, the two loops are in the region of unit cells {UC-i, i∈{1, 2, 3, 5, 6}} and its symmetric region. Since the effective area shaping the magnetic loop at the 3rd frequency is larger than that at the 4th one, the 3rd frequency is lower than the 4th frequency.

Due to that a similar number of unit cells are involved in the generation, the 2nd and 3rd frequencies would have been very close to each other. To separate the two frequencies, the units in the outer ring are slightly smaller than the units in the middle and inner rings. The 3rd frequency will be shifted higher, to improve the in-band performance of the antenna.

At the 5th resonant frequency, in Fig. 4. 5(e), two closed magnetic loops are present around unit cells {UC-i, i∈{5, 6, 10}} and its symmetric region {UC-i, i∈{10, 14, 15}}. The magnetic field distribution pattern suggests that the MTS still mainly operates at the TM_{12} mode. However, since the operating frequency is relatively high, the surrounding unit cells {UC-i, i ∈{1, 3, 4, 7, 8, 12, 13, 16, 17, 19}} also make the contribution to the radiation. As a result, this radiation is influenced both by the anti-phase TM_{12} mode and parasitic element effect.

4.3.2 Parametric Studies

A. Unit Size

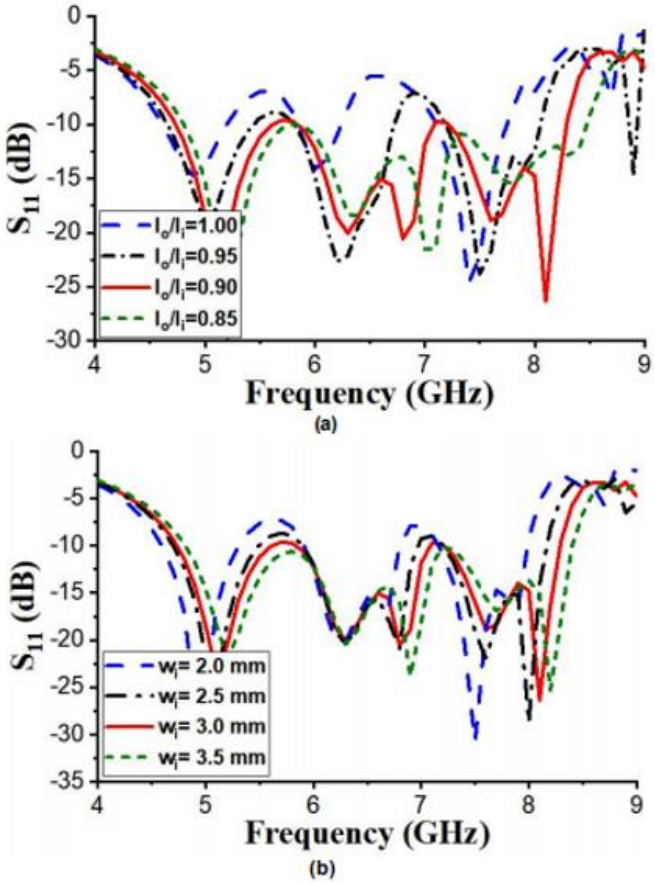

Figure 4.6. The S-parameter comparison of the antenna (a) with the same size of unit cells and the antenna with different sizes of unit cells on the MTS layer and (b) with different widths of unit cells.

It is interesting to investigate the effect of altering the dimensions of unit cells on different rings. It is noticed that each magnetic field loop is mainly generated by seven-unit cells at the 2nd and the 3rd frequency, as shown in Fig. 4. 5(b) and (c) respectively. The loops of the 2nd frequency are generated by unit cells on the middle and inner rings, while the loops of the 3rd frequency are on the middle and outer. Thus, a simple comparison is conducted by applying two different unit cell dimension settings: one is when all the unit cells are of the same size and the other is when the size of unit cells on the outer ring is different from the middle and inner rings. Such a variation will affect the anti-phase TM_{12} modes at the 2nd and the 3rd frequencies differently. The comparison result is shown in Fig. 4. 6. It can be clearly seen that when unit cells are of the same size, the 2nd and the 3rd frequencies are very close to each other. When the ratio of the size of unit cells on the outer ring to that of others decreases, the difference between the 2nd frequency and 3rd frequency will increase. By changing the ratio of l_o/l_i from 1 to 0.85, the difference of the two resonant frequencies is increased from 0 to 0.65 GHz. Therefore, the

bandwidth can be increased, or the in-band performance can be improved by tuning the size of unit cells on the outer ring.

A further study is carried out to evaluate the effect of the width of the hexagonal loop. It has been studied in [16] that changing the width of a square loop will alter the resonant frequency of the loop. When the loop width w_i is decreased the resonant frequencies of all modes (the 1st frequency to the 5th frequency) will drop accordingly.

B. Gap Width

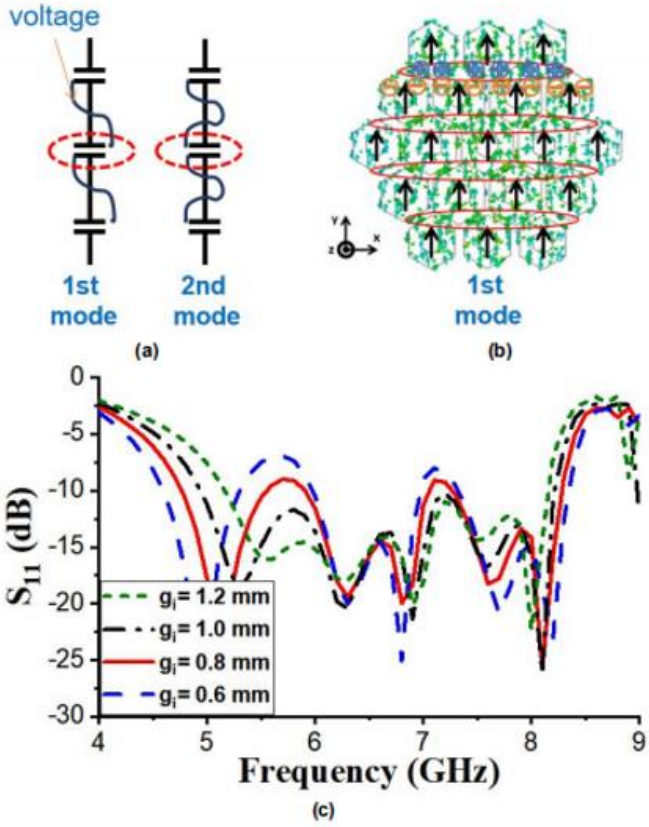

Figure 4.7. (a) The voltage difference, (b) the current distributions on the MTS layer at the 1st resonant frequency, and (c) the S-parameter comparison of the antenna with different gap widths between unit cells.

When the gap width between each unit cell is decreased, the 1st frequency will decrease dramatically, while other frequencies remain almost stable. This is because the electric field distribution for the fundamental mode leads to the significant voltage difference between adjacent unit cells [24]. The capacitance between unit cells significantly pulls the resonant frequency downward. In contrast to the fundamental mode, the resulted voltage differences are

much mixed in other modes. It leads to insignificant variations on other resonant frequencies, as shown in Fig. 4. 7(a).

At the fundamental frequency, due to the electric field distribution pattern at the TM_{01} mode, the corresponding current distributions on all units are polarized on the y-direction and in phase across the entire MTS layer. It will induce positive charges to accumulate on the bottom part of each row of unit cells and negative ones on the top part, as shown Fig. 4. 7(b).

As investigated in [24], due to the voltage difference between gaps at the fundamental frequency, increasing the capacitance between adjacent unit cells will significantly lower the resonant frequency. When considering the gap effect, hexagonal loop elements will form far greater equivalent capacitance compared with other types of elements, e.g., square ones [23].

Further verification of the relationship between the gap width and the frequency of the fundamental mode is shown in Fig 4. 7(c). When the gap width is decreased from 1.2 mm to 0.6 mm, the fundamental frequency was lowered by 16.7%, from 5.6 GHz to 4.8 GHz. Differently, because the electric field distributions are not as uniform in other modes, the gap width has much less effect on other resonant frequencies, as can be seen in Fig. 4. 7(c).

In summary, decreasing the gap will significantly lower down the 1st frequency, while the resonant frequencies of other modes will be kept relatively constant. Taking this effect into consideration, the bandwidth of the antenna can be broadened by optimizing the gap width.

4.3.3 Experimental Results

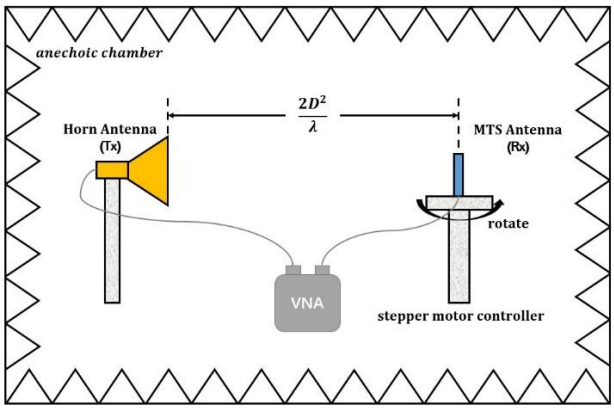

Figure 4.8. Experiment setup.

The experimental setup is shown in Fig. 4. 8. The horn antenna works as the transmitting antenna while the MTS antenna serves as the receiving antenna. The transmitting antenna and

the receiving antenna are set in the line of sight aligned to each other. The distance between them is kept as $\frac{2D^2}{\lambda}$ (guarantee far-field environment), where the maximum overall dimension of the antenna is *D*, and λ is the operating wavelength. Two cables on Port 1 and Port 2 of the vector network analyzer (VNA) are connected to the transmitting and receiving antennas, respectively. The receiving antenna is fixed to the stand whose rotation can be controlled by the stepper motor controller.

VNA can directly read the S_{11} and bandwidth of the receiving antenna. For the radiation patterns measurement, rotate the receiving antenna stand from 0 to 360° on its axis in steps of 30° and record the S_{21} reading from VNA. After that, repeat the measurement for radiation pattern in another plane (E-plane) by rotating both transmitting and receiving antennas by 90°.

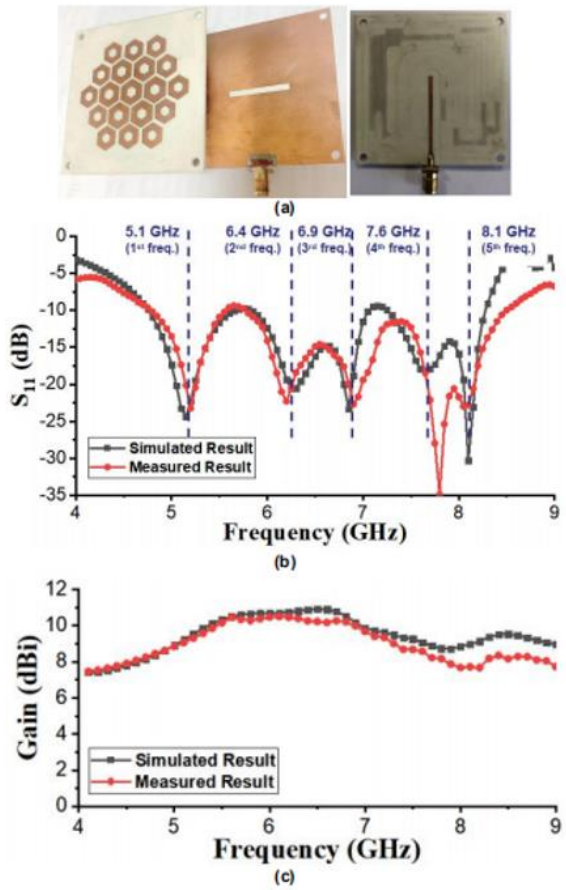

Figure 4.9. (a) Photographs of the fabricated antenna. Simulated and measured (b) S parameters and (c) gain of the proposed antenna.

To validate the proposed design method, an MTS antenna using hexagonal loop unit cells was prototyped and measured, shown in Fig. 4. 9(a). Dimensions of the antenna are illustrated in Fig. 4. 4.

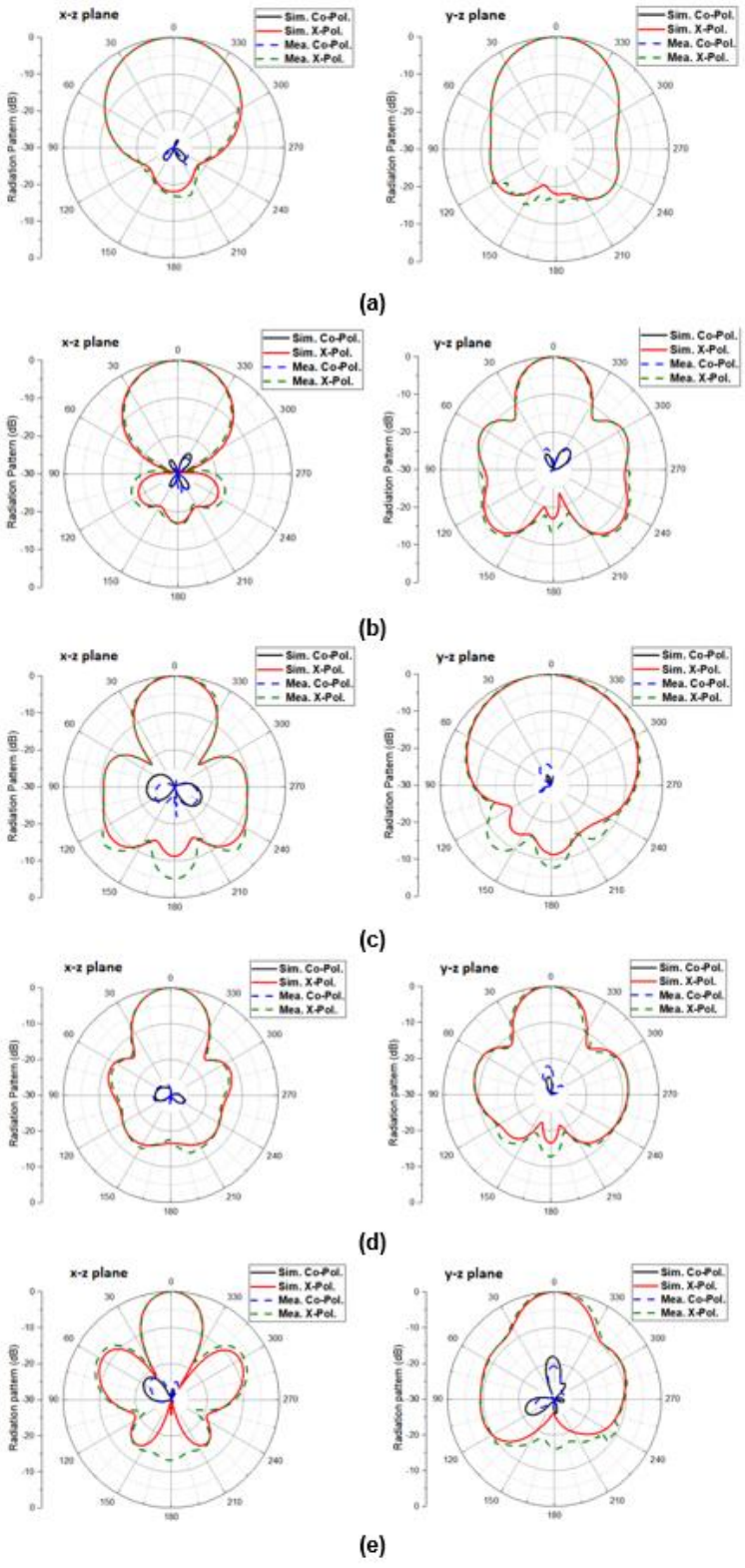

Figure 4.10. The simulated and measured radiation patterns of the proposed antenna at (a) 5.1 GHz, (b) 6.4 GHz, (c) 6.9 GHz, (d) 7.5 GHz and (e) 8.1 GHz.

Fig. 4. 9(b) presents a comparison between the simulated and measured S-parameters. The simulated bandwidth with a reflection coefficient better than -10 dB is from 4.65 to 8.3 GHz

while the measured bandwidth is from 4.7 to 8.5 GHz. The fractional bandwidth of the measurement results is 57.6%, and the resonance frequencies are 5.1, 6.4, 6.9, 7.6, and 8.1 GHz, respectively. As a comparison, the simulated fractional bandwidth is 56.3%. As shown in Fig. 4. 9(c), the simulated gain is from 7.7 to 11 dBi. By contrast, the measured gain is 7 to 11 dBi, which agrees with the simulated results very well.

The simulated and measured normalized radiation patterns at 5.1 GHz, 6.4 GHz, 6.9 GHz, 7.5 GHz, and 8.1 GHz are shown in Fig. 4. 10. They are in consistent agreement with the simulation. Due to the symmetrical feeding design, both the simulated and measured cross-polarization levels at boresight are below -30 dB in both the x-z and y-z planes across the operating frequency band. As can be seen, the proposed antenna has a very directional pattern at 5.1 GHz and 6.4 GHz. Meanwhile, the radiation patterns at 6.9 GHz and 7.5 GHz are with small side lobes. By contrast, relatively greater side lobes can be found in patterns at 8.1 GHz, which is mainly caused by the complexity of modes at higher frequencies. The discrepancy between the simulated and measured cross-polarization levels might be caused by the SMA connector used in the measurement, the fabrication errors, and the test environment variations.

Table III. Performance Comparison of Broadband Directional Metasurface Antennas.

Reference	Antenna Size (mm^3)	Centre Frequency (GHz)	10 dB Impedance Bandwidth (%)	3 dB Gain Bandwidth (%)	Peak Gain (dBi)
[11]	$1.1\lambda_0 \times 1.1\lambda_0 \times 0.09\lambda_0$	5.3 GHz	44%	45%	11.6
[12]	$2.0\lambda_0 \times 2.0\lambda_0 \times 0.16\lambda_0$	6.5 GHz	55%	N/A (50%)	11.8
[13]	$1.0\lambda_0 \times 1.0\lambda_0 \times 0.075\lambda_0$	5.6 GHz	25%	18%	10.3
[14]	$1.1\lambda_0 \times 1.1\lambda_0 \times 0.06\lambda_0$	6.0 GHz	54%	32%	10.7
[25]	$1.2\lambda_0 \times 1.2\lambda_0 \times 0.09\lambda_0$	7.0 GHz	67.3%	N/A (45%)	9.2
This work	$1.2\lambda_0 \times 1.2\lambda_0 \times 0.09\lambda_0$	6.5 GHz	56%	48%	11.2

P.S. 'N/A' means no relevant data in this reference.

The performance of the proposed antenna is compared with other broadband directional MTS antennas in Table III. Particularly, designs in [11]-[12] aim at improving the antenna performance by increasing the number of the MTS layers. The proposed hexagonal MTS antenna has achieved a similar fractional bandwidth (56%) with a single MTS layer compared with [12] (55%), and broader bandwidth than [11] (44%). Compared with other relevant designs, e.g., [13], [14], the proposed hexagonal MTS antenna has achieved a broader 3 dB gain bandwidth (48% of the proposed one compared with 18% and 32% obtained by [13] and [14] respectively).

4.4 Design II: Dual-Band MTS Antenna Design with Shorting Pins

4.4.1 Antenna Design

1) Mode analysis in a dual-band MTS antenna with shorting pins

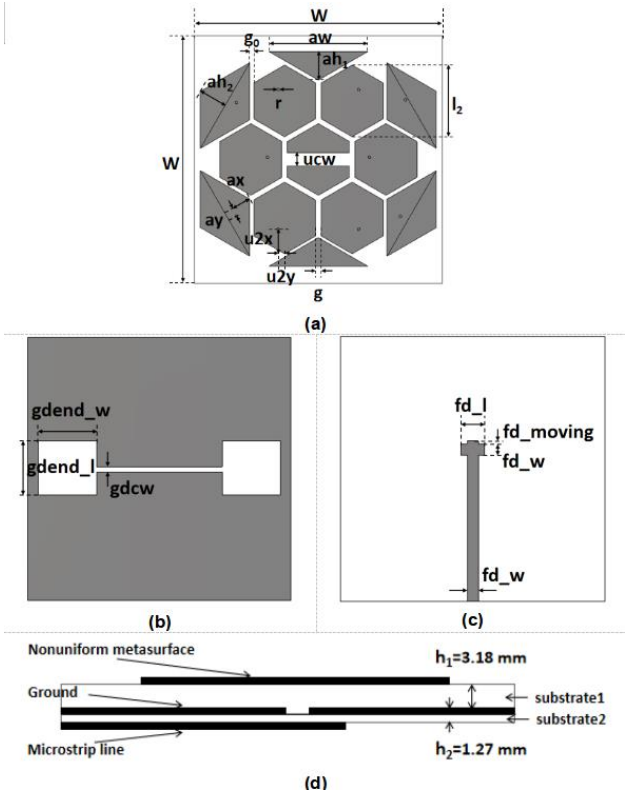

Figure 4.11. Geometry of the proposed MTS antenna using nonuniform unit cells. (a) MTS layer. (b) Ground plane layer. (c) Feedline layer. (d) Side view.

The layout of the proposed antenna is shown in Fig. 4. 11. The detail dimensions are: W= 45 mm, l_2= 13 mm, aw= 18 mm, ah_1= 5.2 mm, ah_2= 5.2 mm, g= 0.8 mm, g_0= 0.7 mm, ucw= 2.3

mm, *r*= 0.25 mm, *u2x*= 4.5 mm, *u2y*= 1.2 mm, *ax*= 3.7 mm, *ay*= 1.5 mm, *fd_w*= 1.9 mm, *fd_l*= 4 mm, *fd_moving*= 0.5 mm, *gdcw*= 0.9 mm, *gdend_w*= 10 mm, *gdend_l*= 9.3 mm. Firstly, a basic MTS antenna using seven hexagonal radiating unit cells with a center slot is designed. Next, to further improve the impedance bandwidth while keeping the structure compact, six polygon-shaped parasitic unit cells are added around the seven hexagonal radiating unit cells. Then, to achieve a lower frequency band at around 2.45 GHz, shorting pins are added at ten of these radiation unit cells. The positions of the shorting pins will affect the impedance bandwidths both at the lower frequency and the higher frequency band, to be discussed further in the next section.

The proposed nonuniform MTS antenna consists of the MTS layer, the ground plane layer, and the feedline layer. Two substrate materials are used to connect these three-layer structure respectively. A Rogers RT5870 substrate is used for connecting the MTS layer and the ground plane layer, whose dielectric constant and thickness are 2.33 and 3.18 mm respectively. An alternative substrate material TMM6 is used to support the ground plane layer and the feedline layer. The geometry and detailed dimensions of the above-mentioned layers are shown in Fig. 4. 11(a), (b) and (c).

2) Mode analysis of the MTS antenna with shorting pins

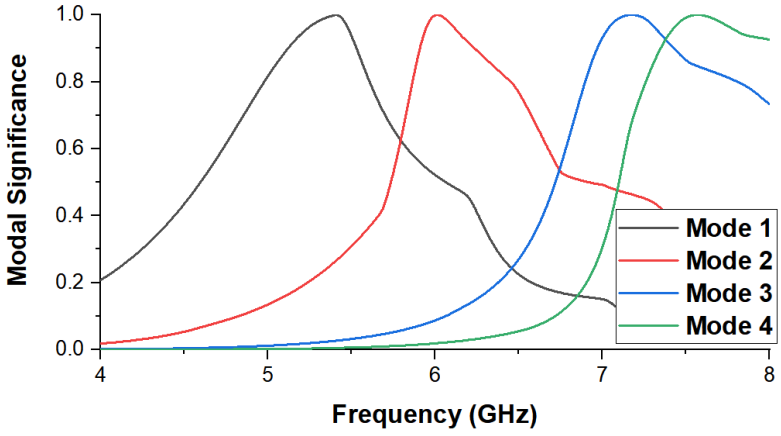

Figure 4.12. Modal significance of the proposed MTS.

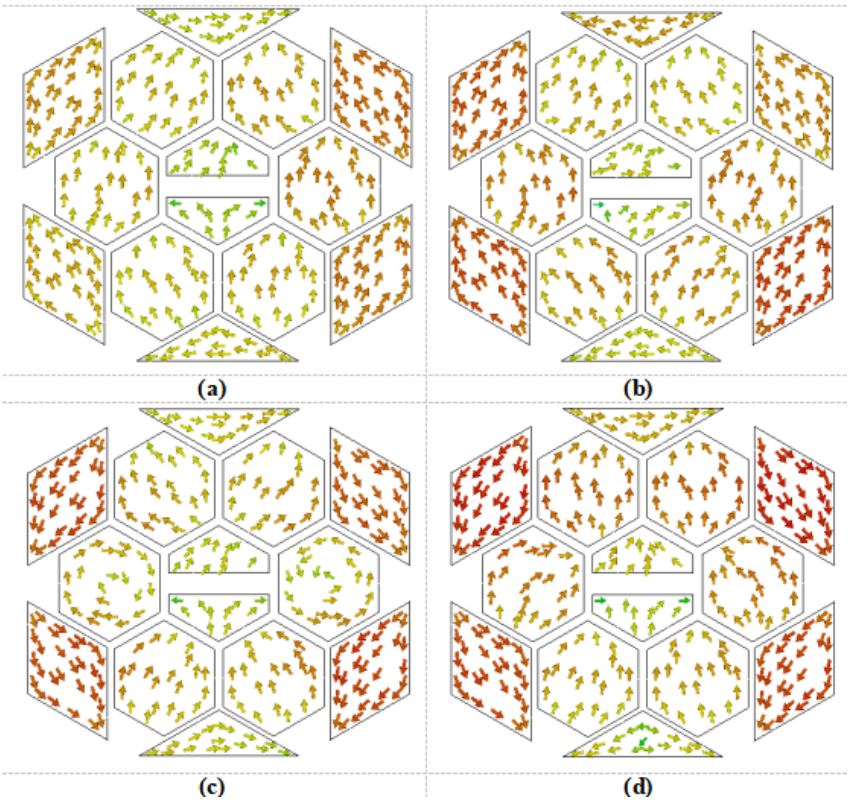

Figure 4.13. Modal current distributions of (a) Mode 1, (b) Mode 2, (c) Mode 3, and (d) Mode 4.

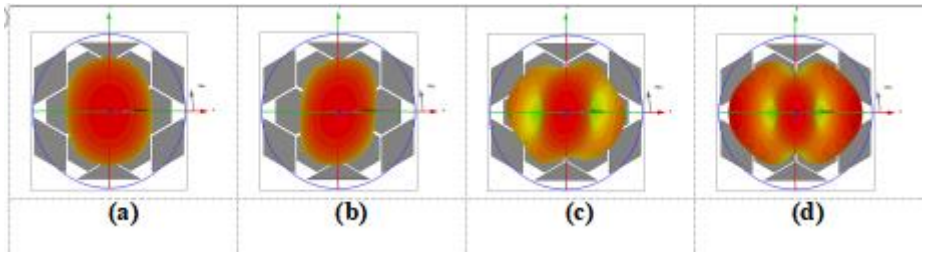

Figure 4.14. Modal radiation patterns of (a) Mode 1, (b) Mode 2, (c) Mode 3, and (d) Mode 4.

For symmetry, simplicity and compactness, regular tessellation structures are desirable shapes to construct an MTS. The hexagonal structure can potentially achieve the broadest bandwidth, compared with the other tessellation shapes [28].

To better understand the modes excited in this proposed antenna, the proposed MTS layer is analyzed by the characteristic mode analysis with simulation software CST MWS and the first four modes are calculated. The boundary of the ground plane is set as electric while the rest five boundaries are all set as open, which is detailed described in Chapter 3. Simulations are carried out from 4 to 9 GHz. The modal significance, modal current distributions, and modal

radiation patterns at resonant frequencies are illustrated in Figs. 4. 12-4. 14. As shown in Fig. 4. 12, Mode 1 resonates at 5.3 GHz. The corresponding current distributions of Mode 1 on the MTS layer mainly in the same direction, as shown in Fig. 4. 13(a). The modal radiation pattern of Mode 1 has a main lobe which is orthogonal to MTS layer, as shown in Fig. 4. 14(a). Mode 2 resonates at around 5.9 GHz. As shown in Fig. 4. 13(b), the modal current distributions of Mode 2 are similar to Mode 1. This current distribution produces a main lobe orthogonal to MTS layer.

Mode 3 resonates at 7.0 GHz. For the modal current distributions shown in Fig. 4. 13(c), the modal currents on the hexagonal elements on the 2nd and the 4th row are in the same direction. While those on the four diamond-shape parasitic elements are of opposite directions to adjacent hexagonal elements. In addition, the modal currents on the hexagonal elements on the 3rd row form a circle. The resonant frequency of this mode can be tuned by changing the size of the four parasitic elements, so that overall operational bandwidth of the MTS based antenna can be adjusted. The radiation pattern of Mode 3 has a main lobe and two side lobes. By contrast, Mode 4 resonates at around 7.6 GHz. As presented in Fig. 4. 13(d), the modal current distributions on the seven hexagonal radiating elements are directed in the same direction while those on the four parasitic elements are with the opposite direction. The modal radiation pattern of Mode 4 is similar to that of Mode 3. To effectively excite these four modes, an aperture-coupled feeding structure is used [26], [27]-[28].

4.4.1.1 Dual-band Performance

To generate a mode in the lower frequency band to achieve dual-band performance, shorting pins are added to the radiating elements. The mushroom-like unit cell, namely, a composite right-/left-handed (CRLH) structure, contains both left-handed (LH) and right-handed (RH) parts. In the structure of the mushroom-like unit cell, the metallic radiating elements can provide series inductance. The gaps between metallic radiating elements can provide series capacitance. The shorting pins connecting the radiating elements and the ground plane can be viewed as shunt inductors. The gaps between radiating elements and the ground plane have shunt capacitance. Among these equivalent components, the series inductance and the shunt capacitance mainly contribute to the RH resonance operation modes at the higher frequency band. Meanwhile, the shunt inductance and the series capacitance mainly contribute to the LH operation modes at the lower frequency band. Dual-band antenna performance can be achieved by the RH and LH resonance operation modes.

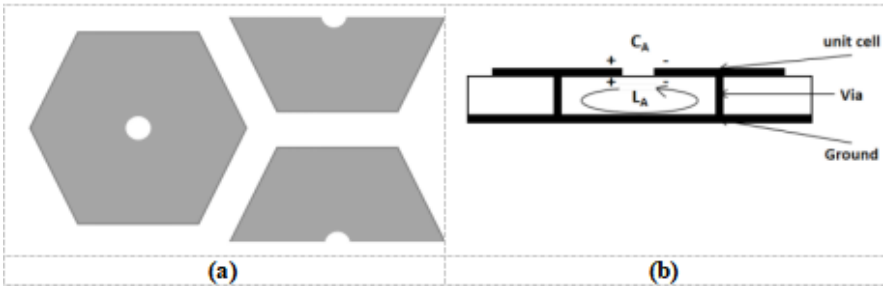

Figure 4.15. Mushroom-like unit cells. (a) hexagonal unit cell arrangement and (b) cross-section of hexagonal unit cell.

Fig. 4. 15(a) shows the hexagonal unit cell arrangement of the proposed antenna. Fig. 4. 15(b) illustrates the cross-section view of the hexagonal unit cells. Adjacent unit cells are connected to ground by shorting pins. The fringing coupling between the adjacent unit cells generates series capacitance. The current loop along the shorting pins, the unit cells and the bottom ground plane constitute inductance. Hence, the resonance at the lower frequency is produced by this capacitance and inductance.

4.4.1.2 Position of Shorting Pins

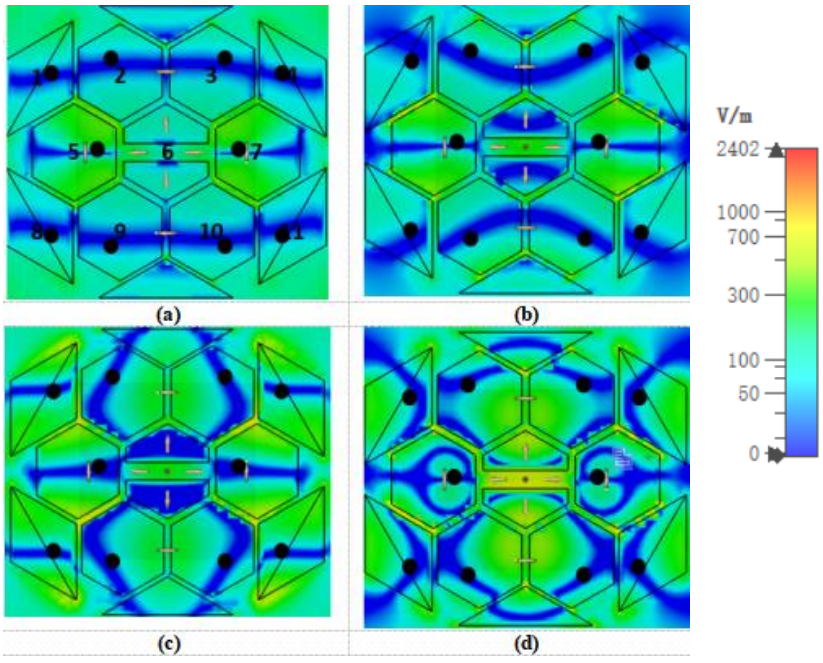

Figure 4.16. Electric field distributions of the proposed MTS antenna at four resonant frequencies in the higher frequency band, with (a) 5.0, (b) 5.8, (c) 7.0 and (d) 7.6 GHz.

More importantly, the positions of the shorting pins at each radiating element can affect the excited modes in both the lower and higher frequency bands. The main consideration is that

the shorting pins should not affect the desired modes excited at the higher frequency band too much. If the shorting pins are added at the nulls of the electric field distribution, the existence of these shorting pins will not greatly affect the above-mentioned TM modes in the higher frequency band due to the equal electric potentials at the two opposite ends of the shorting pins. The positions of the shorting pins are marked as black dots as shown in Fig. 4. 16. The positions of common nulls of electric field distributions at these four resonant frequencies are around: upper-right part of unit 1 and unit 3, lower-right part of unit 8 and unit 10, upper-left part of unit 2 and unit 4, lower-left part of unit 9 and unit 11, and the center part of unit 5 and unit 7.

4.4.2 Parametric Studies

It is important to understand the relationship between the main parameters and the resonant frequencies in both lower and higher bands. Hence, three related parameters are swept to study their effect on antenna performance. They are the size of the hexagonal element (L_2 shown in Fig. 4. 11), the gap between radiating unit cells g, and the radius of the shorting pin r.

In the higher frequency band, the fundamental resonant frequency is mainly related to the dimensions of radiating unit cells. It can be clearly seen in Fig. 4. 17(a) that in the higher frequency band, the larger the value of L_2, the lower the resonant frequencies. By contrast, this relationship is reversed in the lower frequency band.

Apart from the dimensions of radiating unit cells, the gap between adjacent radiating unit cells will also affect the bandwidth since the fundamental frequency will be affected by gap. This is verified by the S-parameter curves shown in Fig. 4. 17(b). When the gap width was decreased from 1.2 mm to 0.8 mm, the fundamental frequency of the higher frequency band was lowered by 10%, from 5.4 GHz to 4.9 GHz while the fundamental frequency of the lower frequency band was lowered by 17%, from 2.45 GHz to 2.05 GHz. In the lower frequency band, the impedance bandwidth is related to the series capacitance and shunt inductance, which are determined by the gap width and the radius of the shorting pins respectively. When the radius of the shorting pins is decreased from 0.45 mm to 0.05 mm, the resonant frequency is decreased as well, as can be seen in Fig. 4. 17(c). The radius of the pins has little effect on the higher radiation band, as the inductance produced by the pins contribute very little to the RH operation resonance.

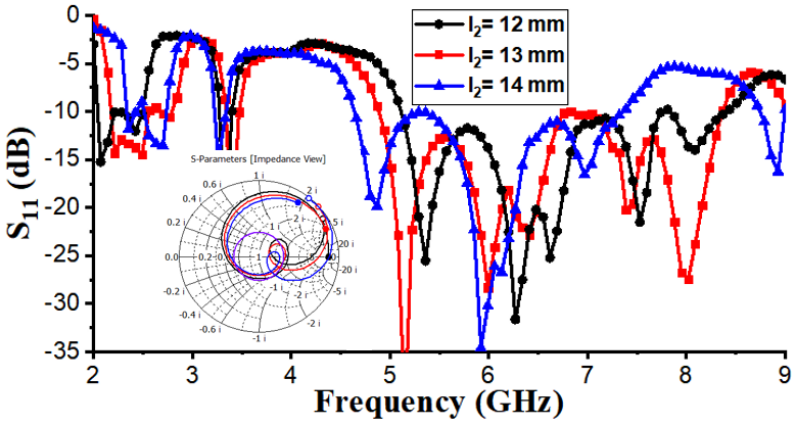

(a)

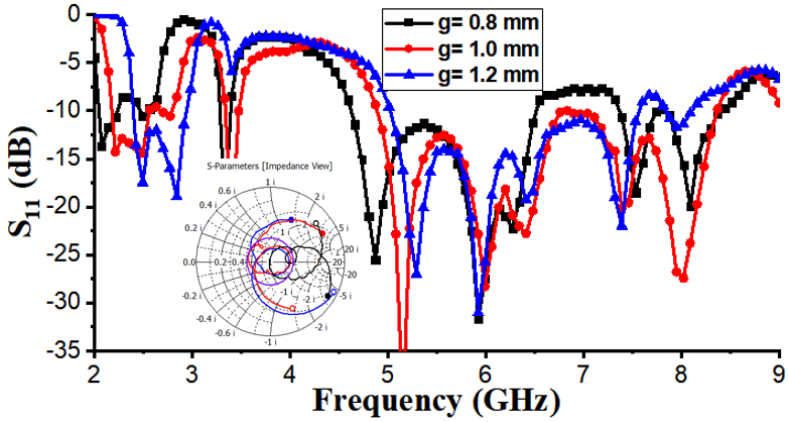

(b)

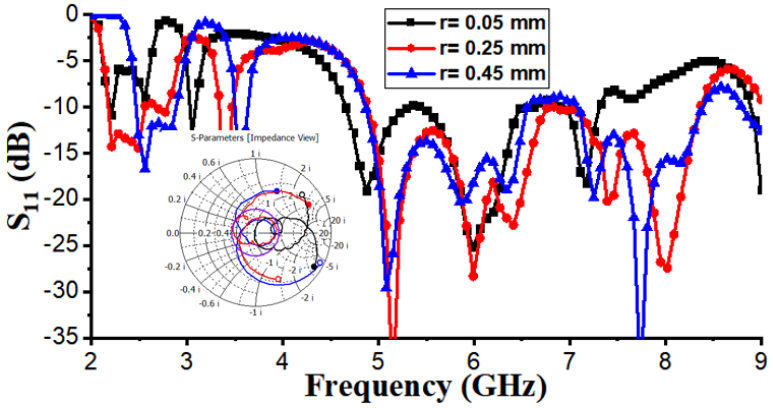

(c)

Figure 4.17. Parametric studies of the proposed antenna, with the variation of (a) the hexagon-shaped unit size (L_2), (b) the gap width between the unit cells (g), and (c) the radius of the shorting pins (r).

4.4.3 Experimental Results

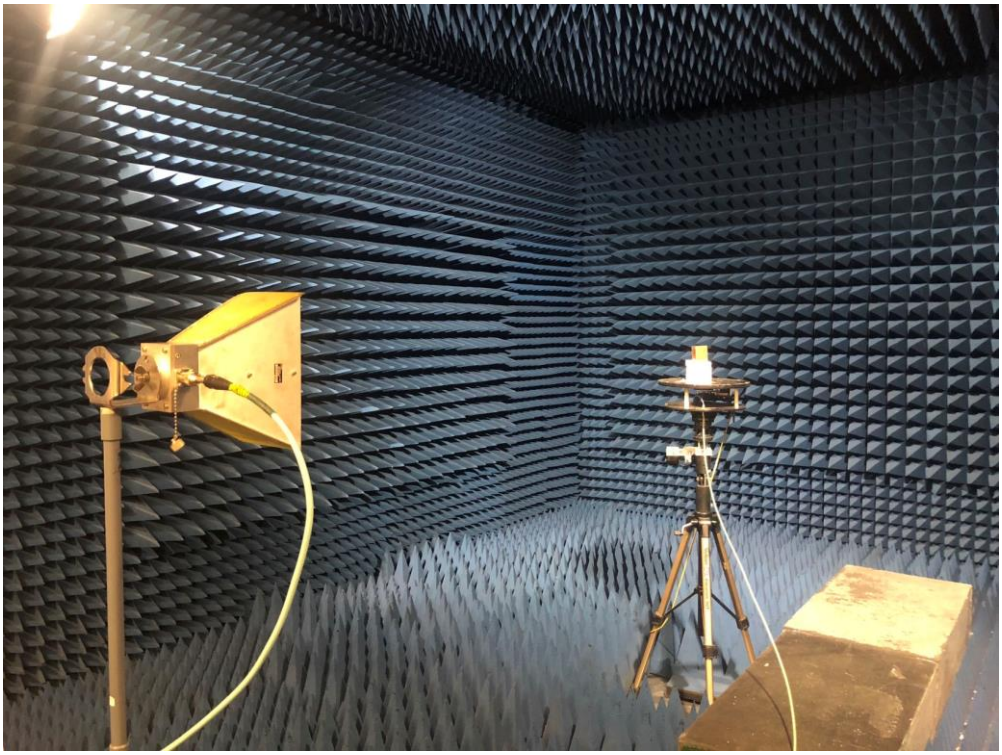

Figure 4.18. Experiment setup.

The experimental setup is shown in Fig. 4. 18. The horn antenna works as the transmitting antenna while the MTS antenna serves as the receiving antenna. The transmitting antenna and the receiving antenna are set in the line of sight aligned to each other. The distance between them is kept as $\frac{2D^2}{\lambda}$ (guarantee far-field environment), where the maximum overall dimension of the antenna is D, and λ is the operating wavelength. Two cables on Port 1 and Port 2 of the vector network analyzer (VNA) are connected to the transmitting and receiving antennas, respectively. The receiving antenna is fixed to the stand whose rotation can be controlled by the stepper motor controller.

VNA can directly read the S_{11} and bandwidth of the receiving antenna. For the radiation patterns measurement, rotate the receiving antenna stand from 0 to 360° on its axis in steps of 30° and record the S_{21} reading from VNA. After that, repeat the measurement for radiation pattern in another plane (E-plane) by rotating both transmitting and receiving antennas by 90°.

To validate the proposed design method, an MTS-based antenna with hexagonal unit cells and parasitic elements was prototyped and measured, shown in Fig. 4. 19(a). Dimensions of the antenna are illustrated in Fig. 4. 11.

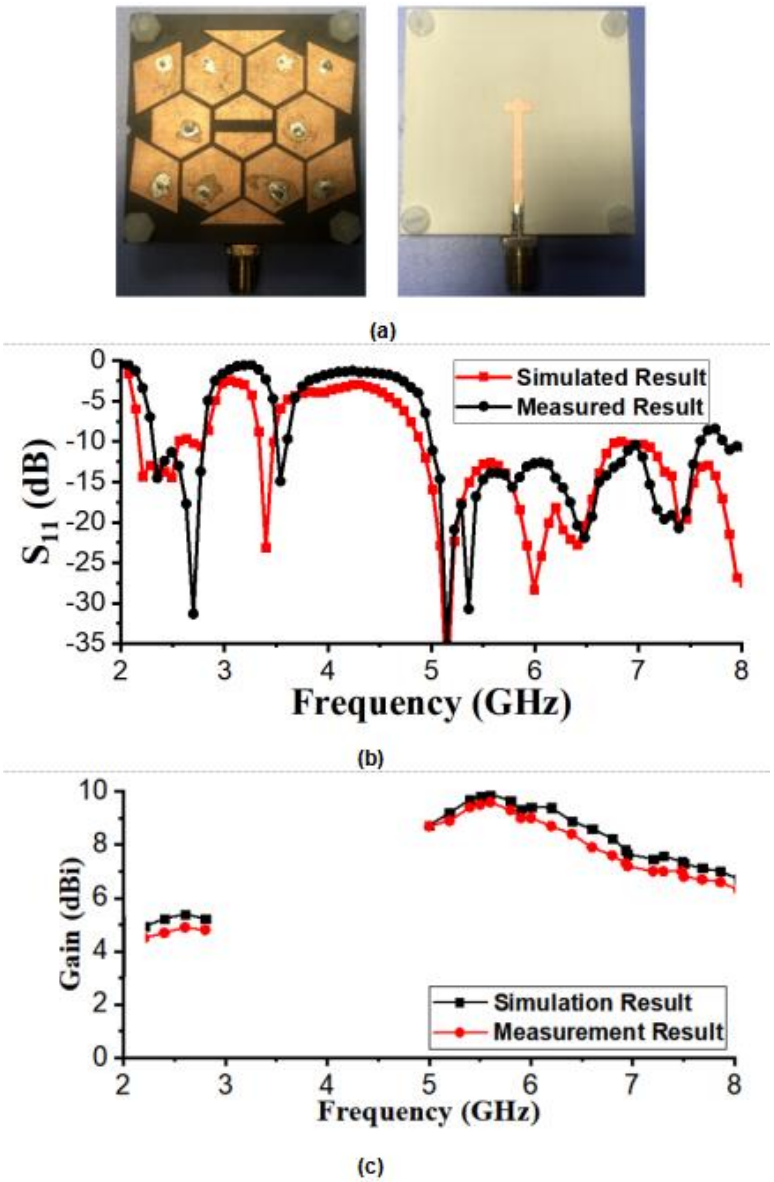

Figure 4.19. (a) Photographs of the fabricated antenna. Simulated and measured (b) S-parameters and (c) gains of the proposed antenna.

Fig. 4. 19(b) presents a comparison between the simulated and measured S-parameters. The simulated bandwidth with a reflection coefficient better than -10 dB in the lower frequency band is from 2.25 to 2.9 GHz and in the higher frequency band is from 4.95 to 8.35 GHz. By contrast, the measured bandwidths in the lower and higher frequency band are from 2.35 to 2.9 GHz and from 4.9 to 8.3 GHz respectively. In the lower frequency band, the simulated and measured fractional bandwidths are 25% and 21%, respectively. In the higher frequency band, the simulated and measured factional bandwidths are 50% and 51.5%, respectively. The difference between simulated and measured results is mainly due to fabrication precision. Especially the tightness between two substrate materials, which was bonded together using

plastic screws, has a greater effect at higher frequencies. The comparison between the simulated and the measured gain of the antenna is shown in Fig. 4. 19(c). In the lower frequency band, the range of the simulated gain is from 4.8 to 5.6 dBi, compared with the scope of the measured gain is from 4.4 to 5.0 dBi. In the higher frequency band, the ranges of simulated and measured gain are from 6.5 to 9.8 dBi and from 6.1 to 9.6 dBi respectively. It should be noted in Fig. 4. 19(b) that there exists a resonant frequency at around 3.8 GHz. This resonant frequency is the zeroth-order mode in the CRLH structure.

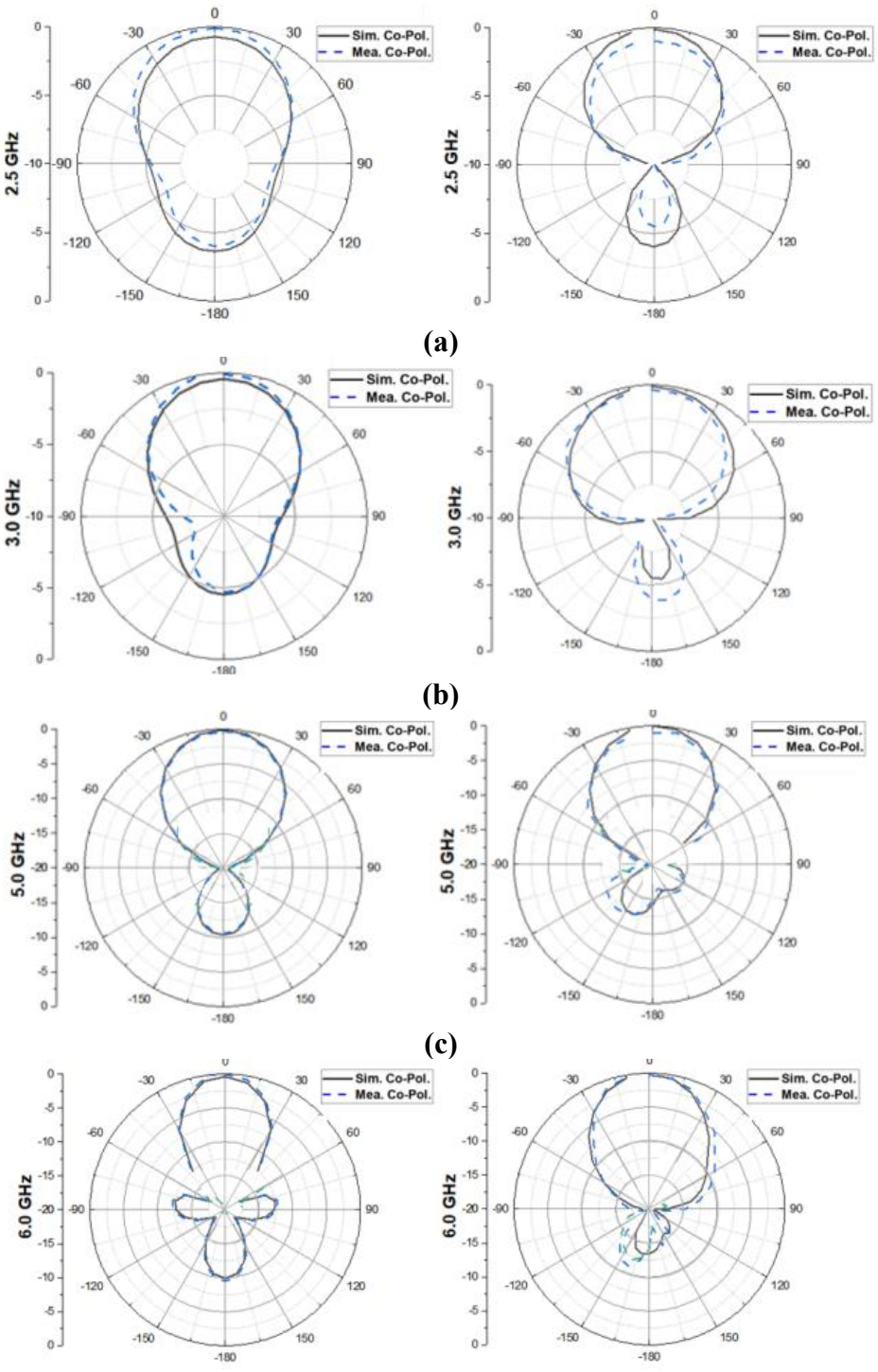

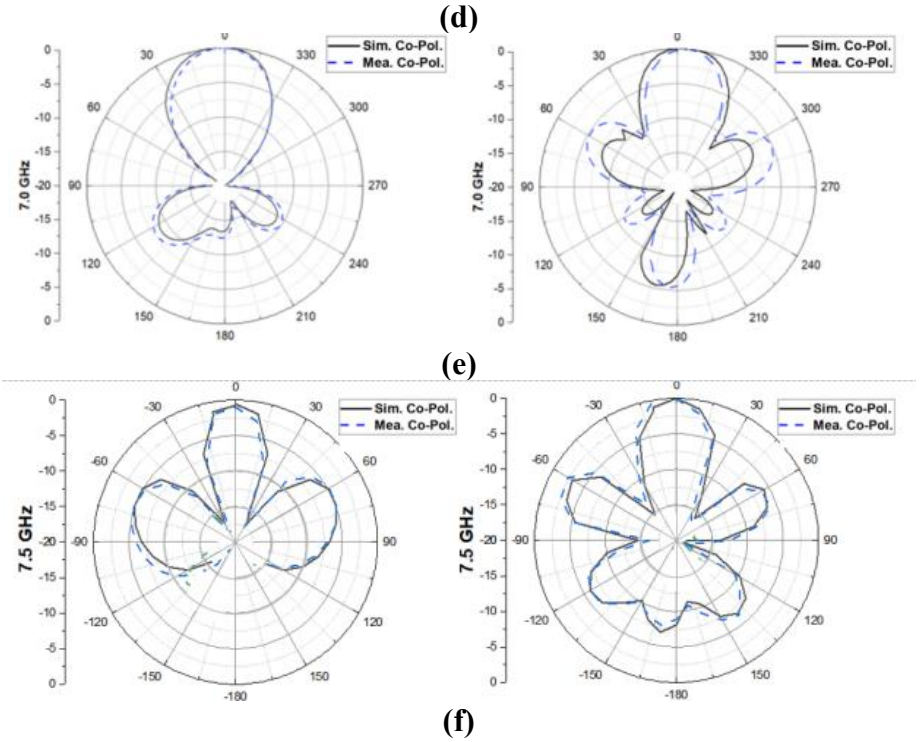

Figure 4.20. Simulated and measured radiation patterns of the proposed antenna at (a) 2.5 GHz, (b) 3.0 GHz, (c) 5.0 GHz, (d) 6.0 GHz, (e) 7.0 GHz and (f) 7.5 GHz.

The normalized radiation patterns of the proposed antenna in the lower and higher frequency band at 2.5, 3.0, 5.0, 5.8, 7.0 and 7.6 GHz are shown in Fig. 4. 20. The simulated and measured results are in good agreement. Due to the symmetry of the feeding structure, both the simulated and measured cross-polarization levels at boresight are below -30 dB in both the xoz and yoz planes over the two operating frequency bands. As can be seen, the proposed antenna has a very directional radiation pattern at 2.5, 3.0, 5.0 and 5.8 GHz. While the radiation patterns at 7.0 GHz and 7.6 GHz have slightly higher side lobes. Overall, consistent boresight radiation with a low cross-polarization level has been achieved across both operating frequency bands.

The size, fractional bandwidth, gain and type of proposed dual-band antenna are compared with the other works, as summarized in Table IV. As can be seen, the fractional bandwidths achieved by the patch antenna [29]-[30] are less than 20% in both frequency bands and the size is not compact enough. Compared with patch antennas, MTS-based antennas, such as those in [32] and our proposed work, are with a more compact size and broader fractional bandwidths in both frequency bands. The metamaterial in [31] is taken as an artificial magnetic conductor, so there exists an additional antenna in the whole design, which will increase the size. Additionally, two bandwidths in [31] are both narrower than those in our proposed antenna

Table IV. Performance Comparison of the Dual-band Directional Antennas.

Ant. Type	Ref. No.	Dimensions (mm^3)	Center Frequency (GHz)	Fractional Bandwidth (%)	Peak Gain (dBi)
Patch Antenna	[29]	$0.8\ \lambda_0 \times 0.6\ \lambda_0 \times 0.006\ \lambda_0$	2.4/5.8	17.67/9.61	2.0/5.58
	[30]	$0.49\ \lambda_0 \times 0.49\ \lambda_0 \times 0.089\ \lambda_0$	2.45/5.35	3.42/17.15	6.97/10.37
Metasurface Antenna	[31]	$0.86\ \lambda_0 \times 0.86\ \lambda_0 \times 0.088\ \lambda_0$	2.4/5.4	15.6/9.3	7.2/7.3
	[32]	$0.264\ \lambda_0 \times 0.24\ \lambda_0 \times 0.034\ \lambda_0$	2.45/5.8	25.8/15.1	2.0/6.9
	This work	$0.375\ \lambda_0 \times 0.375\ \lambda_0 \times 0.035\ \lambda_0$	2.45/5.8	25/50	5.3/9.8

design. Therefore, compared with these designs, the proposed dual-band MTS antenna has achieved broader bandwidths, especially at the higher frequency band.

4.5 Summary

Two MTS antenna designs with bandwidth improvement are proposed for modern wireless communication systems. The unit cells of these two designs are both with hexagonal structure to extend the bandwidth. This chapter explains the benefits of hexagon-shaped unit cells in detail. To further design the dual- broadband MTS antenna, CRLH structure is introduced to provide the other band. Then, the appropriate positions of shorting pins are selected to extend/remain the bandwidth. This chapter verifies that the geometry of unit cell will affect the antenna bandwidth and positions of shorting pins in CRLH structure are critical.

4.6 References

[1] D. Pozar and B. Kaufman, "Increasing the bandwidth of a microstrip antenna by proximity coupling," *Electronics Letters*, vol. 23, no. 8, pp. 368-369, 1987.

[2] C. Aanandan, P. Mohanan, and K. Nair, "Broad-bandgap coupled microstrip antenna," *IEEE Transactions on Antennas and Propagation*, vol. 38, no. 10, pp. 1581-1586, Oct. 1990.

[3] S. Targonski, R. Waterhouse, and D. Pozar, "Design of wideband aperture stacked patch microstrip antennas," *IEEE Transactions on Antennas and Propagation*, vol. 46, no. 9, pp. 1245–1251, Sep. 1998.

[4] M. Martin, B. Sharif, and C. Tsimenidis, "Probe fed stacked patch antenna for wideband applications," *IEEE Transactions on Antennas and Propagation*, vol. 55, no. 8, pp. 2385–2388, Aug. 2007.

[5] F. Yang, X. Zhang, Z. Ye, and Y. Samii, "Wide-band E-shaped patch antennas for wireless communications," *IEEE Transactions on Antennas and Propagation*, vol. 49, no. 7, pp. 1094–1100, Jul. 2001.

[6] Y. Guo, M. Chia, Z. N. Chen, and K. Luk, "Wide-band L-probe fed circular patch antenna for conical-pattern radiation," *IEEE Transactions on Antennas and Propagation*, vol. 52, no. 4, pp. 1115–1116, Apr. 2004.

[7] J. Park, H. Na, and S. Baik, "Design of wideband aperture stacked patch microstrip antennas," *IEEE Antennas Wireless Propagation Letter*, vol. 3, pp. 117–119, 2004.

[8] C. Liu, Y. Guo, and S. Xiao, "Compact Dual-Band Antenna for Implantable Devices," *IEEE Antennas and Wireless Propagation Letters*, vol. 11, pp. 1508-1511, 2012.

[9] D. E. Serup, G. F. Pedersen, and S. Zhang, "Dual-Band Shared Aperture Reflectarray and Patch Antenna Array for S- and Ka-Band," *IEEE Transactions on Antennas and Propagation* (Early access).

[10] C. S. Lee, S. W. Lee, and S. L. Chuang, “Plot of Modal Field Distribution in Rectangular and Circular Waveguides,” *IEEE Transactions on Microwave Theory and Techniques*, vol. MTT-33, no. 3, pp. 271-274, Mar. 1985.

[11] Z. Yang, F. Liang, Y. Yi, D. Zhao, and B. Wang, "Metasurface-based wideband, low-profile, and high-gain antenna," *IET Microwaves, Antennas & Propagation*, vol. 13, no. 4, pp. 436-441, Mar. 2019.

[12] H. Bai, G. Wang, and T. Wu, "High-Gain Wideband Metasurface Antenna With Low Profile," *IEEE Access*, vol. 7, pp. 177266-177273, Dec. 2019.

[13] F. Lin and Z. N. Chen, "Low-Profile Wideband Metasurface Antennas Using Characteristic Mode Analysis," *IEEE Transactions on Antennas and Propagation*, vol. 65, no. 4, pp. 1706-1713, Apr. 2017.

[14] M. S. Alharbi, C. A. Balanis, and C. R. Birtcher, "Performance Enhancement of Square-Ring Antennas Exploiting Surface-Wave Metasurfaces," *IEEE Antennas and Wireless Propagation Letters*, vol. 18, no. 10, pp. 1991-1995, Oct. 2019.

[15] W. Sun, Y. Li, Z. Zhang, and P. Chen, "Low-Profile and Wideband Microstrip Antenna Using Quasi-Periodic Aperture and Slot-to-CPW Transition," *IEEE Transactions on Antennas and Propagation*, vol. 67, no. 1, pp. 632-637, Jan. 2019.

[16] D. Chen, W. Yang, W. Che, and Q. Xue, "Broadband Stable-Gain Multiresonance Antenna Using Nonperiodic Square-Ring Metasurface," *IEEE Antennas and Wireless Propagation Letters*, vol. 18, no. 8, pp. 1537-1541, Aug. 2019.

[17] T. Li and Z. N. Chen, "A Dual-Band Metasurface Antenna Using Characteristic Mode Analysis," *IEEE Transactions on Antennas and Propagation*, vol. 66, no. 10, pp. 5620-5624, Oct. 2018.

[18] Q. Zheng, C. Guo, J. Ding, and G. A. E. Vandenbosch, "Dual-band metasurface-based CP low-profile patch antenna with parasitic elements," *IET Microwaves, Antennas & Propagation*, vol. 13, no. 13, pp. 2360-2364, Oct. 2019.

[19] C. Zhao and C. Wang, "Characteristic Mode Design of Wide Band Circularly Polarized Patch Antenna Consisting of H-Shaped Unit Cells," *IEEE Access*, vol. 6, pp. 25292-25299, Apr. 2018.

[20] X. Yang, Y. Liu, and S. Gong, "Design of a Wideband Omnidirectional Antenna With Characteristic Mode Analysis," *IEEE Antennas and Wireless Propagation Letters*, vol. 17, no. 6, pp. 993-997, Jun. 2018.

[21] D. Ferreira, R.F. S. Caldeirinha, I. Cuiñas, and T. R. Fernandes, " Square Loop and Slot Frequency Selective Surfaces Study for Equivalent Circuit Model Optimization," *IEEE Transactions on Antennas and Propagation*, vol. 63, no. 9, pp. 3947-3954, Sep. 2015.

[22] R. C. Mahajan1 and V. Vyas, " Verification, enhancement and mathematical analysis of EBG structure using complex geomsetrical shapes and eigenmode analysis approach," *SN Applied Sciences*, vol. 30, pp. 1813-1818, Dec. 2019.

[23] N. Nie, X. Yang, Z. N. Chen, and B. Wang, "A Low-Profile Wideband Hybrid Metasurface Antenna Array for 5G and WiFi Systems," *IEEE Transactions on Antennas and Propagation*, vol. 68, no. 2, pp. 665-671, Feb. 2020.

[24] B. Majumder, K. Krishnamoorthy, J. Mukherjee, and K. P. Ray, “Compact Broadband Directive Slot Antenna Loaded With Cavities and Single and Double Layers of

Metasurfaces," *IEEE Transactions on Antennas and Propagation*, vol. 64, no. 11, pp. 4595-4605, Nov. 2016.

[25] J. Wang, H. Wong, Z. Ji, and Y. Wu, "Broadband CPW-Fed Aperture Coupled Metasurface Antenna," *IEEE Antennas and Wireless Propagation Letters*, vol. 18, no. 3, pp. 517-520, Mar. 2019.

[26] N. Nie, X. Yang, Z. N. Chen, and B. Wang, "A Low-Profile Wideband Hybrid Metasurface Antenna Array for 5G and WiFi Systems," *IEEE Transactions on Antennas and Propagation*, vol. 68, no. 2, pp. 665-670, Feb. 2020

[27] Z. Wu, L. Li, X. Chen, and K. Li, "Dual-Band Antenna Integrating With Rectangular Mushroom-Like Superstrate for WLAN Applications," *IEEE Antennas and Wireless Propagation Letters*, vol. 15, pp. 1269-1272, 2016.

[28] W. Zhang, C. Song, R. Pei, Y. Huang, and J. Zhou, "Broadband Metasurface Antenna Using Hexagonal Loop-Shaped Unit Cells," *IEEE Access*, vol. 8, pp. 223797-223803, Dec. 2020.

[29] B. Feng, J. Lai, Q. Zeng, and K. L. Chung, "A Dual-Wideband and High Gain Magneto-Electric Dipole Antenna and Its 3D MIMO System With Metasurface for 5G/WiMAX/WLAN/X-Band Applications," *IEEE Access*, vol. 6, pp. 33387-33398, 2018.

[30] I. Yeom, J. M. Kim, and C. W. Jung, "Dual-Band Slot-Coupled Patch Antenna With Broad Bandwidth and High Directivity for WLAN Access Point," *Electronics Letters*, vol. 50, no. 10, pp. 726-728, 2014.

[31] H. Zhai, K. Zhang, S. Yang, and D. Feng, "A Low-Profile Dual-Band Dual-Polarized Antenna With an AMC Surface for WLAN Applications," *IEEE Antennas and Wireless Propagation Letters*, vol. 16, pp. 2692-2695, 2017.

[32] Z. Wu, L. Li, X. Chen, and K. Li, "Dual-Band Antenna Integrating With Rectangular Mushroom-Like Superstrate for WLAN Applications," *IEEE Antennas and Wireless Propagation Letters*, vol. 15, pp. 1269-1272, 2016.

Chapter 5 Aperture Sharing MTS-Based Wide-Beam Antenna for Energy Harvesting

Metasurface (MTS) antenna can excite different MTS modes due to its unique structure with multiple radiating gaps. Exciting different MTS modes with different frequencies but similar directional radiation patterns simultaneously can achieve an MTS antenna with broad bandwidth. Alternatively, exciting different MTS modes with similar frequencies but various radiation patterns effectively can obtain an MTS antenna with wide beamwidth.

5.1 Introduction

Besides the broadband performance, the wide beamwidth performance is also attractive in antenna performance improvement. The wide beamwidth property will make the MTS antenna suitable for energy harvesting systems.

The rectenna, which consists of an antenna, a matching network, and a rectifying circuit, is commonly used to realize RF energy harvesting. The overall performance of a rectenna is determined by the performance of the antenna and the efficiency of the rectifying circuit [1]-[2]. In practice, if the antenna does not receive enough power from the surrounding environment, the rectenna efficiency will be less than desired. One solution is to increase the input power levels of the antenna in multiple directions, which requires the use of wide-beam or multi-beam antennas to successfully collect incident RF waves from different directions [3].

However, if a wide-beam antenna with one port is used to collect the power, the antenna will inevitably have a low gain, hence a low level of sensitivity due to the low power density. This is because, for a one-port antenna, the gain is normally inversely proportional to the beamwidth [4]. To resolve this problem, the utilization of a wide-beam (or multi-beam) antenna with multiple ports could be a solution. By using multiple ports, the potential of the antenna aperture can be maximized since each port can be assigned to excite one beam focusing on one direction [5].

The MTS antenna can realize the wide beamwidth performance excited by multiple ports. For a conventional N×N MTS antenna, the unit cells on the MTS layer can be regarded as the

radiator. Thanks to these unit cells, single/multiple transverse magnetic (TM) /transverse electric (TE) mode(s) can be excited successfully by using appropriate feeding methods. It has been proved that, by using appropriate feeding methods, different radiation patterns can be achieved, such as directional, directional with tilted angles, omnidirectional, and end-fire radiation patterns [9]-[12]. It indicates that an MTS antenna has the potential to be excited in different ways to realize the desired radiation pattern.

Therefore, for MTS antennas, different modes with different radiation patterns can be excited by suitable feeding methods. By exciting these different modes simultaneously, a wide beamwidth antenna can be achieved to harvest more power.

5.2 Wide-beam Multiport MTS Antenna Design

The purpose of this chapter is to demonstrate that exciting different modes on the MTS layer multiple times and then combining these modes in direct current (DC) way, a receiver with wide beamwidth and high gain can be achieved. The design in this chapter is just an example to verify the feasibility of this idea. The MTS antenna with square unit cells is used as a simple example here. It is easier to analyze the modes with square unit cells than other structures because square unit cells are symmetrical along the x- and y-axis. A 4×4 MTS antenna with square unit cells is proposed, where the number '4' is randomly selected since the difference in the chosen number affects this design is only how many beam numbers are combined finally.

5.2.1 MTS Modes

Without loss of generality, a typical MTS with 4×4 square elements is shown in Fig. 5. 1. Either TM or TE characteristic modes can be excited on the MTS depending on the feeding structures. For this MTS, the fundamental TM mode (TM_{01}) can be excited for radiation if the feed structure is positioned in the middle of the feeding slot between the 2nd and the 3rd column of unit cells. For the TM_{01} mode, the modal current distribution is in phase across the entire MTS [8]. Due to the modal current distribution on the MTS, the radiation pattern will be a directional one. In [7]-[9], a broadside gain of 10 dBi can be achieved for an MTS with 4×4 elements.

Apart from the fundamental TM_{01} mode, it is also possible to excite higher TM_{xy} modes ($x \geqslant 1, y \geqslant 1$) as analyzed in [15]. The choice of the higher TM_{xy} mode is decided by various factors, which will be further discussed in this subsection.

Since the unit cells on the MTS layer are symmetric about the x- and y-axis, there exist pairs of orthogonal higher modes, such as TM_{12} and TM_{21} mode, that can be potentially excited. When the direction of the feeding structure is chosen, only one set of higher modes can be realized.

If the radiation pattern is not a concern, any higher TM_{xy} mode can be considered. However, to complement the directional radiation pattern of the TM_{01} mode, it is desirable to choose those higher TM_{xy} modes with a radiation null in the direction perpendicular to the MTS layer. The reason is that if multiple modes are combined, it will be easier to achieve a wider beamwidth of the combined radiation pattern.

One particular high TM_{xy} mode of interest is described below. For this mode, the modal current distribution is in-phase across the unit cells on the 1st and the 2nd columns. By contrast, the modal current distribution on the 3rd and the 4th column is also in-phase but are out-of-phase with those unit cells on the 1st and the 2nd column. Since the modal current distributions are opposite about the center, this MTS mode has a radiation null in the direction perpendicular to the MTS layer.

Since the modal current distributions of the fundamental TM_{01} mode and this TM_{xy} mode are different, two modes cannot be effectively excited by the same feed simultaneously. In addition, for the higher TM_{xy} mode itself, there are two symmetrical positions where the modal current is maximum, which will induce one main radiation lobe on each side, but a radiation null orthogonal to the MTS layer. This TM_{xy} mode can be excited if one feed structure with two branches is used, with each branch underneath the gap between the 1st and the 2nd column and the gap between the 3rd and the 4th column, respectively.

A better solution is to decompose this mode with two high-gain radiation lobes into two modes. Each of these two decomposed modes is with one main radiation direction. The first decomposed mode is with a stronger current distribution on the 3rd and the 4th column while with a weaker current distribution on the 1st and the 2nd column. Thus, the radiation pattern of this first decomposed mode will have a main lobe inclining along the 1st and the 2nd column and a side lobe inclining along the 3rd and the 4th column. This decomposed mode can be

effectively excited by a feed underneath the gap between the 3rd and the 4th column. By contrast, the second decomposed mode has a stronger current distribution on the 1st and the 2nd column while weaker on the 3rd and the 4th column. The radiation pattern of the second decomposed mode will have the main lobe inclining along the 3rd and the 4th column. The effective feeding position of this decomposed mode is underneath the gap between the 1st and the 2nd column.

To make use of these modes and their associated radiation patterns, three feeding networks with three ports are needed. The dimensions of the MTS elements can be optimized so that the excited decomposed mode will have a similar resonant frequency as the fundamental TM_{01} mode.

These three radiation patterns are generated by three independent feeding ports. Each radiation pattern has a relatively narrow beam but a high gain. For energy harvesting purposes, when a signal is from the left (or right), the right (or left) port can receive the signal with a high gain, respectively. When the signal is from the middle, the centre port can receive the signal with a high gain. The received signal can then be converted to DC individually and combined. Effectively, a rectenna with a high gain and a wide beamwidth is achieved.

5.2.2 Mode Analysis of Proposed Metasurface Antenna

To verify the theory, characteristic mode analysis (CMA) is used to analyze the modes on the proposed MTS layer. Once desired modes are identified, suitable feed structures can be designed to effectively excite these modes.

Normally, in the feed design, it is important to consider the type of the feeding structure and the feeding position. As for the feed type, the aperture-coupled feed type is a conventional method to excite desired modes in an MTS antenna since it can reduce the interference between different layers and be easier to match the impedance [7]-[9], [19]. The apertures on the ground plane can effectively couple electromagnetic energy from the feed to the MTS layer. For the proposed MTS antenna, there are strong modal current distributions at two ends of the unit cells on the MTS layer. If an aperture on the ground plane is positioned right underneath the radiating gaps, it can selectively excite the desired modes [11]-[13]. Therefore, three apertures are positioned right underneath the radiating gaps to excite the three above-mentioned desired modes.

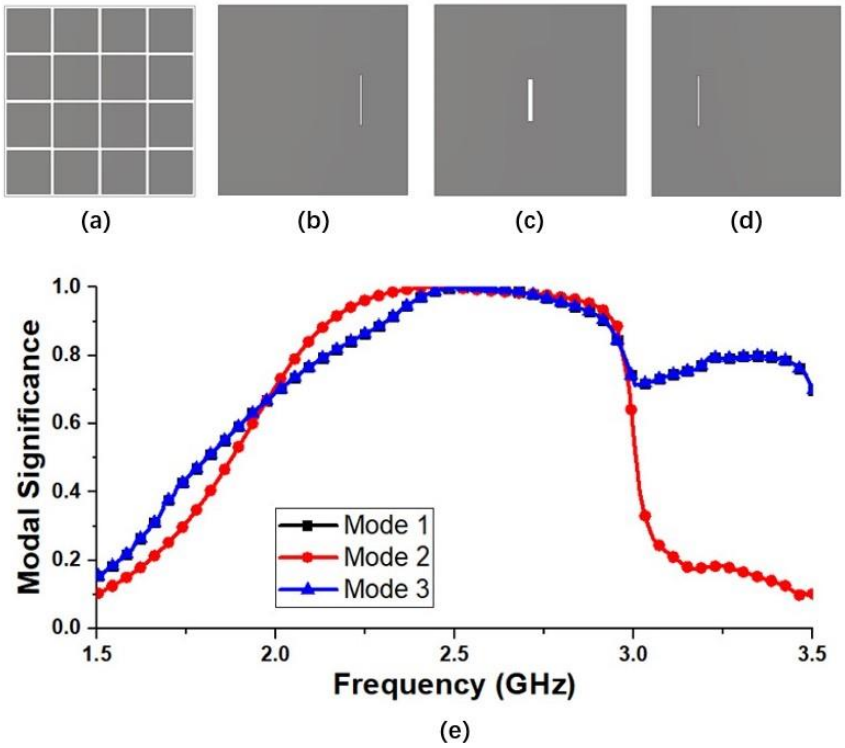

Figure 5.1. Configuration of the MTS antenna: (a) MTS layer, (b) a slot on the right hand side of the ground for exciting Mode 1, (c) a slot in the middle to excite Mode 2 (d) a slot on the left to excite Mode 3, and (e) modal significance of the proposed MTS antenna when excited only from the slot on the right (Mode 1), only the slot in the middle (Mode 2) and only on the left (Mode 3).

To reveal the operation mechanism of the proposed MTS antenna, the MTS layer, two substrates and three apertures on the ground plane are considered. The geometry and layout of the MTS layer remain the same, which are shown in Fig. 5. 1(a). Three feeding positions are shown in Fig. 5. 1(b), (c) and (d), respectively.

Fig. 5. 1(e) shows the modal significances (MSs) for the proposed MTS with different aperture positions on the ground plane. The resonant frequencies of Mode 1 (right aperture-coupled feed), Mode 2 (center aperture-coupled feed), and Mode 3 (left aperture-coupled feed) are all at around 2.45 GHz. Although Mode 1 and Mode 3 are two decomposed high TM_{xy} modes, of which frequencies should be higher than the fundamental mode, the difference between the resonant frequencies of the fundamental mode and the decomposed higher TM_{xy} modes is not large. Hence, these three modes can be excited at a similar resonant frequency. After effectively exciting these three modes, the modal current distributions, and the radiation patterns of Mode 1, Mode 2, and Mode 3 are shown in Fig. 5. 2. It can be seen that the current distribution of the

fundamental TM_{01} is in phase across the MTS layer, and the main beam of the radiation pattern of the fundamental mode is perpendicular to the MTS surface. For Mode 1, the current distribution is in-phase across the unit cells on the 1st and the 2nd columns, but out-of-phase with the current distribution on unit cells of the 3rd and the 4th columns. The amplitude of modal current distributions on unit cells of the 3rd and the 4th column is much stronger than that on the 1st and the 2nd column, which is because of the aperture-coupled feed being on the right. The radiation pattern induced by the modal current distribution is shown in Fig. 5. 2. The main beam is tilted to the left side, and the side lobe is tilted to the other side.

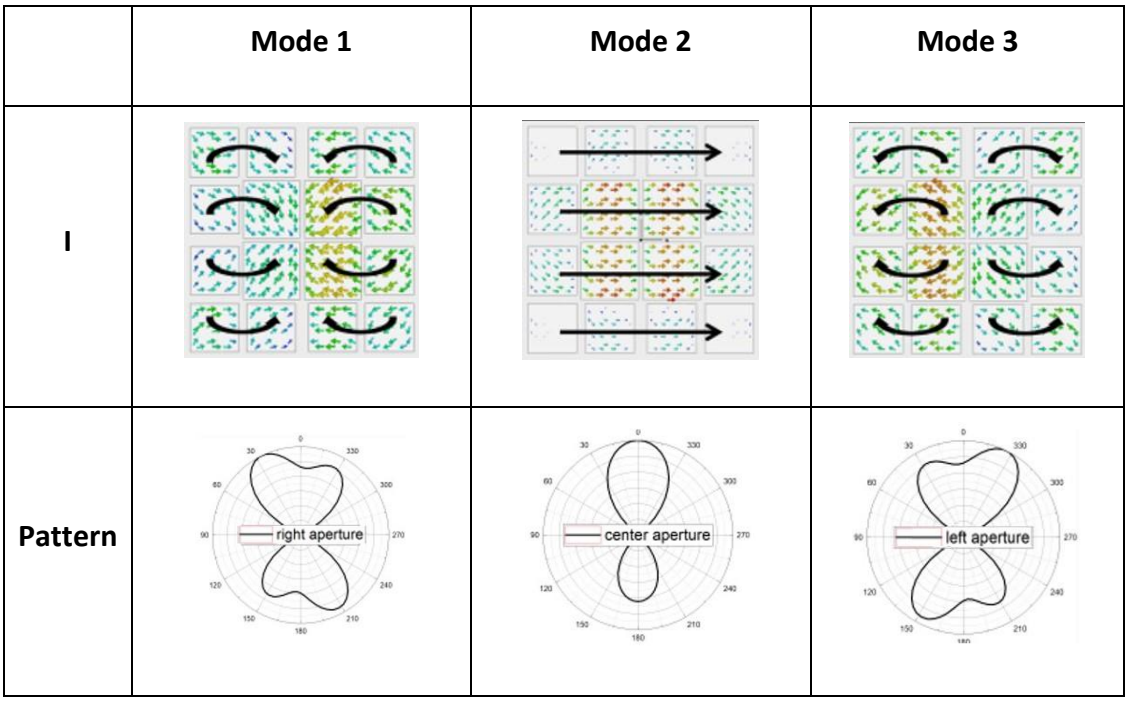

Figure 5.2. Modal currents distributions, and modal radiation patterns of Mode 1, Mode 2, and Mode 3.

For Mode 3, since it is totally symmetrical with Mode 1, its modal current distribution and radiation pattern are symmetrical with those of Mode 1.

5.2.3 Mode Analysis of Proposed MTS Antenna

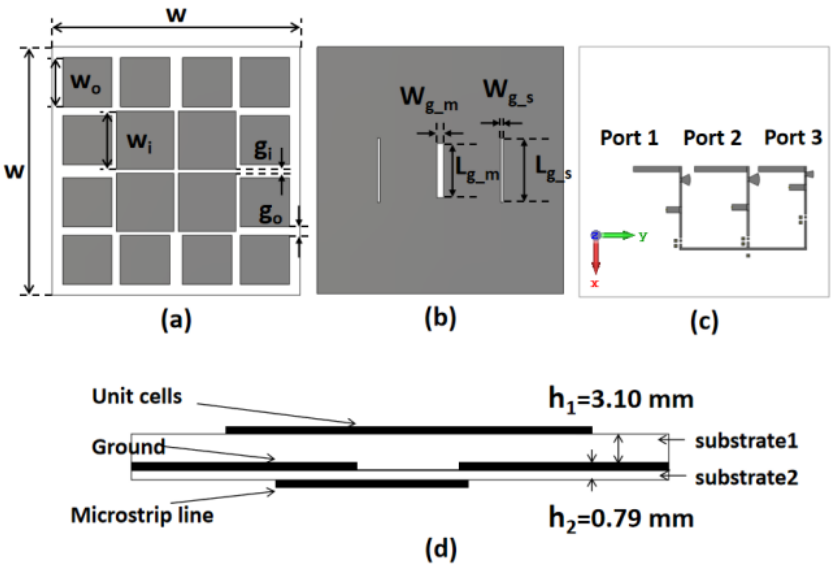

Figure 5.3. Geometry of the proposed wide-beam multi-port MTS antenna. (a) Top view of the MTS layer. (b) Top view of the ground plane. (c) Bottom view of the feed layer. (d) Side view of the whole structure. (w= 120 mm, w_i= 28 mm, w_o= 23.8 mm, g_i= 2 mm, g_o= 6.2 mm, l_{g_m}= 26.6 mm, w_{g_m}= 3.2 mm, l_{g_s}= 31.2 mm, w_{g_s}= 1.2 mm).

To verify the above analysis, a wide-beam and high gain MTS antenna with multiple ports is designed as shown in Fig. 5. 3. The proposed MTS antenna is composed of three layers: the MTS layer, the ground plane layer, and the feeding and rectifying circuit layer. A Rogers RT6002 substrate and a Rogers RT5880 substrate were used to connect these three layers. The heights of the two substrates are 3.1 mm and 0.79 mm, respectively. The geometry and detailed dimensions of the MTS layer and ground plane layer are shown in Fig. 5. 3.

On the MTS layer, there are in total 16-unit cells of square metal plates. The sizes of the four inner unit cells are the same and are larger than that of those 12 outer unit cells. For the decomposed modes, if the ratio of the inner cell size and the outer cell size is changed, the resonant frequency, the beamwidth and the gain will change accordingly. When the ratio is increased, the beamwidth decreases while the gain increases. It is worth noting that this proportional/inverse-proportional relationship does not apply to the fundamental mode. On the ground plane layer, there are three vertical apertures. The positions of these apertures are aligned with the positions of those three vertical gaps between elements on the MTS layer. On the feeding and rectifying circuit layer, three horizontal transmission lines are positioned underneath and orthogonal to the three apertures on the ground plane as feeding lines.

Current distributions of these three modes after being excited individually are demonstrated in Fig. 5. 4(a), (c), and (d), respectively. They agree well with the mode analysis by CMA. Fig. 5. 4(b) shows the current distribution of the high TM_{xy} mode when fed by a feeding structure with two branches. In this feeding structure, a power divider is used to split the power into two branches. The positions of the two branches and the coupling apertures for these two branches are very similar to that for Mode 1 and Mode 3. This high TM_{xy} mode is shown here to demonstrate how it can be transformed to Mode 1 and Mode 3.

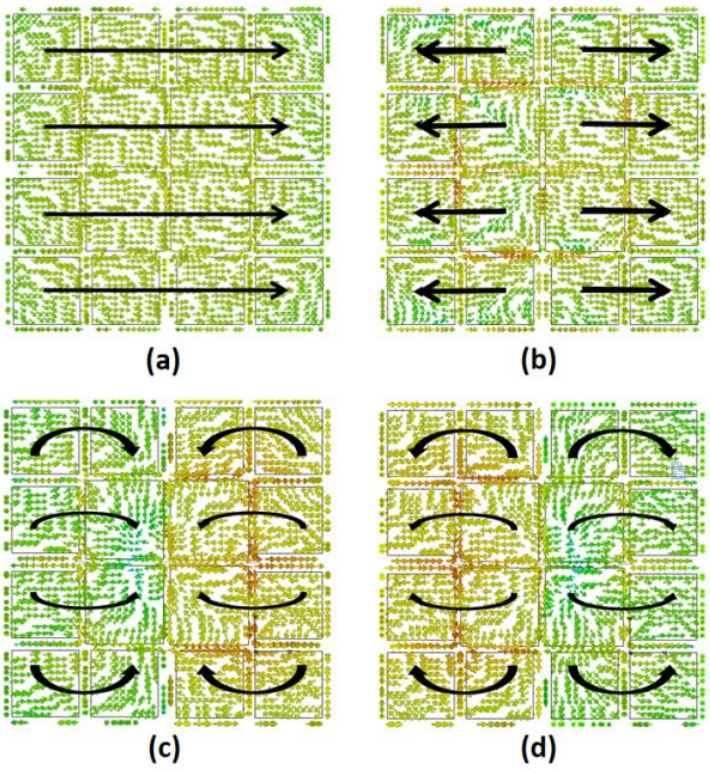

Figure 5.4. Current distributions of the proposed MTS antenna on the xoy plane at (a) the fundamental MTS mode (TM_{01}) excited at Port 2, (b) the higher TM_{xy} mode excited by a feeding structure with two branches, (c) the decomposed higher mode excited at the Port 1, and (d) the decomposed higher mode excited at Port 3.

5.2.4 Rectifier Design

Three different modes with different radiation patterns as mentioned above can be combined to effectively widen the angle coverage of RF energy harvesting. The harvested RF power needs to be converted to DC and combined to power a single load. The topology and detailed dimensions of a single-branch rectifying circuit are shown in Fig. 5. 5. The circuit consists of a transmission line which is the feed to the antenna, an impedance matching network, and a

voltage-doubler rectifying circuit. The DC output was combined with other branches to power a load.

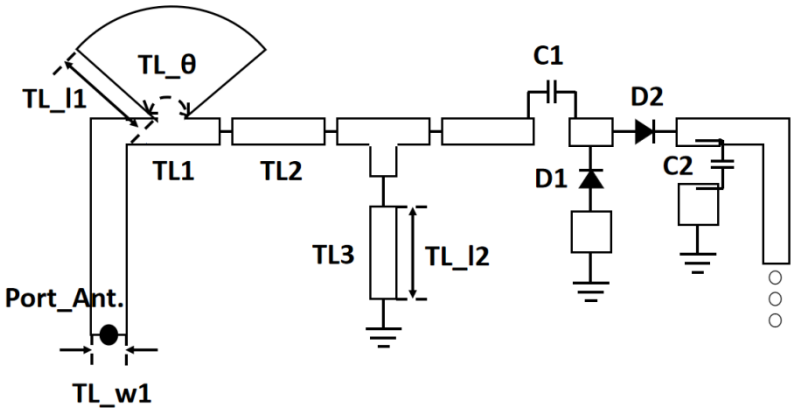

Figure 5.5. Topology of a single branch voltage doubler rectifying circuit. (TL_w_1= 2.5 mm, TL_l_1= 3.2/4.8/4.0 mm (for all three branches), TL_l_2= 7.3/7.3/6.3 mm (for three branches), TL_θ= 52.3/26.5/55º (for the right/middle/left branch respectively), C_1= 1000 pF, C_2= 100 pF).

This rectifier is fabricated on a 0.813-mm-thick RT5880. It is shown as Substrate 2 in Fig. 5. 3(d). The dielectric constant is 2.2 and the loss tangent is 0.0009. In the impedance matching part, the network consists of a radial stub and a short stub, as shown in Fig. 5. 5. The radial stub TL_1 is regarded as an open stub, which is equivalent to an adjustable capacitor by adjusting its angle. This capacitance value can be more easily matched to achieve a broadband performance, compared to a quarter stub. The short-circuit stub TL_3 is used to cancel the imaginary part of its input impedance, making the real part nearly constant. The matching network is implemented by transmission lines rather than lumped elements to reduce loss. The rectifier consists of two diodes D_1 and D_2 and two capacitors C_1 and C_2. Schottky diodes SMS7630 were selected because of their low biasing voltage requirement [16].

5.3 Measurement Result

5.3.1 Antenna measurement

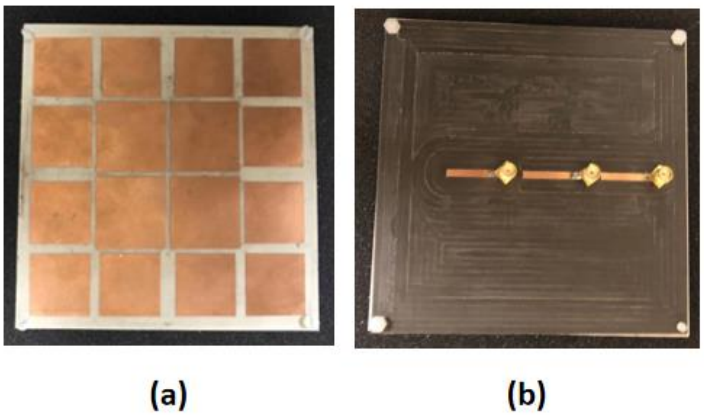

Figure 5.6. Photograph of the fabricated antenna. (a) Front view. (b) Back view of the antenna.

The front and back views of the fabricated MTS antenna are demonstrated in Fig. 5. 6. The simulated and measured S_{11} and gain of the antenna are compared in Fig. 5. 7 and Fig. 5. 8, respectively. The simulated bandwidth of the MTS antenna with -10 dB reflection coefficient is 19.6% when the antenna is excited at Port 2, and 7% at Port 1 and Port 3 while the measured one is 22% at Port 2, and 12% at Port 1 and Port 3. The measured bandwidth is much wider than the simulated one because of the fabrication loss. The simulated and measured gain when the antenna is excited by the center and the two side ports are 9.5 dBi and 8.7 dBi, respectively, at 2.45 GHz.

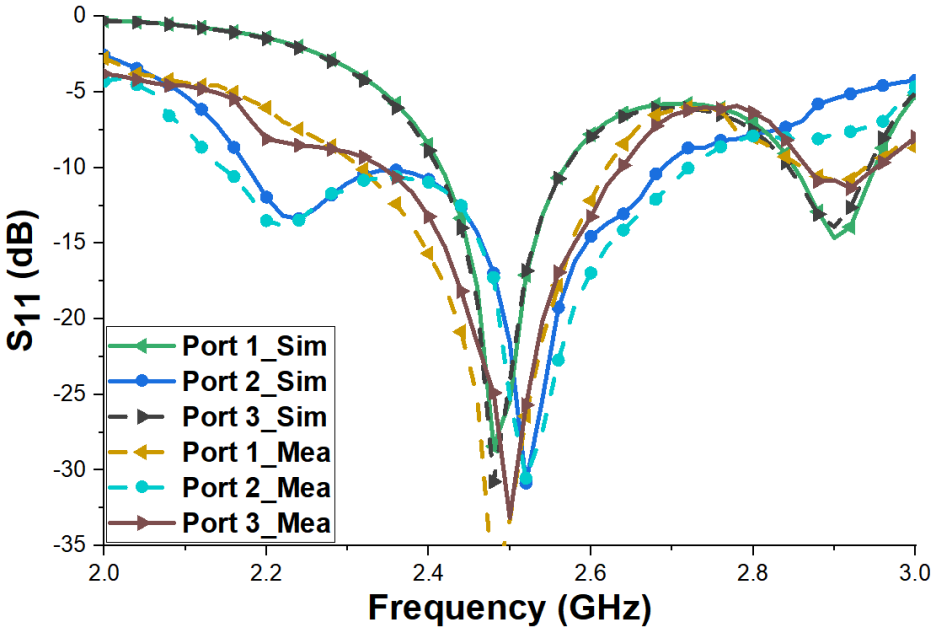

Figure 5.7. Simulated and measured reflection coefficients when the antenna is excited by Port 1, Port 2, and Port 3, respectively.

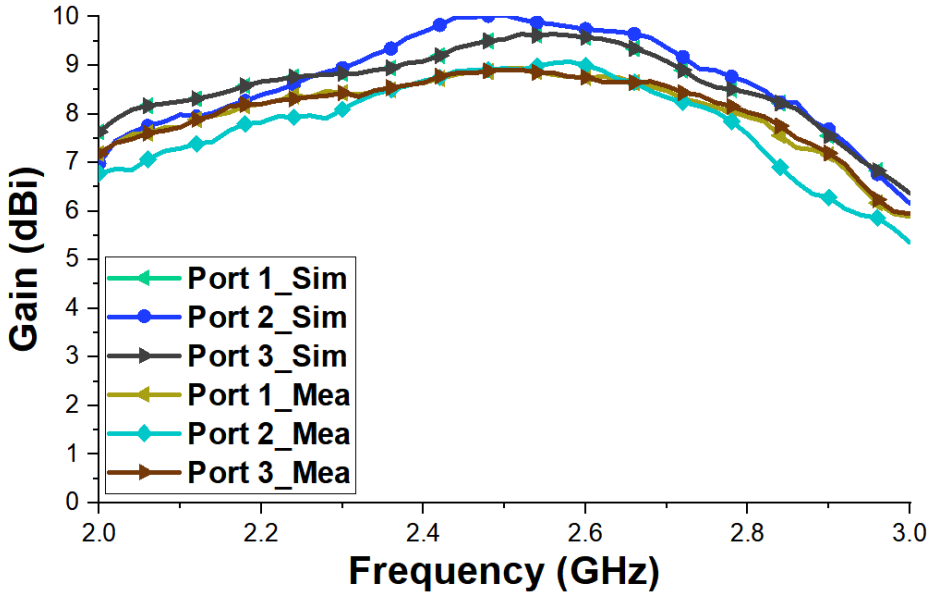

Figure 5.8. Simulated and measured gains when the antenna is excited by Port 1, Port 2, and Port 3, respectively.

Fig. 5. 9 shows the simulated and measured normalized radiation patterns of the MTS antenna at 2.45 GHz. The tilted-angles of H-plane radiation patterns when excited by each port are at +35°, 0°, and -35°, respectively. The beamwidth for each port is around 46°. For energy

harvesting applications, when the DC output powers from the three ports are combined, a wide beamwidth of 117° can be achieved, effectively. The beamwidth for each port in E-planes are similar, at around 90°. The measured normalized radiation patterns are all in good agreement with the simulated results.

	H-plane	E-plane
Port 1	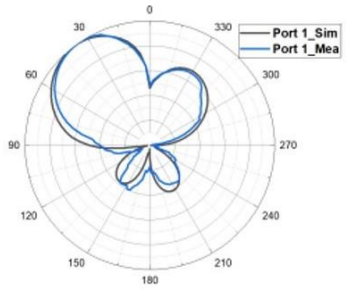	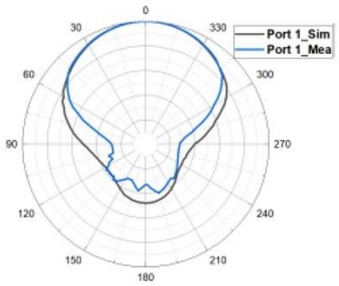
Port 2	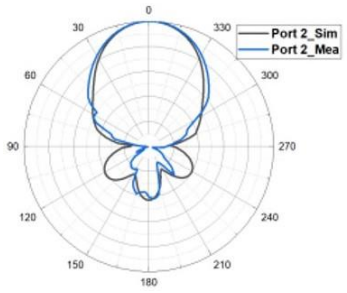	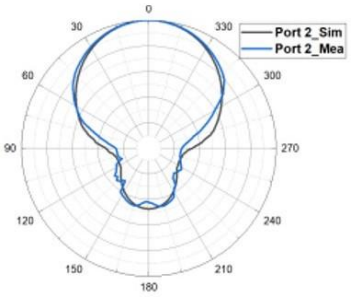
Port 3	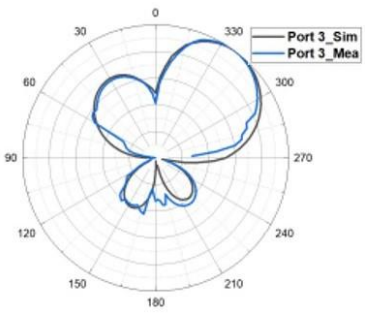	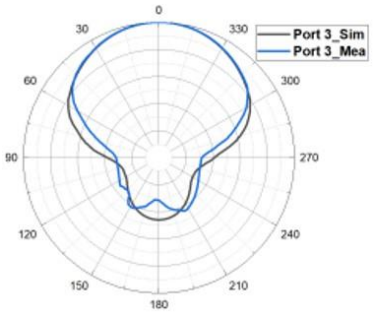

Figure 5.9. Simulated and measured normalized radiation patterns at 2.45 GHz when the antenna is excited by Port 1, Port 2, Port 3, respectively, and the effective radiation pattern when they are combined.

5.3.2 Rectifier measurement

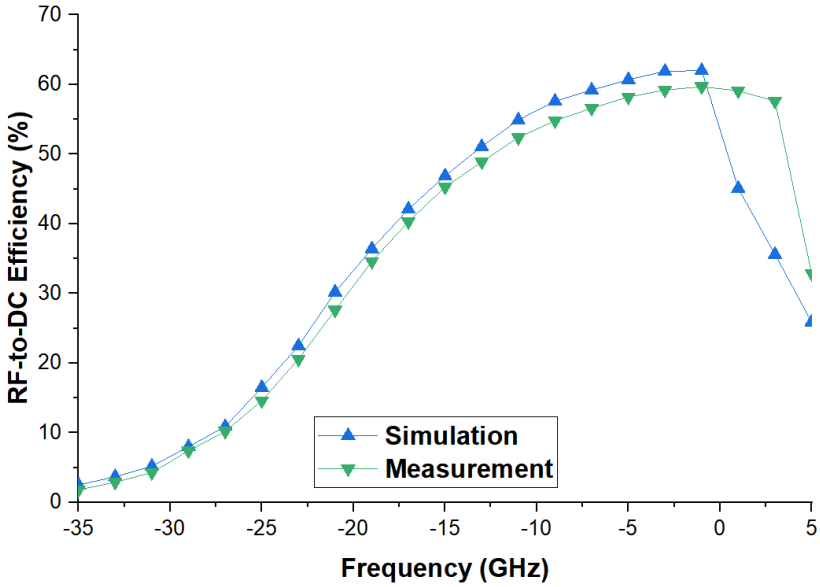

Figure 5.10. Simulated and measured RF-to-DC conversion efficiency of the rectifier versus different input power levels at 2.45 GHz with a resistive load.

Three rectifiers are connected to Port 1, Port 2, and Port 3 of the MTS antenna, respectively, for RF-to-DC conversion. The output DC voltage V_{DC} of the rectifier is measured across the resistive load R_L. To evaluate the RF-to-DC conversion efficiency of the rectifier, the rectifier is connected to a signal generator, and a multimeter is used to measure the V_{DC}. The RF input power was from -35 to 5 dBm at 2.45 GHz. The RF-to-DC conversion efficiency of the rectifier can be obtained from

$$\eta = \frac{V_{dc}^{\ 2}}{R_L} \times \frac{1}{P_{in}} \tag{5.1}$$

where P_{in} denotes the input RF power provided by the signal generator. The measured RF-to-DC conversion efficiency of the rectifier versus input RF power levels is plotted in Fig. 5. 10. It can be seen that, for the rectifying circuit with a single load resistance, the maximum conversion efficiency is around 63% at -1 dBm, and over 30% when the input power level is higher than -20 dBm. This rectifier circuit can still work with an efficiency of around 1.5% at a low input RF power level of -35 dBm.

5.3.3 Rectenna measurement

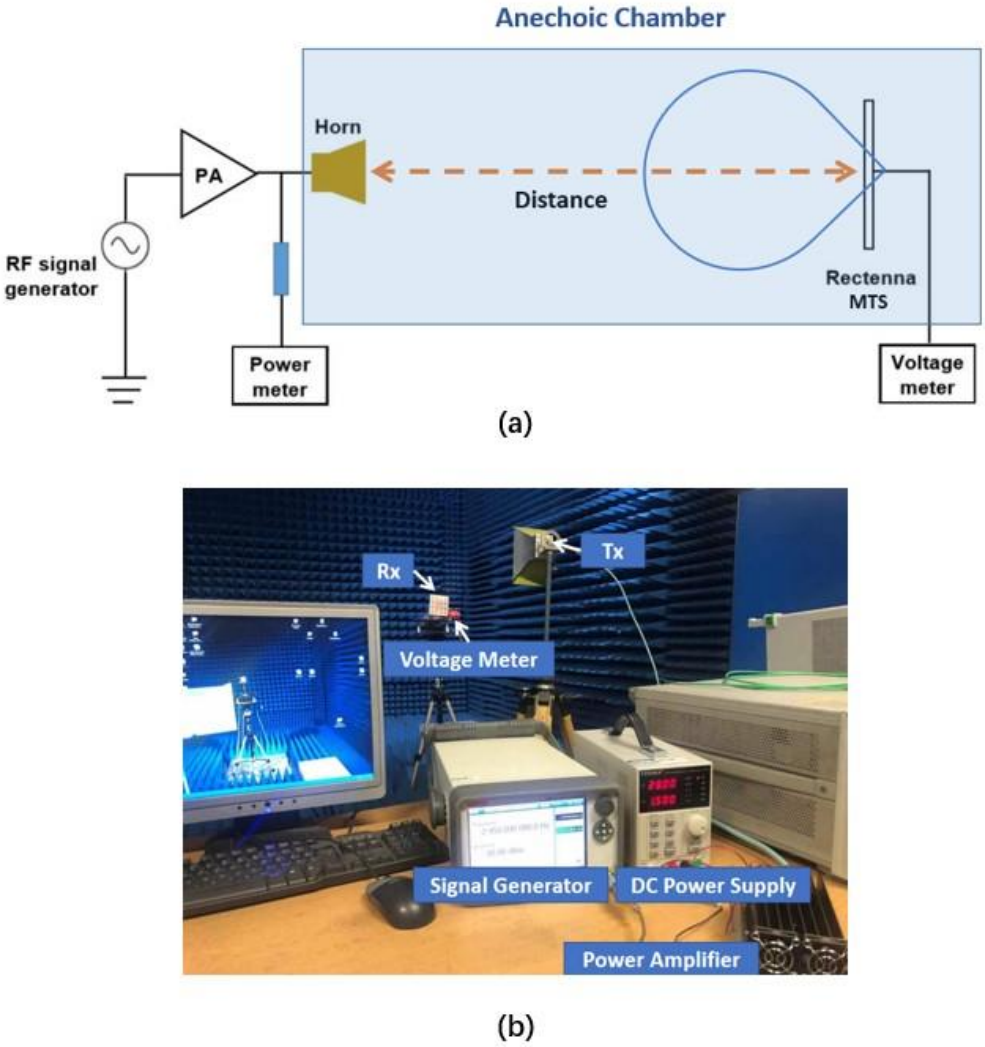

Figure 5.11. (a) Diagram and (b) photograph of the measurement setup.

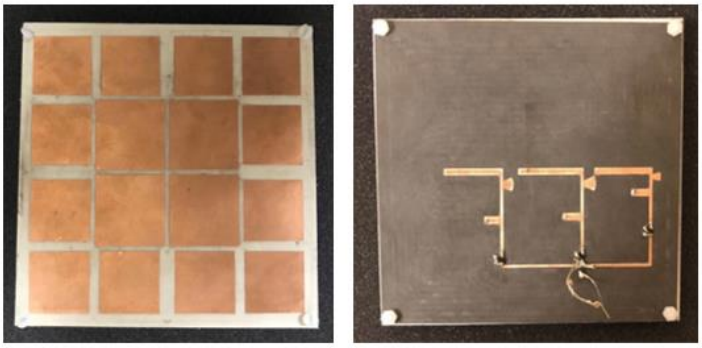

Figure 5.12. Photograph of the proposed rectenna. Front and back view.

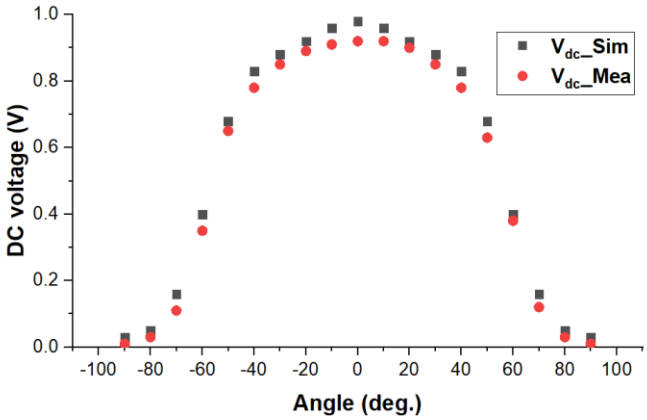

Figure 5.13. DC output voltage versus different incident angles.

The measurement setup of the rectenna is shown in Fig. 5. 11. The source signal was generated by a Keithley 2920 RF signal generator and was amplified by a 43 dB gain power amplifier. The signal was transmitted by a calibrated horn antenna. The proposed rectenna was used to receive the signal at 1 m from the transmit antenna. The front and back views of the proposed rectenna are shown in Fig. 5. 12. The power delivered to the transmit antenna was measured by a power meter while the received power by the rectenna was calculated using the Friis transmission equation [20]:

$$P_r = P_t + G_t + G_r + 20\log_{10}\frac{\lambda}{4\pi r} \tag{5.2}$$

where P_r is the received power in dBm, P_t is the transmitting power in dBm (43), G_t is the gain of the horn in dBi (9.8), G_r is the gain of the proposed rectenna in dBi, λ is the free space wavelength at 2.45 GHz, and r is the distance between the transmitter and the receiver in meter (1). The measurement was carried out in an anechoic chamber. The power density at the rectenna was controlled to be 1 μW/cm^2 at 2.45 GHz. The rectenna was rotated over a 180°

angle to vary the incident angle of the RF radiation on the rectenna. The DC output voltage was measured after every 5° rotation. The total RF-to-DC conversion efficiency of the rectenna could then be calculated. The DC voltages of Ports 1, 2, and 3 are mathematically combined. In Fig. 5. 13, the combined output voltage of three ports is simulated and measured at different incident angles. The measured output DC voltage was over 0.7 V within the angle range of -50° to +50° and was over 0.3 V from -60° to +60°. It is noted that the simulated 3 dB beamwidth of the receiver is around 117°, which combines the beamwidths of Port 1, Port 2, and Port 3. The measured beamwidth of the receiver is about 100° because of the fabrication tolerance. The effective beamwidth of the proposed rectenna is 2.5 times that of the rectenna with a single port. Fig. 5. 13 verified that the proposed design method could achieve an extended angle coverage range.

In Table V, the achieved results are compared with other multi-port rectennas designed for harvesting energy from low power RF sources. The gain of the proposed MTS rectenna, when excited by individual ports, is comparable with that of other rectennas. Compared with [17], the proposed rectenna has a much simpler structure, smaller dimensions, and a wider beamwidth. By using a grid-array antenna in [5], the size of the whole rectenna is five times bigger than the proposed rectenna. Compared with the rectenna design with a similar size, the beamwidth of our rectenna is 30% wider than that in [6].

Table V. Comparison of the Proposed Rectenna and Related Designs.

Ref.	Rectenna Dimension (mm^3)	Complexity of the Overall Design	Frequency (GHz)	Overall -3dB beamwidth (°)	Peak Gain (dBi)	RF-to-DC conversion efficiency (%)
[17]	$2.0\lambda_0 \times 0.83\ \lambda_0 \times 0.04\ \lambda_0$	Complex	2.45	Center lobe: 80 Side lobe: 80	8.7	42.4% (input power=-10 dBm) 55.3% (input power=-4 dBm)
[5]	$2.8\lambda_0 \times 1.88\lambda_0 \times 0.03\ \lambda_0$	Simple	2.45	Each beam (2): 70	14.6	16.3% – 45.3% (Power density=1 $\mu W/cm^2$)
[6]	$1.25\lambda_0 \times 0.67\lambda_0 \times 0.03\ \lambda_0$	Simple	2.45	90	8.5	19.5% – 44.6% (Power density: 0.05-1 $\mu W/cm^2$)
This work	$\lambda_0 \times \lambda_0 \times 0.03\ \lambda_0$	Simple	2.45	117	7.8	47.4% (Power density=1 $\mu W/cm^2$, input power: -35-0 dBm)

5.4 Summary

In this chapter verified the possibility to achieve a high gain and wider beamwidth MTS antenna for energy harvesting system. Different MTS modes having high gain radiation patterns can be excited individually with their outputs combined. For example, when the electromagnetic waves are from the left side, the MTS mode with a main lobe on the right can receive these electromagnetic waves with a high gain. If the electromagnetic waves are vertical to the MTS layer, the fundamental mode with a directional main lobe orthogonal to the MTS layer can harvest energy with a high gain. Therefore, it can effectively receive electromagnetic waves from a wide angle. At the same time, the receiver part is low-profile and with simple structures permitting easy implementation. This rectenna design is particularly suitable for scenarios where the source location is unknown or multiple sources exist from different directions.

5.5 References

[1] C. Song, Y. Huang, J. Zhou, J. Zhang, S. Yuan, and P. Carter, "A High-Efficiency Broadband Rectenna for Ambient Wireless Energy Harvesting," *IEEE Transactions on Antennas and Propagation*, vol. 63, no. 8, pp. 3486-3495, Aug. 2015.

[2] L. Li, X. Zhang, C. Song, W. Zhang, T. Jia, and Y. Huang, "Compact Dual-Band, Wide-Angle, Polarization Angle-Independent Rectifying Metasurface for Ambient Energy Harvesting and Wireless Power Transfer," *IEEE Transactions on Microwave Theory and Techniques*, vol. 69, no. 3, pp. 1518-1528, Mar. 2021.

[3] A. Jie, M. Nasimuddin, M. F. Karim, and K. T. Chandrasekaran, "A Wide-Angle Circularly Polarized Tapered-Slit Patch Antenna With a Compact Rectifier for Energy-Harvesting Systems," *IEEE Antennas and Propagation Magazine*, vol. 61, no. 2, pp. 94-111, Apr. 2019.

[4] S. Shen, Y. Zhang, C. Y. Chiu, and R. Murch, "A Triple-Band High-Gain Multibeam Ambient RF Energy Harvesting System Utilizing Hybrid Combining," *IEEE Transactions on Antennas and Propagation*, vol. 67, no. 11, pp. 9215-9226, Nov. 2020.

[5] Y. Y. Hu, S. Sun, H. Xu, and H. Sun, "Grid-Array Rectenna With Wide Angle Coverage for Effectively Harvesting RF Energy of Low Power Density," *IEEE*

Transactions on Microwave Theory and Techniques, vol. 67, no. 1, pp. 402-413, Jan. 2019.

[6] Y. Y. Hu, S. Sun, H. J. Su, S. Yang, and J. Hu, "Dual-Beam Rectenna Based on A Short Series-Coupled Patch Array," *IEEE Transactions on Antennas and Propagation*, 2021. (Early Access)

[7] W. Liu, Z. N. Chen, and X. Qing, "Metamaterial-Based Low-Profile Broadband Mushroom Antenna," *IEEE Transactions on Antennas and Propagation*, vol. 62, no. 3, pp. 1165-1172, Mar. 2014.

[8] F. Lin and Z. N. Chen, "Low-Profile Wideband Metasurface Antennas Using Characteristic Mode Analysis," *IEEE Transactions on Antennas and Propagation*, vol. 65, no. 4, pp. 1706-1713, Apr. 2017.

[9] W. Liu, Z. N. Chen, and X. Qing, "Metamaterial-Based Low-Profile Broadband Aperture Coupled Grid-Slotted Patch Antenna," *IEEE Transactions on Antennas and Propagation*, vol. 63, no. 7, pp. 3325-3329, Jul. 2015.

[10] W. Yang, L. Gu, W. Che, Q. Meng, Q. Xue, and C. Wan, "A Novel Steerable Dual-Beam Metasurface Antenna Based on Controllable Feeding Mechanism," *IEEE Transactions on Antennas and Propagation*, vol. 67, no. 2, pp. 784-793, Feb. 2019.

[11] X. Yang, Y. Liu, and S. X. Gong, "Design of a Wideband Omnidirectional Antenna With Characteristic Mode Analysis," *IEEE Antennas and Wireless Propagation Letters*, vol. 17, no. 6, pp. 993-997, Jun. 2018.

[12] T. Li and Z. N. Chen, "Wideband Substrate-Integrated Waveguide-Fed Endfire Metasurface Antenna Array," *IEEE Transactions on Antennas and Propagation*, vol. 66, no. 12, pp. 7032-7040, Dec. 2018.

[13] T. Li and Z. N. Chen, "Shared-Surface Dual-Band Antenna for 5G Applications," *IEEE Transactions on Antennas and Propagation*, vol. 68, no. 2, pp. 1128-1133, Feb. 2020.

[14] C. Song, Y. Huang, P. Carter, J. Zhou, S. D. Joseph, and G. Li, "Novel Compact and Broadband Frequency Selectable Rectennas for a Wide Input-Power and Load

Impedance Range," *IEEE Transactions on Antennas and Propagation*, vol. 66, no. 7, pp. 3306-3316, Jul. 2018.

[15] W. Zhang, C. Song, R. Pei, Y. Huang, and J. Zhou, "Broadband Metasurface Antenna Using Hexagonal Loop-Shaped Unit Cells," *IEEE Access*, vol. 8, pp. 223797-223803, Dec. 2020.

[16] Surface Mount Mixer and Detector Schottky Diodes, Data Sheet. Skyworks Solutions, Inc., Woburn, MA, USA, 2013.

[17] D. J. Lee, S. J. Lee, I. J. Hwang, W. S. Lee, and J. W. Yu, "Hybrid power combining rectenna array for wide incident angle coverage in RF energy transfer," *IEEE Transactions on Microwave Theory and Techniques*, vol. 65, no. 9, pp. 3409–3418, Sep. 2017.

[18] S. Ladan, A. B. Guntupalli, and K. Wu, "A high-efficiency 24 GHz rectenna development towards millimeter-wave energy harvesting and wireless power transmission," *IEEE Transactions on Circuits and Systems I: Regular Papers*, vol. 61, no. 12, pp. 3358–3366, Dec. 2014.

[19] D. Anandkumar and R. G. Sangeetha, "Design and analysis of aperture coupled microstrip patch antenna for radar applications," *International Journal of Intelligent Networks*, vol. 1, pp. 141-147, Nov. 2020.

Chapter 6 Key Contributions and Future Work

6.1 Key Contributions

In this thesis, a comprehensive study of exciting multiple modes in MTS antennas to improve antenna performance is presented, such as broad/dual bandwidth or wide beamwidth. This thesis also demonstrates that the properties of MTS antennas render them suitable for both wireless communications and energy harvesting systems.

6.1.1 Mode Analysis of the basic MTS antenna

In Chapter 3, the mode analysis from the structure of a basic MTS antenna is proposed, which facilitates further understanding of the working mechanism behind an MTS antenna. Such analysis illustrates that the radiation property can be attributed to the current distributions of the MTS mode, while the electric-/magnetic-field distributions are used to identify the MTS mode, which is referenced from the mode identification method of the waveguide. Additionally, several parametric studies are discussed to provide further understanding of the relationship between the modes and the antenna structure, such as the size of the unit cells, the gap between neighboring unit cells, the number of the unit cells, and the geometry of the unit cells.

6.1.2 MTS Antenna with Bandwidth Improvement in Wireless Communication System

In Chapter 4, attractive designs of an MTS antenna with bandwidth improvement in wireless communication systems are introduced. A discussion is provided on the relationship between the geometry of the unit cell and the bandwidth, which could be a direct way to increase the bandwidth. Compared with conventional square-shaped unit cells, a broader bandwidth can be achieved by utilizing hexagonal-shaped unit cells. Two reasons for such findings are illustrated in detail in Chapter 4. Another proposed dual broadband nonuniform MTS antenna is also analyzed, in which a composite right-/left-handed structure is used to excite the left-handed property at the lower band and the right-handed property (normal MTS modes) at the higher band. The main novelty of the design is that the appropriate positions of the shorting pins can

be selected to maintain the broad bandwidth performance at the higher band. The positions should be chosen at the nulls of E-field distributions at each excited mode at the higher band.

6.1.3 MTS Antenna with Beamwidth Improvement in Energy Harvesting System

In Chapter 5, a discussion is provided on developing an MTS antenna with beamwidth improvement and high gain simultaneously to collect more power in the energy harvesting system. In the developed MTS antenna, three modes with different radiation patterns are excited through the middle and two side aperture-coupled feedings, respectively. By exciting the three modes simultaneously, then linking each excited mode with a rectifier circuit, and finally combining the three rectifiers at direct current (DC) with a single load, a wide beamwidth can be obtained to harvest incident waves from different directions. The key novelty of using such multiport MTS antenna as a receiver is that the unit cells on the MTS layer could be reused to effectively excite different MTS modes with different radiation patterns, thereby achieving a collector with beamwidth improvement.

6.2 Future Work

Based upon the aforementioned summaries and considering the challenges of existing technologies, further research can be conducted in the following areas:

6.2.1 Optimization of broadband MTS antenna

1. Broadband MTS antennas can be realized by exciting different MTS modes resonating at different frequencies and then combining said modes. The difficulty lies in determining how to excite desired modes and suppressing the undesired modes simultaneously.

2. To obtain a broadband MTS antenna, different MTS modes with similar directional radiation patterns resonating at different frequencies should be excited simultaneously. However, as the frequency increases, the directional radiation pattern of excited MTS modes will have larger/more side lobes, which is not preferred. As a result, investigating the bandwidth limitation of a broadband MTS antenna while maintaining the integrity of the directional radiation pattern is meaningful.

6.2.2 Optimization of MTS antenna for energy harvesting

1. The design of MTS antennas in energy harvesting systems can be further improved. Several properties of MTS antennas have not been fully explored. The antenna performance can be improved in terms of several aspects, such as (a) designing a dual-polarization MTS antenna; and (b) designing a broad bandwidth MTS antenna by changing the structure of radiating elements or the layout of the MTS layer. Additionally, the rectifier design can be improved to be more suitable for broader bandwidths and different input power levels.

2. The MTS antenna design in Chapter 5 is a simple example that can be used to demonstrate how the advantages of MTS antennas can be used to design a receiver in energy harvesting. Although more ports can be used to cover wider incident angles in reality, there will be an optimal value for the number of the ports versus the maximum radio frequency (RF)-to-DC conversion efficiency (or output DC power). As such, exploring and evaluating the port number will be a meaningful investigation.

3. Owing to the uncertainty and randomness of ambient environments, adaptive and reconfigurable MTS antennas might be worth exploring. The MTS antenna can be optimized using a hybrid technique that combines RF and DC. The pattern and beam direction can be adaptive and self-reconfigurable in real-time to deal with varying ambient EM field conditions.

6.2.3 New materials

New materials with unique properties have recently been applied as conductive or substrate materials in several antenna designs. To illustrate, the bandwidth can be extended by liquid materials with a high dielectric constant. The utilization of new materials in MTS antennas can improve the antenna performance.

6.3 Reference

[1] Y. F. Cheng, X. Ding, X. Xu, X. Zhong, and C. Liao, “Design and Analysis of a Bow-Tie Slot-Coupled Wideband Metasurface Antenna,” *IEEE Antennas and Wireless Propagation Letters*, vol. 18, no. 7, pp. 1932-1936, Jul. 2019.

[2] X. Yang, Y. Liu, and S. X. Gong, “Design of a Wideband Omnidirectional Antenna With Characteristic Mode Analysis,” *IEEE Antennas and Wireless Propagation Letters*, vol. 17, no. 6, pp. 993-997, Jun. 2018.

[3] C. Shi, J. Cui, R. Zhang, and Y. Han, “Diamond-shaped metasurface low-profile wideband antenna,” *IET The Journal of Engineering*, vol. 2019, no. 20, pp. 6566-6567, Oct. 2019.

[4] Z. Yang, F. Liang, Y. Yi, D. Zhao, and B. Wang, "Metasurface-based wideband, low-profile, and high-gain antenna," *IET Microwaves, Antennas and Propagation*, vol. 13, no. 4, pp. 436-441, Mar. 2019.

[5] H. Bai, G. Wang, and T. Wu, "High-Gain Wideband Metasurface Antenna With Low Profile," *IEEE Access*, vol. 7, pp. 177266-177273, Dec. 2019.

[6] M. S. Alharbi, C. A. Balanis and C. R. Birtcher, "Performance Enhancement of Square-Ring Antennas Exploiting Surface-Wave Metasurfaces," *IEEE Antennas and Wireless Propagation Letters*, vol. 18, no. 10, pp. 1991-1995, Oct. 2019.

[7] T. Li and Z. N. Chen, “A dual-band metasurface antenna using characteristic mode analysis,” *IEEE Transactions on Antennas and Propagation*, vol. 66, no. 10, pp. 5620-5624, 2018.

[8] K. Li, L. Li, Y. M. Cai, C. Zhu, and C. H. Liang, “A Novel Design of Low-Profile Dual-Band Circularly Polarized Antenna With Meta-Surface,” *IEEE Antennas and Wireless Propagation Letters*, vol. 14, pp. 1650-1653, 2015.

END